Intravascular Ultrasound and Photoacoustic Image Reconstruction

For improved lipid imaging in atherosclerotic coronary arteries

MSc Thesis

Amerens Bekkers

Delft University of Technology

TU Delft

Intravascular Ultrasound and Photoacoustic Image Reconstruction

For improved lipid imaging in atherosclerotic coronary arteries

by

Amerens Bekkers

Student Name	Student Number
Amerens Bekkers	4477375

Supervisor Technical University of Delft: Dr. ir. H. J. Vos
Supervisor Kaminari Medical: Dr. V. Daeichin
Supervisor Erasmus Medical Center: Prof. dr. G. van Soest
Project Duration: February, 2022 - November, 2022
Faculty: Faculty of Mechanical, Maritime and Materials Engineering, Delft

Cover: *Isabel van Ommen*

TU Delft

Preface

Writing this preface does not only mark the end of my thesis project, but also of my time at university. A new phase in my life is about to start, for which I am very excited. I look back on my time at the TU Delft with satisfaction, and I am proud of my achievements.

Needless to say, there are many people I want to thank that have contributed to the way I feel looking back on this period. First of all, my parents. I feel so lucky to have such encouraging parents that support me in any choice I make and any adventure I want to embark on. Their emotional and financial support has made it possible for me to make the most out of my time as a student, for which I am very grateful.

During my thesis, there were several people with whom I have had fruitful discussions or who gave their valuable insights. First and foremost, I would like to thank my thesis supervisors, Verya Daeichin, Rik Vos, and Gijs van Soest for their feedback and critical questions that definitely pushed me a bit further each time to improve my research. In particular, I would like to thank my daily supervisor Verya Daeichin for our countless talks. He is one of the most humble and intelligent people I have ever met, who barely needed an explanation before he could already give highly relevant input. A special thanks goes to all people at Kaminari Medical for including me on their journey of developing a new medical technology. Especially to Jeroen Kodde, who gave me the warmest welcome and made me feel part of the team from day one. Next, I would like to thank Hans Bosch, Sowmiya Chandramoorthi, and Antonio López Marín for our conversations and the ideas they provided for my research.

Lastly, I want to thank my friends, without whom my student's life would not have been as joyful. Besides all the fun, they are the reason I immediately felt at ease in Delft. It would be impossible to give everyone the credit they all truly deserve, but I do want to highlight a few. I want to thank Isabel, Cas, and Martin for the study sessions or talks whenever I needed a different surrounding or some moral support during this my thesis. I want to thank Liza for putting things in perspective and encouraging me to be proud of myself. Yasmin, thank you for the much-needed push to take a break when times were too demanding. Toke, Ella, and Rebekka many thanks for your valuable feedback on my thesis, and most of all, thank you for being a truly great (second) home.

I am looking forward to using all the skills, tools, and knowledge that the TU Delft provided me to pursue a professional career dedicated to contributing to a better world.

Amerens Bekkers
Delft, December 2022

Summary

Introduction: Coronary atherosclerosis can form large lipid-rich plaques inside the arteries, which are prone to rupture. Rupture can lead to thrombus formation and subsequent obstruction of the blood flow, which is the most common cause of acute coronary events like myocardial infarction. Current imaging modalities lack the ability to image important factors in the diagnosis of these vulnerable plaques or have a limited image quality. A novel imaging modality, intravascular ultrasound (IVUS) combined with intravascular photoacoustics (IVPA), is a good candidate for accurate lipid imaging in atherosclerotic coronary arteries. IVPA enables specific lipid imaging alongside the artery morphology image provided by IVUS. Kaminari Medical is developing the first rotating IVUS and IVPA catheter for this purpose.
Objective: The objective of this research project is to develop an image reconstruction method with improved lateral resolution (LR) and Signal-to-Noise Ratio (SNR) compared to the conventional image reconstruction method.
Methods and Materials: A literature review was executed to find the state-of-the-art image reconstruction method for IVUS and IVPA. A virtual source synthetic aperture (VSSA) beamforming method with Coherence Factor Weighting (CFW) was selected and implemented to achieve the desired image quality improvement. The principle of the VSSA is that the signals captured at adjacent transducer positions are delayed and summed to use all available image information. The delays are calculated with respect to the virtual sources, which are placed at the natural focus of the beams under the assumption that this yields the best alignment after delaying the signals. A pixel-based implementation of VSSA with CFW was developed on IVUS data which directly reconstructs the image pixel values. Subsequently, the algorithm is optimized to achieve the best image quality for IVUS and IVPA data acquired by the Kaminari Medical catheter.
Results: The implementation of the algorithm based on the literature did not show the image quality as expected, most likely due to the invalid assumption that the virtual source should lie at the natural focus of the ultrasound beam. Therefore, the virtual source depth and the opening angle of the beam are optimized to find the parameter combination that achieves the best image quality. For both IVUS and IVPA, narrow beam shapes and a virtual source behind the transducer, thus using diverging beam shapes, should be used to obtain the best LR and SNR. The optimized VSSA leads to an increased SNR by 20.3% and 77.7% for IVUS and IVPA, respectively. The LR is increased by 7% for IVPA but shows a LR reduction for the IVUS data.
Conclusion: The optimized VSSA meets the objective of improving the LR and SNR to a large extent. However, it is recommended to focus future work on developing a substitutional weighting method for the CFW to also improve the LR for the IVUS data.

Contents

Preface i

Summary ii

Nomenclature v

1 Introduction 1
1.1 General Introduction . . . 1
1.2 Research Design . . . 2
1.2.1 Problem Statement and Research Objective . . . 2
1.2.2 Research Approach . . . 3
1.3 Relevance . . . 4
1.3.1 Scientific Relevance . . . 4
1.3.2 Clinical Relevance . . . 4

2 Background 5
2.1 Coronary Atherosclerosis . . . 5
2.2 Imaging Physics . . . 6
2.2.1 Intravascular Ultrasound . . . 6
2.2.2 Intravascular Photoacoustics . . . 7
2.3 Kaminari Medical Imaging Catheter . . . 8
2.4 IVUS and IVPA Image Reconstruction . . . 9

3 Virtual Source Synthetic Aperture Beamforming with Coherence Factor Weighting 10
3.1 Introduction . . . 10
3.1.1 VSSA and CFW Theory . . . 10
3.2 Materials and Methods . . . 12
3.2.1 Implementation . . . 12
3.2.2 Data . . . 15
3.2.3 Image Reconstruction and Quality . . . 16
3.3 Results . . . 16
3.3.1 Algorithm Outputs . . . 16
3.3.2 Image Reconstruction . . . 18
3.4 Discussion . . . 20
3.4.1 Performance . . . 20
3.4.2 Implementation . . . 21

4 Optimization 22
4.1 Introduction . . . 22
4.2 Materials and Methods . . . 22
4.2.1 Theoretical Validation VSSA . . . 22
4.2.2 Optimization . . . 24
4.2.3 Image Reconstruction and Quality . . . 25
4.3 Results . . . 25
4.3.1 Theoretical Validation VSSA for IVUS . . . 25
4.3.2 IVUS Optimization . . . 27
4.3.3 IVPA . . . 29
4.3.4 Image Reconstruction and Quality . . . 29
4.4 Discussion . . . 32
4.4.1 Theoretical Validation VSSA . . . 32
4.4.2 Optimization . . . 32
4.4.3 Image Reconstruction and Quality . . . 33

5 General Discussion **34**
5.1 Conclusion . . . 34
5.2 Weighting Method . . . 36
5.3 Algorithm Implementation . . . 37
5.3.1 Beam Shape Overlap . . . 37
5.3.2 Pixel-based Discretization . . . 38
5.3.3 Implementation for IVPA . . . 39

A Appendix A - Literature Review **45**

B Appendix B - IVPA Optimization Results **57**
B.1 Theoretical Validation . . . 57
B.1.1 Delay and Sum Effect . . . 57
B.1.2 Theoretical Maximum Image Quality . . . 58
B.2 Optimization . . . 59

Nomenclature

Abbreviations

Abbreviation	Definition
CAD	Coronary Artery Disease
CFW	Coherence Factor Weighting
CNR	Contrast-to-Noise Ratio
DAS	Delay and Sum
LCA	Left Coronary Artery
LR	Lateral Resolution
IVPA	Intravascular Photoacoustics
IVUS	Intravascular Ultrasound
IV-OCT	Intravascular Optical Coherence Tomography
MUST	Matlab Ultrasound ToolBox
MI	Maximum Intensity
NIRS	Near-Infrared Spectroscopy
PCI	Percutaneous Coronary Intervention
PA	Photoacoustics
PAI	Photoacoustic Imaging
PSF	Point Spread Function
RCA	Right Coronary Artery
RF	Radiofrequency
SAF	Synthetic Aperture Focusing
SAFT	Synthetic Aperture Focusing Technique
SCF	Sign Coherence Factor
SNR	Signal-to-Noise Ratio
TCFA	Thin-cap Fibroatheroma
TGC	Time Gain Compensation
US	Ultrasound
VS	Virtual Source
VSSA	Virtual Source Synthetic Aperture
2D	Two-dimensional
3D	Three-dimensional

Symbols

Symbol	Definition	Unit
c	Speed of sound	$[m \cdot s^{-}1]$
C_p	Specific Heat Capacity	$[J \cdot kg^{-1} \cdot K^{-1}]$
d	Distance	$[m]$
D	Width of the transducer	$[m]$
f_c	Center frequency	$[Hz]$
F	Laser fluence	$[J \cdot m^{-2}]$
L_{NF}	Beam width at near field	$[m]$
L_{FF}	Beam width at far field	$[m]$
i	RF index	-
N	Number of RF lines overlapping a pixel	-

Symbol	Definition	Unit
p_o	Source pressure	$[J \cdot m^{-3}]$
r	Depth distance between pixel and virtual source	$[m]$
r'	Direct distance between pixel and virtual source	$[m]$
t	Time	$[s]$
Δt	Time delay	$[s]$
w	beam shape width	$[m]$
w_{td}	beam shape width at transducer surface	$[m]$
w_B	beam shape width at imaging depth	$[m]$
Z	Acoustic Impedance	$[kg \cdot m^{-2} \cdot s^{-1}]$
z	Imaging depth	$[m]$
z_p	Pixel depth	$[m]$
z_f	Natural focus depth	$[m]$
z_{vs}	Optimized virtual source depth	$[m]$
α	Half opening Angle	$[deg]$
α_{rad}	Full opening angle	$[rad]$
β	Isobaric volume expansion coefficient	$[K^{-1}]$
Γ	Grüneisen coefficient	-
λ	wavelength	$[m]$
μ	Absorption coefficient	$[m^{-1}]$
ρ	Tissue density	$[kg \cdot m^{-3}]$

1 Introduction

1.1. General Introduction

Coronary Artery Disease (CAD) is the leading cause of death worldwide [1]. CAD is primarily caused by atherosclerosis [2], which leads to lipid accumulation and calcification in the coronary arteries [2, 3]. This atherosclerotic mechanism can form large lipid-rich plaques with a necrotic core that is contained by a thin fibrous cap [4, 5]. This type of plaque is also referred to as thin-cap fibroatheroma (TCFA) or vulnerable plaque. Rupture of a vulnerable plaque can lead to thrombus formation, and subsequent obstruction of the blood flow, which is the most common cause of acute coronary events like myocardial infarction [3, 6, 7]. Many patients suffering from obstructive CAD or acute coronary syndrome (ACS) are treated by a percutaneous coronary intervention (PCI) [8, 9]. Still, 12% of the patients that underwent PCI need another intervention within the first year due to acute cardiac events [8, 9]. Half of these events are caused by non-culprit plaques [8], which are not the plaques responsible for the initial PCI. This indicates the importance of more accurate detection of all lipid-rich plaques at risk.

Currently, several imaging modalities are used in the clinical practice for intravascular imaging of the coronary arteries. Intravascular Ultrasound (IVUS) is a widely used modality that performs well in imaging the arterial wall structures and detecting calcification, and stenosis [10]. However, since IVUS lacks adequate soft-tissue contrast, it can neither be used for measurement of the fibrous cap thickness nor the detection of the lipid-core, which are two key features of vulnerable plaques [11, 12]. Other imaging modalities aim to enable quantification of the fibrous cap thickness and the lipid-core size to provide more accurate intravascular lipid imaging. One of these modalities is Intravascular Optical Coherence Tomography (IV-OCT) which detects the optical reflection of the emitted near-infrared light to visualize the arterial wall [13]. Therefore, it is analogous to IVUS because IVUS detects the echo of the transmitted ultrasound wave [13]. IV-OCT provides a high spatial resolution which enables identifying the fibrous cap thickness [4, 14, 15], but does have a limited penetration depth of 1-2 mm [4]. Another modality is Near-Infrared Spectroscopy (NIRS), which can detect lipids by identifying the chemical components of the tissue [16]. The reflection spectrum of the near-infrared light is compared to the reflection spectrum of a vulnerable plaque to find the location and intensity of lipid content [17]. Moreover, the NIRS signal, and thus the lipid distribution, is not depth-resolved [4, 15, 18, 19]. As a result, NIRS does not provide a fibrous cap thickness measurement [19]. Thus, all imaging modalities currently used in the clinic have some limitations that preclude optimal vulnerable plaque imaging in coronary atherosclerosis.

IVUS combined with intravascular photoacoustics (IVPA) is a novel imaging modality that is a promising candidate to overcome these limitations. IVPA is based on the optical absorption of pulsed light. This causes transient thermoelastic expansion and local tissue heating, which generates a pressure sound wave. Detecting this sound wave allows for accurate reconstruction of the absorption site [18, 20]. When using specific wavelengths, IVPA can image lipid content, which is fundamental in diagnosing vulnerable plaques [21] and provides clinically relevant information that could improve diagnosis and enhance intervention strategy [12, 22]. Due to the combination with IVUS, the lipids can be imaged alongside the arterial wall morphology. IVPA has been applied to human plaque specimens and large-

animal coronary atherosclerosis models but is not clinically available. Kaminari Medical is a company that aims to bring the first IVUS and IVPA catheter to the clinic to prevent re-interventions with improved lipid detection. Kaminari Medical is developing a rotating catheter that uses laser light pulses to excite the PA effect. The IVUS and IVPA signals are received from each rotation position. Subsequently, images can be composed of these signals to visualize cross-sections of the artery. Developing the optimal image reconstruction method is one of the essential steps in developing and validating this new technology, and is therefore the main topic of this research.

1.2. Research Design

1.2.1. Problem Statement and Research Objective

Multiple studies show that stent implantation guidance by intravascular imaging like IVUS reduces the rate of cardiac events in the long term for up to 5 years [23, 24]. Enabling accurate lipid imaging by IVPA has the potential to further reduce the risk of recurring cardiac events due to improved lipid imaging. Nevertheless, wider implementation of intravascular imaging of the coronary arteries is held back due to image interpretation issues [25]. Thus, high-quality IVUS and IVPA images are needed. The problem statement is summarized as follows:

Problem Statement

IVUS combined with IVPA is a promising imaging modality that can potentially reduce the risk of recurring cardiac events through more accurate lipid imaging. This requires high-quality images of the coronary arteries. However, the optimal image reconstruction method to obtain high-quality IVUS and IVPA images has yet to be invented.

Hardware design choices can limit the intrinsic image quality of IVUS and IVPA images, or the image quality is insufficient for the specific goal of atherosclerotic lipid imaging. Therefore, there is a need to research and develop an image reconstruction method that yields IVUS and IVPA images that meet certain image quality criteria for lipid imaging in atherosclerotic coronary arteries. The research objective that follows from the problem statement is defined as follows:

Main Research Objective

To develop an IVUS and IVPA image reconstruction method with improved image quality to advance lipid imaging in atherosclerotic coronary arteries.

Generally, the desired image quality improvement is an improvement of the currently obtained image quality by the conventional image reconstruction method of stacking the received echo signals, i.e., the US radio frequency (RF) data. The image is reconstructed by stacking the RF lines of adjacent transducer positions next to each other to fill the image pixels. A more detailed explanation can be found in Section 2.4. This is further referred to as the original reconstruction. A literature review is conducted to specify what image quality metrics are important for intravascular imaging and to find the best image reconstruction method to achieve the desired image quality. The literature review aims to answer the first research question:

Research Question 1

What is the state-of-the-art image reconstruction for IVUS and IVPA?

Since IVPA image reconstruction has not been researched extensively due to its novelty, IVUS or other photoacoustic (PA) image reconstruction methods are sought that could be applied to IVPA. The full version of the literature review can be found in Appendix A, but the most important findings of the literature review that are used to guide this research are outlined below:

From the synthesis of ten studies describing IVUS image reconstruction can be concluded that spatial resolution (lateral and axial) and contrast are the most important image quality metrics for IVUS images. The lateral resolution (LR) improvement is most important when using IVUS for atheroscle-

rotic plaque imaging because this strongly deteriorates when there is a high amount of plaque present [26]. The LR is defined as the ability to distinguish imaging objects that are located side-by-side at the same depth [27]. Besides, a high signal-to-noise ratio (SNR) is required for measuring atherosclerotic plaque burden [28]. Most studies achieve this by a Synthetic Aperture Focusing Technique (SAFT), which is also seen in the literature review of PA image reconstruction methods. This consists mainly of SAFT to improve the LR and SNR beyond the natural focus of the beam. In conclusion, the desired image quality improvement can be defined as an improvement of the lateral resolution and SNR of the reconstructed images compared to the original images. To this purpose, the Virtual Source Synthetic Aperture (VSSA) focusing with Coherence Factor Weighting (CFW) by Yu et al. [29] was selected to implement due to its potential applicability to both IVUS and IVPA and the high image quality improvements.

The next phase of this research involves developing and implementing the state-of-the-art image reconstruction method. The algorithm will be developed on IVUS data. The effect of this algorithm on the image quality will be evaluated, leading to the following research question:

Research Question 2

What is the image quality improvement achieved by implementing the state-of-the-art image reconstruction method compared to the original reconstruction?

Once implemented in the form found in the literature, the next objective is to find whether further improvements in LR and SNR can be achieved for the Kaminari Medical IVUS and IVPA catheter. The algorithm will be optimized for IVUS and IVPA data. This leads to research question 3:

Research Question 3

What are the optimal algorithm parameters to reconstruct high-quality images from data acquired with the Kaminari Medical IVUS and IVPA catheter?

Subsequently, the performance of the optimized versions of the algorithm is evaluated as described in research question 4:

Research Question 4

What is the image quality improvement after optimization compared to the original reconstruction?

Lastly, it will be assessed whether the main research objective is met by comparing the algorithm performance regarding LR and SNR to the original reconstruction. Besides, the algorithm implementation and techniques used throughout the research will be evaluated.

1.2.2. Research Approach

This research project is divided into four phases: Exploration, Implementation, Optimization, and Conclusion. The exploration phase is meant to familiarize oneself with the topic, gain the necessary background and perform the literature review. The implementation phase is where the state-of-the-art image reconstruction method found in the literature will be implemented as an algorithm. This implementation will be executed in MATLAB 2022a and developed and tested on IVUS data. The implementation phase is followed by an optimization phase where the algorithm will be optimized to obtain the most significant IVUS and IVPA image quality improvements for the Kaminari Medical catheter characteristics. Lastly, it will be validated whether the main research objective is reached by comparing the images reconstructed by the algorithm with the original image reconstruction results. Figure 1.1 gives an overview of the research design.

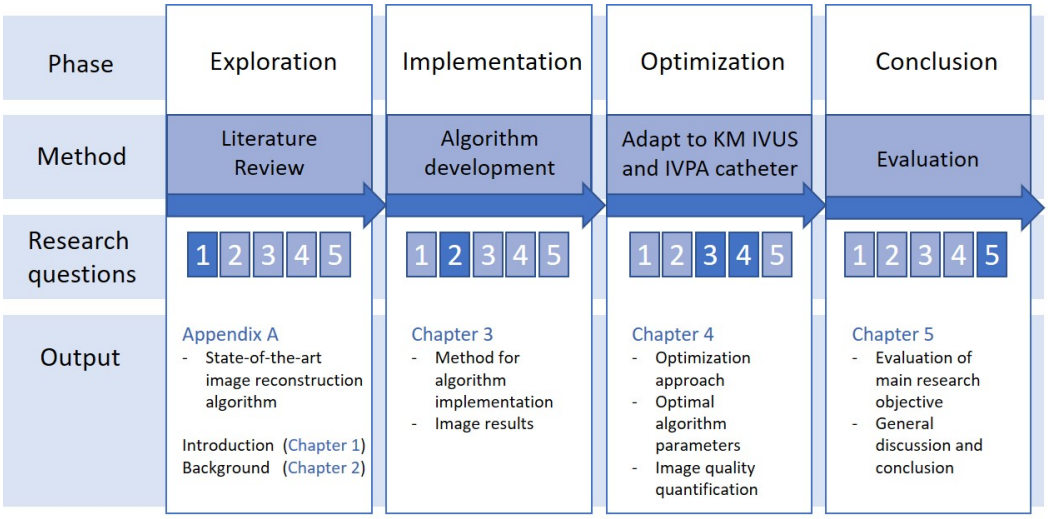

Figure 1.1: Overview of the research approach with the methods, research questions, and expected output per phase.

1.3. Relevance

1.3.1. Scientific Relevance

Many steps must be taken to validate the functionality, safety, and relevance to enable the translation of IVPA into medical practice. One of these steps is to develop an image reconstruction method to provide the highest possible image quality. This research provides the first advanced image reconstruction for an IVUS and IVPA combined imaging modality. This could form a substantial basis for further image quantification of the thin fibrous cap and other image markers in vulnerable plaques.

1.3.2. Clinical Relevance

The clinical relevance of this research lies in the role that the Kaminari Medical catheter will play in preventing PCIs through improved diagnosis and treatment strategy. An overview of the impact of imaging with the Kaminari Medical catheter is given in Figure 1.2. First, the number of PCIs performed worldwide in 2022 is close to 6 million (source: Kaminari Medical, based on GlobalData). 12% of these patients that underwent PCI still need a re-intervention, which accounts for 720 thousand re-catheterizations. Half of the cardiac events leading to a re-intervention are caused by non-culprit plaques [8], which could potentially have been identified with Kaminari Medical's imaging catheter, resulting in the prevention of around 360 thousand re-catheterizations. This does not even consider the patients who did not survive a cardiac event after their PCI, whose lives could have been saved by improved imaging by Kaminari Medical. Prevention of those 360 thousand re-catheterizations leads to an estimated yearly cost saving of €2.8 based on a catheter price of €8000,- (source: Kaminari Medical).

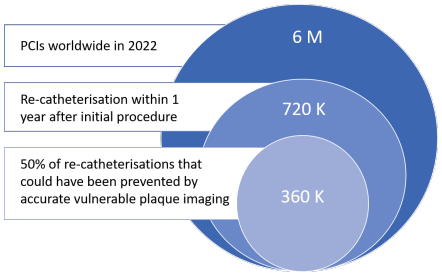

Figure 1.2: Overview of the impact of imaging with the Kaminari Medical IVUS and IVPA catheter based on 6 million PCIs procedures worldwide. 720 thousand of these 6 million PCIs need a re-catheterization within one year due to major adverse cardiac events. This leads to 360 thousand re-catheterizations that could have been prevented by more accurate plaque imaging because 50% of the cardiac events were caused by non-culprit, or non-diagnosed, plaques.

2

Background

2.1. Coronary Atherosclerosis

The coronary arteries are located on the outside of the myocardium because they are responsible for the blood supply to the heart [30]. Therefore, unrestricted blood flow through the coronary arteries is of major importance. One of the diseases that could complicate this is atherosclerosis. Coronary atherosclerosis is a progressive disease with a complex inflammatory mechanism that causes the accumulation of lipids in the arteries. Dysfunctional endothelial cells initiate the inflammatory cascade that leads to the development of atherosclerosis [3]. The induced inflammatory cascade can lead to advanced plaques with accumulated extracellular lipids [31]. There are multiple types of plaques, but the plaques with the highest rupture risk are the so-called thin-cap fibroatheroma or vulnerable plaques as previously discussed. A visualization of the typical morphology of a vulnerable plaque is depicted in Figure 2.1a. Plaque is generally located in the inner layer of the arterial wall, namely the tunica intima. When the disease progresses, processes like smooth muscle cell proliferation, calcifications, cell death, and plaque rupture take place [3]. Plaque rupture is the most common cause of acute coronary events like myocardial infarction because of the thrombus formation that obstructs the blood flow [6, 7]. Whether a plaque is prone to rupture depends on several factors. These factors are a low concentration of smooth muscle cells (SMC), a large lipid core, a high concentration of macrophages, and a thin fibrous cap (Figure 2.1b) [5, 31].

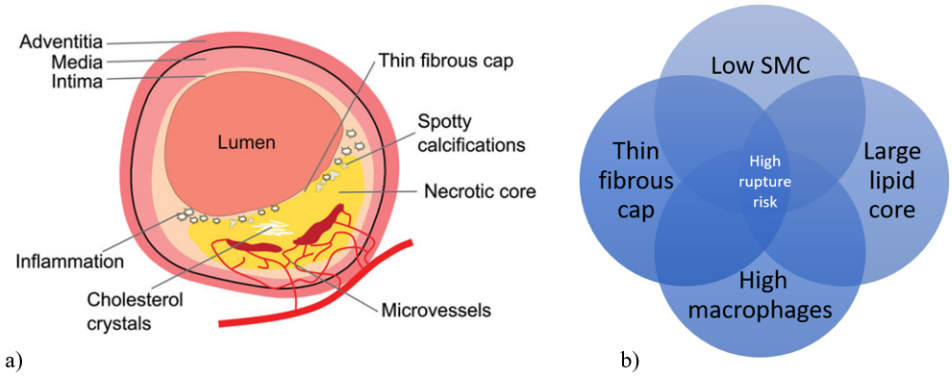

Figure 2.1: a) A schematic overview of a coronary artery with typical morphology traits of a vulnerable plaque. b) The factors associated with a high risk of vulnerable plaque rupture. SMC = smooth muscle cells.

As previously discussed, PCI is a procedure that is often performed to treat coronary atherosclerosis. The goal of a PCI is to reopen occluded arteries by placing a permanent stent. The occlusion site in the coronary artery is entered via the aorta by guiding a catheter from a radial or femoral artery. The catheter tip contains a balloon with a stent around it. The balloon is inflated to open the artery and place

the stent. The balloon is deflated while the stent remains in its position, and the catheter is removed. The procedure is depicted in Figure 2.2. PCI is guided by visualization of the coronary arteries and their stenoses by injecting a contrast agent and acquiring X-ray images. This is called a 2D angiogram. Plaques do not necessarily compromise the arterial lumen because the arterial wall can remodel and increase its external diameter, or the plaque can grow outward instead of inward [31]. This complicates the visibility of plaques on a 2D angiogram. Hence, an intravascular imaging modality is needed to ensure full visibility.

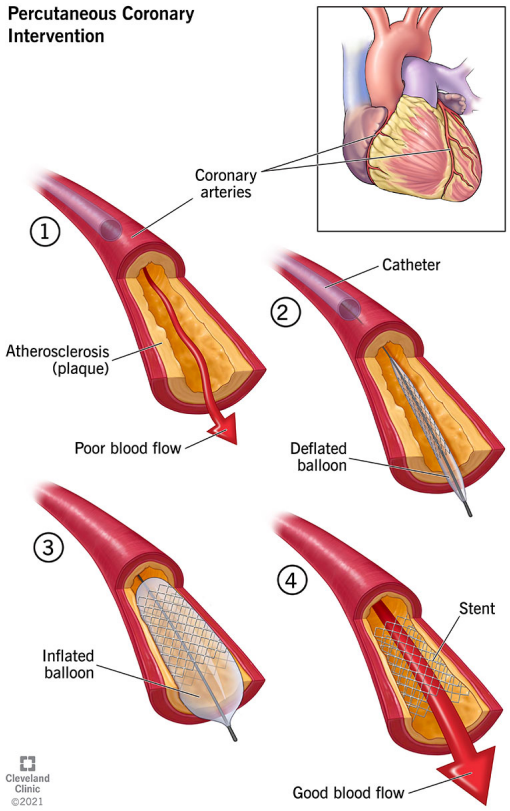

Figure 2.2: Percutaneous coronary intervention. A catheter is guided to the plaque location that occludes the artery. The artery is opened by inflating a balloon and a permanent stent is placed to keep the artery open and reinstate the blood flow. Adapted from [32]

2.2. Imaging Physics

2.2.1. Intravascular Ultrasound

Intravascular Ultrasound (IVUS) is pulse-echo ultrasound imaging, miniaturized to fit a catheter that enables imaging of the vessel wall from inside the blood vessels. IVUS is based on the transmission of a sound wave, and the reception of its echo by a transducer [33]. An echo is a reflection of the sound wave due to a change in acoustic impedance of the tissue. The amount of reflected energy determines the US signal strength, which depends on the difference in acoustic impedance (Z) between the tissues at an interface. When this difference is larger, more energy is reflected as an echo, leading to a stronger image signal. As shown in Equation 2.1, the acoustic impedance (Z) is the product of the tissue density (ρ) and the speed of sound (c) with which the sound wave travels through the tissue [34].

$$Z = \rho \cdot c \tag{2.1}$$

The generation and reception of US waves are based on the piezoelectric effect of the transducer, which is the coupling of mechanical strain and the electrical field in the transducer material [35]. The transmitted sound waves are generated due to mechanical vibrations induced by an electrical current.

Subsequently, the received echo causes a mechanical strain which generates an electrical current [35]. These electrical signals received by the transducer are referred to as the RF data. This RF data is the signal amplitude acquired from multiple echoes over one imaging line, given as a function of time [33]. The RF data can be used to calculate the distance (d) to the tissue location that caused the echo by Equation 2.2 because the sound velocity (c) and the time between pulse transmission and echo reception (t) is known.

$$d = \frac{c \cdot t}{2} \tag{2.2}$$

These principles are used in IVUS such that the layers of the artery can be visualized separately [33], based on the echo reception and corresponding distance calculation.

Ultrasound waves are mechanical vibrations that can propagate in fluids and solids at high frequencies. The sound wave frequency, i.e., the number of oscillations per second, determines the resolution and penetration depth. The higher the frequency, the higher the spatial resolution, but also the lower the penetration depth [36]. Medical US typically has a frequency ranging from 2 to 10 MHz [34]. In IVUS, an imaging depth of up to several millimeters is sufficient, so an even higher frequency can be used.

The ultrasound waves are attenuated as they travel through the tissue due to the gradual energy loss caused by various mechanisms like reflection, deflection of a wave's original direction, or absorption, which causes energy loss by heat dissipation [34]. This results in a weaker echo signal received at the transducer, especially from deeper tissues. Most conventional US systems use a time gain compensation method to compensate for this signal loss by amplifying the RF signal from larger imaging depths [34].

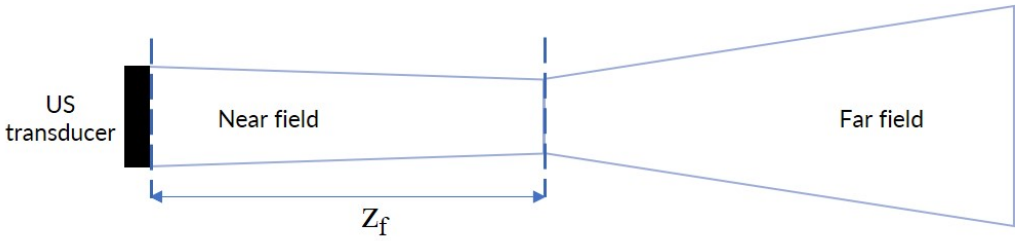

Figure 2.3: US beam shape of a single disk-shaped transducer. The beam consists of a near field and far field. The transition from near to far field is made at the natural focus depth (z_f) of the beam. Adapted from

The ultrasound beam is consists of a near field and a far field, which are separated by the natural focus of the beam. The near field has a more irregular intensity pattern and is rather parallel to the transducer, whereas the far field diverges [36, 37]. An illustration of an US beam shape for a round, disk-shaped transducer is depicted in Figure 2.3. This beam shape is based on the -3 dB contour of the US beam, which is based n a spatial pressure distribution map for the full beam [38]. Taking a -3 dB contour means that energy levels higher than -3 dB contribute to this beam shape. Furthermore, the shape of the beam depends on the frequency and the dimensions and shape of the transducer [37]. The beam in Figure 2.3 illustrates the main lobe of the ultrasound beam, where most of the energy is transmitted. However, a small amount of the energy is directed off-axis adjacent to the main lobe, which are called side lobes [39]. These weak side lobes can also be reflected. The US transducer receives the echoes of the side lobes as if they originate from the main lobe which causes false image signal [39].

2.2.2. Intravascular Photoacoustics

Photoacoustic (PA) imaging (PAI) is based on the optical absorption of pulsed laser light. This causes transient thermoelastic expansion and local heating of the tissue, which generates a pressure sound wave that is received by a transducer [20]. In more detail, the transient pressure increases because the optical energy from the laser pulse is transferred to the tissue. Subsequently, the pressure increase serves as an acoustic source and generates a sound wave [40]. This principle is visually depicted in Figure 2.4.

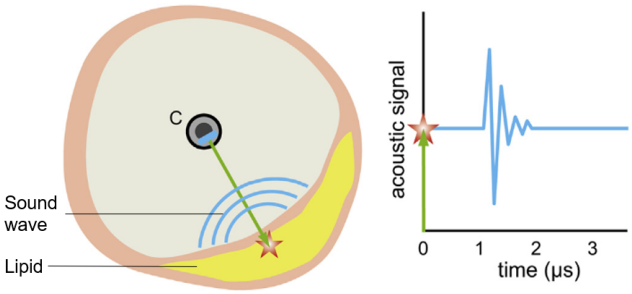

Figure 2.4: The photoacoustic effect. The green line represents the laser pulse that causes transient expansion and local heating. This eventually generates the sound waves that the transducer in catheter C can receive. The laser pulse is very short, only a couple of nanoseconds, so it immediately reaches the tissue. Adapted from [40]

Tissue contents of the arterial wall can be identified in IVPA because tissue types have a specific optical absorption spectrum for light of different wavelengths [20, 40]. Differentiation between tissue components is possible with PA imaging when the excitation wavelengths are selected such that maximum absorption contrast is given between the relevant tissues [40].

Besides the absorption coefficient of the tissue (μ), other factors contribute to the PA signal. The measured PA signal represents the source pressure (p_0), which is generated after the absorption of the laser energy. The source pressure can be calculated using Equation 2.3

$$p_0 = \Gamma \cdot \mu \cdot F \tag{2.3}$$

showing that the source pressure is built up by the local optical absorption coefficient (μ), the laser fluence (F), which represents the light intensity, and the Grüneisen coefficient (Γ) [41]. The Grüneisen coefficient describes the efficiency of the thermo-acoustic conversion and can be calculated using Equation 2.4.

$$\Gamma = \frac{c^2 \cdot \beta}{C_p} \tag{2.4}$$

Grüneisen coefficient (Γ) depends on the speed of sound (c), the isobaric volume expansion coefficient (β), and the specific heat capacity (C_p), which is a measure of the ability to store thermal energy [41].

2.3. Kaminari Medical Imaging Catheter

Kaminari Medical is a company situated in the Erasmus Medical Center (EMC), aiming to bring the first IVUS and IVPA imaging catheter to the clinic. Kaminari Medical is developing a dual-frequency intravascular imaging catheter with an IVUS and an IVPA transducer. A low-frequency transducer is used for the IVPA signal because it was shown that more than 80 % of the PA signal power lies below a frequency of 8 MHz [42]. On the other hand, a high-frequency transducer is used for IVUS because this increases resolution [36]. However, a higher resolution decreases the penetration depth, but the IVUS imaging depth only needs to be a few millimeters. Therefore, two transducers with a center frequency of 5 and 50 MHz are used to gain as much signal as possible.

The Kaminari system will have two lasers with wavelengths of 1200 nm and 1700 nm to excite the PA effect. These two wavelengths are used because the light absorption by lipids is stronger than by water at these wavelengths [43], as visible from the absorption spectra in Figure 2.5. This difference allows for the differentiation and specific imaging of the lipids. Lasers of both wavelengths are used to maximally profit from the high light absorption by lipid.

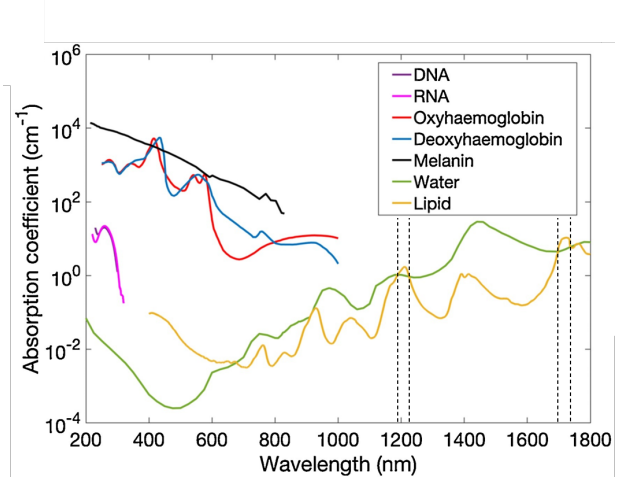

Figure 2.5: Absorption spectra of different media. Adapted from [43]

A schematic overview of an intravascular imaging catheter is depicted Figure 2.6 to illustrate the Kaminari Medical catheter. Two optical fibers, one for each wavelength, and a coaxial cable go into the catheter. Laser pulses generate a light bundle that illuminates the tissue to induce the IVPA signals. The tissue absorbs this light of a specific wavelength and transmits an omni-directional sound wave. The transducers receive this sound wave, which is captured as RF data. High-voltage pulses induce a sound wave from the high-frequency IVUS transducer. Interaction with the tissue causes echoes that are received by the IVUS transducer. Transmitting and receiving the IVUS or IVPA signals is a sequential process. First, the IVPA signal is triggered by a laser beam of the first wavelength and the IVPA signal is received. Then, a similar process for the second wavelength is executed before the sound waves are transmitted and received which results in the IVUS signal. During this signal acquisition, the catheter is pulled back from the distal end of the coronary artery while rotating to image the entire arterial wall.

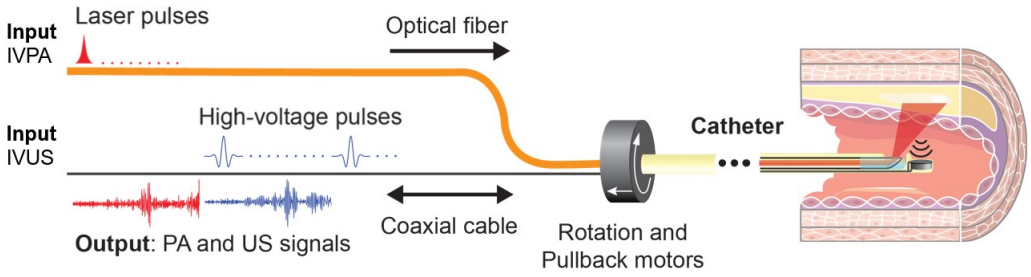

Figure 2.6: A schematic overview of the IVUS and IVPA imaging catheter. The IVPA input are laser pulses, which generate an optical light bundle that triggers the PA effect resulting in a sound wave that a transducer can capture. The IVUS is triggered by high-voltage pulses, which results in the transducer sending out a sound wave and capturing the echoes. Adapted from [44]

2.4. IVUS and IVPA Image Reconstruction

As explained before, IVUS can be used to visualize the vessel morphology and the different vessel layers because the acoustic impedance differences at tissue boundaries generate echoes that are detected by the IVUS transducer. The IVPA signal can be overlaid with the IVUS image, which provides localization of the lipids. The conventional way to reconstruct IVUS and IVPA images is by stacking the RF data captured by the rotating transducer. The received RF data will be referred to as RF lines because a line of RF data is captured for each transducer position while rotating. RF line refers to a line of data that contains the amplitude of the received pulse-echo US or IVPA signal as a function of time given in samples, which is also called an A-line. Stacking these RF lines means that an image grid is filled by placing the RF lines next to each other. Since the RF lines are captured in a rotational scanning approach, a scan conversion is applied to generate a cross-sectional image of the artery.

3

Virtual Source Synthetic Aperture Beamforming with Coherence Factor Weighting

3.1. Introduction

As previously discussed, a high LR and SNR are important in IVUS and IVPA imaging for enhanced interpretation of artery wall structures and abnormalities. Besides hardware design choices such as using a focused transducer, a high LR and SNR could be achieved by beamforming techniques. One of these techniques is the VSSA with CFW as proposed by Yu et al. (2017) [29]. The VSSA is a beamforming technique to improve image quality by combining the time-delayed signal of multiple RF lines. This way, all available information about the image signal is considered in the image reconstruction [29]. This Chapter mainly describes the algorithm implementation based on the VSSA and CFW by Yu et al. which performance is evaluated to answer the second research question:

Research Question 2

What is the image quality improvement achieved by implementing the state-of-the-art image reconstruction method compared to the original reconstruction?

Furthermore, the algorithm performance will be evaluated. The theory behind the VSSA and CFW will be described below. Section 3.2 describes the implementation of the algorithm and the data acquisition to obtain experimental and simulated data to evaluate the performance of the algorithm. The results of the intermediate steps of the algorithm are reported, and the final image reconstruction is given in Section 3.3. Lastly, Section 3.4 summarizes the performance of the algorithm and evaluates the implementation method.

3.1.1. VSSA and CFW Theory

Reference [29] is used for all statements made in this section unless reported otherwise.

The principle of the VSSA is to sum the delayed RF lines from adjacent transducer positions that contain signal of the same imaging area. This overlap is determined by the US beam shape of each RF line, which is an hourglass-shaped beam with a near field, natural focus, and a far field [36, 37]. When multiple beam shapes overlap the same imaging area, the corresponding RF lines are delayed and summed up to reconstruct a new RF line through that area. This method allows for synthesizing a larger aperture than the original transducer aperture [29]. This is only valid when the transducer rotates over a radius instead of over its rotation axis. A larger synthetic aperture improves the LR [45, 46], which can be calculated by Equation 3.1 [47].

$$LR = \lambda \cdot \frac{z_f}{D} \tag{3.1}$$

λ is the wavelength, D is the diameter of the transducer, and z_f is the natural focus depth. The ratio between the diameter and natural focus depth is also referred to as the f-number of the transducer. When a larger aperture is synthesized, D will increase, decreasing the LR. The smaller the LR value, the better the resolution.

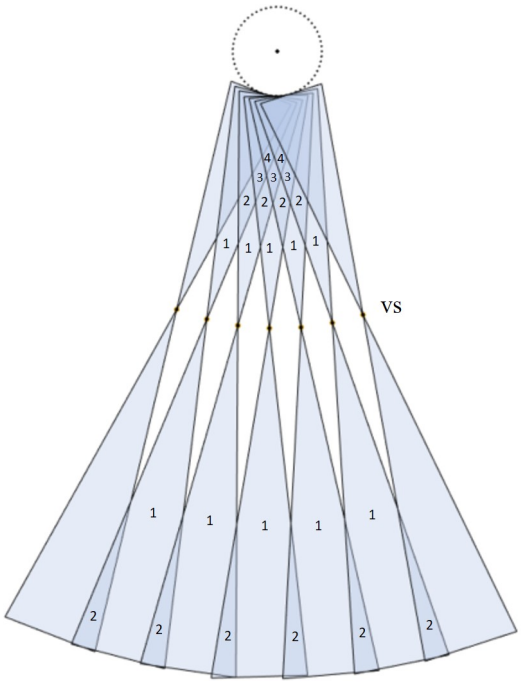

Figure 3.1: Concept of the beam overlap in a rotational scanning approach. The number shows the number of overlapping beams, which is the number of RF lines that should be delayed and summed to find the newly reconstructed RF lines. vs is the virtual source at the natural focus of the beam. Adapted from [29]

.

The concept of the overlapping beam shapes is illustrated in Figure 3.1 with oversimplified beam shapes originating from a VS. In the VSSA case, a VS is placed at the natural focus of the beam to simulate that the natural focus is the source of the US beams. Using a VS at the natural focus is believed to allow for focusing by coherent compounding, i.e., optimal alignment of the RF lines coming from different transducer positions [48]. This alignment of the RF lines by delaying is illustrated in Figure 3.2, which also shows that summation of the delayed RF lines results in a higher signal amplitude. Figure 3.2 shows the concept for three transducer positions with beam shapes that all contain signal for the same imaging point, the blue dot. Three time delays are calculated based on the distance between the imaging point and the VS of each RF line. Hence, the largest delay needs to be applied for the third RF line furthest from the imaging point. The final VSSA signal is obtained by applying these time delays and taking the sum of the result. This is described by Equation 3.2.

$$S_{vssa}(t) = \sum_{i=1}^{N} RF(i, t - \Delta t) \tag{3.2}$$

where N is the number of RF lines that overlap the same imaging point.

A downside of the VSSA method is that besides increasing the main lobe, which is the signal amplitude, the sidelobe amplitude is also increased. The sidelobes are the amplitude peaks on either side of the main lobe that do not account for signal value but for noise. A higher sidelobe amplitude can decrease the resolution and contrast. The proposed method in [29] to reduce these sidelobes is a Coherence Factor Weighting (CFW). This weight is a value between 0 and 1 that gives a measure for coherence between the delayed RF lines. The higher the coherence, the more weight is applied.

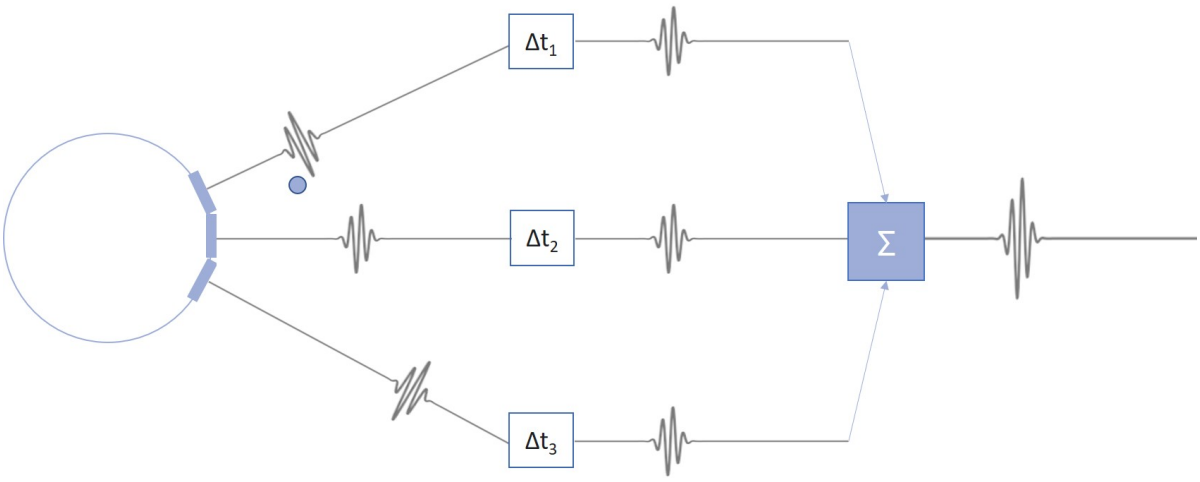

Figure 3.2: Schematic overview of the VSSA principle. The circle illustrates the catheter with three transducer positions highlighted. The RF lines of three transducer positions are shown, which show the signal for the same imaging point at different times along the RF line. The imaging point is indicated with the blue dot between the first and second RF lines. Delaying the RF lines leads to optimal summation resulting in a higher signal amplitude

3.2. Materials and Methods

This section describes the algorithm implementation and the experimental and simulated data acquisition. The algorithm is initially developed for IVUS data and characteristics.

3.2.1. Implementation

The VSSA algorithm is implemented to directly reconstruct the image pixels instead of synthesizing new RF lines as described in [29]. Developing this pixel-based implementation was decided because it allows for the pre-computation of a large part of the algorithm, which will reduce the computational time.

Four pre-processing steps are executed before the RF data can be used as input to the algorithm. The RF data that is input before pre-processing are the RF lines containing the amplitude of the signal as a function of time in samples. First, similarly to [29], a bandpass filter is applied to limit the bandwidth to the most relevant frequencies. A fourth-order Butterworth filter filters the data with a pass band of 30 to 70 MHz. Second, the IVUS data contains ring-down artifacts, which are bright halos close to the transducer occurring due to acoustic oscillations in the transducer [36]. These artifacts are removed by setting the number of samples in which they occur to zero. Third, the Hilbert transform is taken to obtain I/Q data. I/Q data is complex data that contains amplitude and phase information. Using I/Q RF data as input is important because the phase information contains correlations between adjacent RF lines [49]. Lastly, a Time Gain Compensation (TGC) is applied to compensate for the tissue attenuation that decreases the signal energy. The TGC is implemented such that every sample is increased with a certain gain, which is calculated using

$$TGC = 1 + 2 * \frac{j}{N_{samples}} \tag{3.3}$$

where j is the jth sample of the total number of samples ($N_{samples}$). The factor 2 is an arbitrary number and can be increased when stronger compensation is required.

The algorithm outputs a VSSA signal value and a CFW weight per pixel. Several steps need to be taken to obtain that output. First, the rotational geometry of the beam shape overlap is needed to generate the N mask, which contains a value per pixel for the number of overlapping RF. Then, the distances between the image pixel and VS of the overlapping RF lines are calculated to allow for the calculation of the time delays as a next step. Subsequently, these time delays are applied to the RF lines before summation to obtain the final VSSA signal. Lastly, the VSSA signal is multiplied by the CFW. Log compression is used to generate a VSSA and a VSSA+CFW image. An overview of this algorithm pipeline is depicted in Figure 3.3. The algorithm steps are explained in more detail below.

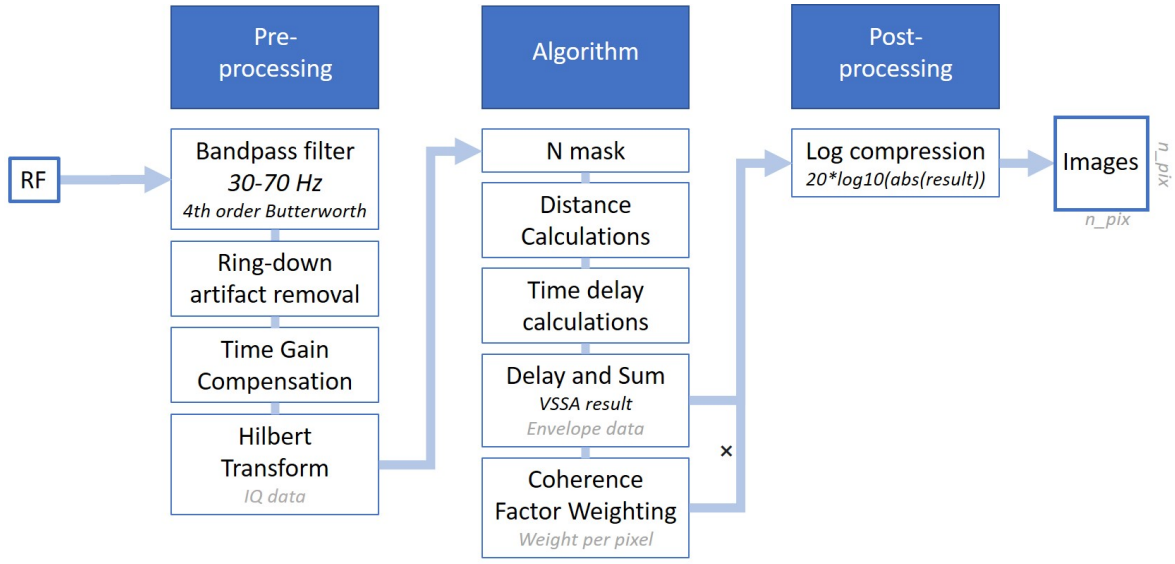

Figure 3.3: Overview of the full algorithm pipeline. Four pre-processing steps are taken to obtain bandpass filtered and time gain compensated I/Q data as the algorithm input. Next, the algorithm consists of five steps. Finally, the VSSA and VSSA+CFW result is visualized after log compression.

N Mask

The first step is to find the number of overlapping beams per pixel (N). Starting with defining the geometry of the beam shapes based on the half opening angle that can be defined by Equation 3.4 [29].

$$\alpha = arctan(\frac{D}{2 \cdot z_f}) \tag{3.4}$$

where D is the diameter of the transducer. z_f is the natural focus depth seen from the transducer surface, which can be calculated using

$$z_f = \frac{D^2}{4 \cdot \lambda} \tag{3.5}$$

λ is the wavelength, which can be calculated by $\lambda = c/f_c$. c is the speed of sound, and f_c is the center frequency of the transducer. α determines the shape simplified beam as illustrated in Figure 3.4a. The final beam shape is depicted in Figure 3.4b with a -3 dB beam width at the natural focus instead of treating the natural focus as an infinitely small point [29]. This beam width equals half the transducer diameter D [37]. The coordinates of the red dots need to be calculated to plot the geometry. The coordinates of the edge points that span the beam at the transducer surface are calculated by adding or subtracting the beam width to or from the transducer center coordinates. The edge points at the end of the far field are calculated similarly by adding or subtracting the beam width from the axis of the beam. Furthermore, this addition or subtraction occurs under an angle due to the rotation of the catheter. The beam widths at the near field and far field are illustrated in Figure 3.4a by L_{NF} and L_{FF} and can be calculated as follows:

$$L_{NF} = tan(\alpha) \cdot z_f \tag{3.6}$$

$$L_{FF} = tan(\alpha) \cdot (z - z_f) \tag{3.7}$$

where z is the total imaging depth. The overlap depends on the imaging depth, and the number of RF lines acquired per rotation, which is the line density. The more RF, the closer the beam profiles are to each other, which results in more overlap. Once the geometry of the beam shapes is defined, the N mask can be generated. This is done by plotting the beam shapes for each transducer position on a pixel grid with zeros. Each beam shape adds +1 to the pixels that it covers. Eventually, this leads to a pixel grid with the N defined for each pixel.

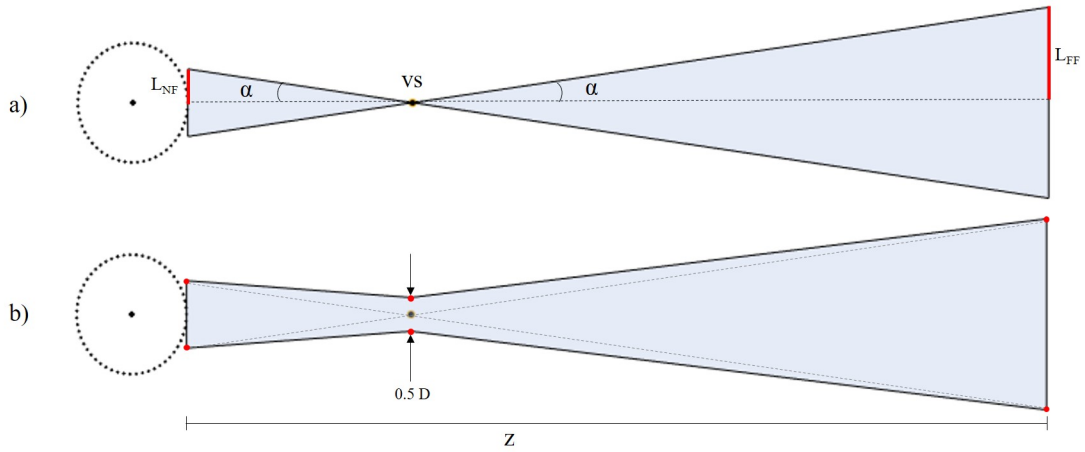

Figure 3.4: a) The simplified beam shape of two cone shapes. α determines the convergence to and divergence from the focal point at z_f. b) The more realistic beam shape with a -3 dB beam width, equal to 0.5 $\cdot$ D, at the natural focus instead of an infinitely small point. The red dots are the edge points needed to plot all beam shapes used to generate the N mask. The simplified beam shape of a) is illustrated with the dashed line in b).

Distance and Time Delay Calculations

The next step is calculating the time delays with which the N RF lines per pixel need to be delayed. The time delay Δt can be calculated by using Equation 3.8 and 3.9.

$$\Delta t = 2 \cdot sgn(z_p - z_f) \cdot \frac{[abs(r) - r']}{c} \tag{3.8}$$

$$r = z_p - z_f \tag{3.9}$$

where r is the depth distance between the pixel depth (z_p) and the VS depth (z_f). r' is the direct distance between the pixel and the VS. This is illustrated in Figure 3.5 for a rotational scan.

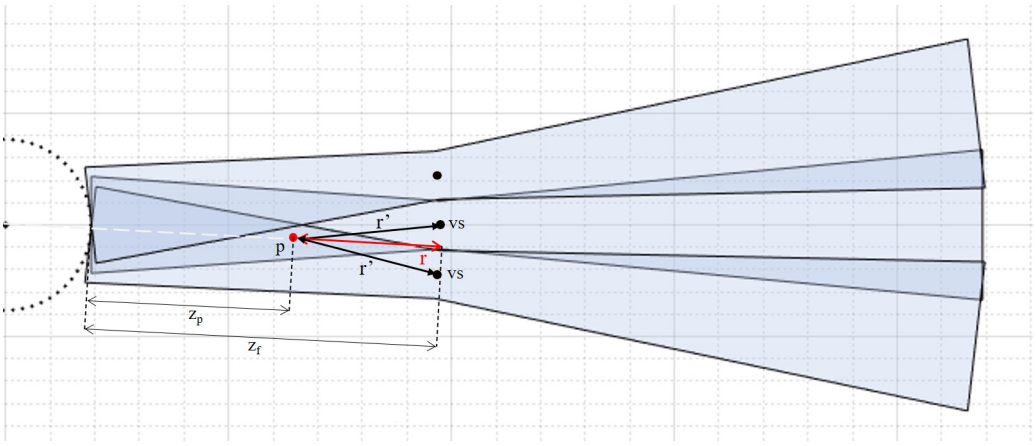

Figure 3.5: The red dot is a randomly picked imaging point in pixel p. Pixel p falls within an area that is covered by two RF, thus N = 2. Therefore, two r' need to be calculated, which is the distance from the pixel to the two virtual sources (VS) of the overlapping RF. The red line represents r, which is the depth distance from the pixel to the natural focus depth, i.e., VS depth. The two time delays for pixel p are determined based on the distance of the two r' respective to r

r is calculated by subtracting z_f from z_p, where the latter is the Euclidean distance from the transducer surface to the pixel p. This r is calculated for each pixel. The pixels in the near field have a negative value for r, and the far field pixels have a positive value for r. The r' is the distance from the pixel p to the VS of the RF lines that overlap pixel p. Thus, there are N r' values per pixel because a unique time delay is calculated for each RF line that overlaps pixel p. In conclusion, the following variables are calculated per pixel: the number of overlapping RF lines (N) and their RF indices, the distance r, and the N distances r'. Subsequently, Δt can be calculated N times for each pixel by

Equation 3.8. The time delay (Δt) is calculated in seconds because the r and r' are given in meters and the speed of sound c in meters per second. This needs to be converted to a time delay in samples because the RF lines are stored in samples. This conversion to obtain a time delay in samples is performed by multiplying the time delay in seconds with the sampling frequency.

Delay and Sum
The delay is applied by selecting the sample value of the RF line that corresponds with the pixel depth and shifting this with Δt to obtain the time-delayed signal. This is done N times per pixel, and the results are summed up to obtain the VSSA signals for all pixels as described in Equation 3.2. The time delay should be negative before the VS (near field) and positive after (far field) because the time delays are calculated relative to the VS instead of the transducer surface.

Coherence Factor Weighting
The CFW is calculated for each pixel by Equation 3.10 [29].

$$CFW = \frac{|\sum_{i=1}^{N} RF(i, t - \Delta t)|^2}{N \sum_{i=1}^{N} |RF(i, t - \Delta t)|^2} \tag{3.10}$$

This shows that the coherency is calculated based on a ratio between the absolute square of the sum of the delayed RF values and the sum of the absolute square of the delayed RF values. It was decided to use the same input data as for the rest of the algorithm, which means the RF in Equation 3.10 is the time gain compensated I/Q RF data. The analytical data was used instead of the raw data because, as mentioned before, the phase contains information on the correlations between adjacent RF lines [49]. The CFW calculation gives a weight between 0 and 1 for every pixel. This W_{cfw} is 0 when there is no coherence and 1 for perfect coherence. Multiplying S_{VSSA} by W_{CFW} gives the final signal for the VSSA with CFW.

3.2.2. Data

Experimental Data
Experimental data is acquired from a stent and a human artery. The IVUS transducer used for these experiments has a center frequency of 50 MHz, a height of 532 μm, and a width of 433 μm. The IVPA transducer has a bandwidth of 1 to 10 MHz, with a center frequency estimated at 5 MHz. The physical offset of the catheter, i.e., the distance between the rotation axis and the transducer surface, is 383 μm. The data is acquired up to 7 mm, seen from the transducer surface, with a rotational speed that results in 256 RF per cross-sectional image. The speed of sound is estimated at 1481 m/s. The sampling frequency is 400 MHz.

Simulated Data
The Matlab Ultrasound Toolbox (MUST) [50] was used to simulate IVUS data to enable validation of the algorithm. The goal is to simulate the RF lines captured by a rotating transducer of a noiseless medium with point scatterers. The RF echo simulator of the MUST, called *SIMUS*, is used to simulate the RF data received from the point scatterers that act as monopole sources [50]. The rotating single-element transducer is simulated using a convex array of transducers under a curvature equal to the catheter's radius. The elements in the convex array should transmit and receive individually and after each other. Initially, all transmit apodization values for the elements were set to 0. This value was only set to 1 for the active element to save the RF lines received by that element. Subsequently, the apodization of that element is set back to 0, and the next element to 1, and so forth. The parameters used in the simulation are based on the Kaminari Medical IVUS transducer. The parameters are summarized in Table 3.1. Besides, the pressure field of the US beam with the same parameters is simulated using *PFIELD* [51].

The RF data was simulated for seven point scatterers located at different depths along the y-axis. The depths are 0.5, 1, 1.6, 2, 3, 4, and 5 mm for scatterers 1 to 7, respectively. This allows for a comparison with the algorithm results because it is known which RF line is closest to these imaging points. Hence, it can be used as a reference for the algorithm and simulated data results. The time delays of the data simulation are used as the ground truth. These are calculated per scatterer by cross-correlation. The MATLAB function *xcorr* is used to find the number of samples that the RF line need to

be delayed with to align with the reference RF. The number of RF lines for which the time delays are calculated is based on an arbitrarily set threshold for the RF amplitude to find sufficient time delays to allow comparison to the algorithm.

Table 3.1: Parameters of the IVUS data simulation in MUST.

Parameter	Value	Parameter	Value
Central Frequency (f_c)	50 MHz	Transducer width	433 μm
Sampling Frequency (f_s)	400 MHz	Transducer Height	532 μm
Speed of sound (c)	1481 m/s	Radius of curvature	383 μm
-6 dB fractional bandwidth	70%	Pitch	9.44 μm

3.2.3. Image Reconstruction and Quality

The algorithm will be used to reconstruct images for the simulated and experimental data. These images will be depicted with a dynamic range of 30 dB below the local maximum of the image.
The image quality of the simulated data reconstruction is quantified by two image quality metrics, namely the LR and the Signal-to-Noise Ratio (SNR). The LR is quantified as the -6 dB beamwidth of the line profile generated by the summation of multiple image rows that contain the scatterer signal. A summation of multiple rows is used because the scatterer appears under an arc in the final images. The simulated data is noiseless, so the SNR is quantified after adding random noise with a noise level comparable to the raw experimental stent data. The noise level is determined such that the simulated data with added noise has a similar SNR to the SNR of the raw stent data. The SNR is calculated in dB as follows [27, 52]:

$$SNR = 20 \cdot log_{10}(\frac{I_{signal}}{I_{noise}}) \tag{3.11}$$

where I_{signal} is the signal intensity taken as the maximum envelope amplitude over a range of samples that contain signal. The I_{noise} is the noise intensity taken as the mean envelope amplitude value of all samples outside the signal sample range [52]. The SNR is calculated for each scatterer.

3.3. Results

This results section will first describe the outputs of the algorithm applied to the simulated IVUS data. The time delays calculated by the algorithm will be compared with the time delays determined from the simulated data by cross-correlation, which is used as the ground truth. Furthermore, the beam profile of the IVUS data is simulated to compare this with the beam shape used to determine the N mask. Lastly, the images are reconstructed for the simulated and experimental data by original reconstruction, the VSSA, and the VSSA with CFW.

3.3.1. Algorithm Outputs

N mask

The N mask shows a value for each pixel that indicates how many RF lines overlap that pixel (N). The N mask depends on the imaging depth, the number of pixels used for reconstruction, and the number of transducer positions per rotation. The algorithm is executed to obtain an IVUS image of 2001x2001 pixels up to an imaging depth of 7 mm. Besides, the data is acquired with a line density of 256 RF lines per rotation. The half opening angle of the beam shape (α) is 7.8 degrees, as calculated by Equation 3.4. The maximum number of RF lines overlapping a pixel is 42. The beam shapes overlap more in the near field because the beams are distributed over a smaller radius than in the far field. Therefore, The N is larger in the near field than in the far field. The smallest N is found at the VS because the beam shape is narrowest at that location.

Time Delay Comparison

The calculated time delays for RF lines that overlap the seven point scatterers in the simulated IVUS data are visualized in Table 3.2 and 3.3. Table 3.2 contains the time delays calculated by the VSSA algorithm. Table 3.3 contains the time delays determined by cross-correlation, which is further referred

to as the ground truth. The ground truth time delays are determined for all RF lines with a maximum amplitude higher than the arbitrary threshold of -60 dB. This threshold was set to -60 dB because it gives a sufficient number of time delays to allow for comparison with the time delays calculated by the algorithm.

The RF line with index 65 is highlighted in blue because this is the reference beam that travels straight through the point scatterers. The delays are given in samples. For the algorithm, the delays have a sign difference for scatterers in the near field and the far field because the time delay needs to be negative in the near field and positive in the far field when $t - \Delta t$ is applied as described in Equation 3.2. Table 3.3 shows that this sign difference is not visible in the time delays of the data simulation that are determined by cross-correlation. The time delays calculated by the algorithm are larger than the ground truth when comparing the time delay per RF index. Especially there is a substantial difference in the magnitude of the time delays for scatterer 3, which was placed at natural focus at 1.6 mm. Furthermore, the time delays calculated by the algorithm increase when the image pixel is closer to the VS. This is as expected because the relative difference between r and r' increases when positioned closer to the VS, leading to a larger time delay, as seen in Equation 3.8. On the other hand, the ground truth time delays decrease with depth. The time delays are largest for scatterer 1 and smallest for scatterer 7 (Tab. 3.3).

Table 3.2: Time delays calculated by the algorithm for the simulated data of the seven point scatterers. Time delays are given in number of samples.

scatterer																																						
1	RF idx	65	64	66	63	67	62	68	61	69	60	70	59	71	58	72	57	73	56	74	55	75	54	76	53	77	52	78	51	79	50	80	49	81	48	82
	Time delays	0	0	0	0	1	1	1	2	2	2	3	4	4	5	6	7	7	8	9	10	11	13	14	15	16	18	19	20	22	23	25	27	28	30	32
2	RF idx	65	64	66	63	67	62	68	61	69	60	70	59	71	58																					
	Time delays	0	0	1	1	2	3	4	5	6	7	9	11	13	15																					
3	RF idx	65	64	66	63	67																														
	Time delays	-6	-19	-32	-45	-58																														
4	RF idx	65	64	66	63	67	62																													
	Time delays	0	-1	-1	-3	-5	-7																													
5	RF idx	65	64	66	63	67	62	68																												
	Time delays	0	0	-1	-2	-3	-5	-7																												
6	RF idx	65	64	66	63	67	62	68																												
	Time delays	0	0	-1	-2	-3	-4	-6																												
7	RF idx	65	64	66	63	67	62	68	61																											
	Time delays	0	0	-1	-1	-2	-4	-5	-7																											

Table 3.3: Time delays determined by cross-correlation for the simulated data of the seven point scatterers. Time delays are given in number of samples.

scatterer																																						
1	RF idx	57	58	59	60	61	62	63	64	65	66	67	68	69	70	71	72																					
	Time delays	-13	-10	-7	-5	-3	-2	-1	0	0	-1	-2	-3	-5	-7	-10	-13																					
2	RF idx	53	54	55	56	57	58	59	60	61	62	63	64	65	66	67	68	69	70	71	72	73	74	75	76													
	Time delays	-13	-11	-9	-7	-6	-4	-3	-2	-1	-1	0	0	0	0	-1	-1	-2	-3	-4	-6	-7	-9	-11	-13													
3	RF idx	52	53	54	55	56	57	58	59	60	61	62	63	64	65	66	67	68	69	70	71	72	73	74	75	76	77											
	Time delays	-12	-10	-8	-7	-6	-4	-3	-2	-1	-1	0	0	0	0	0	0	-1	-1	-2	-3	-4	-6	-7	-8	-10	-12											
4	RF idx	53	54	55	56	57	58	59	60	61	62	63	64	65	66	67	68	69	70	71	72	73	74	75	76													
	Time delays	-9	-8	-6	-5	-4	-3	-2	-1	-1	0	0	0	0	0	0	-1	-1	-2	-3	-4	-5	-6	-8	-9													
5	RF idx	53	54	55	56	57	58	59	60	61	62	63	64	65	66	67	68	69	70	71	72	73	74	75	76													
	Time delays	-9	-8	-6	-5	-4	-3	-2	-1	-1	0	0	0	0	0	0	-1	-1	-2	-3	-4	-5	-6	-8	-9													
6	RF idx	56	57	58	59	60	61	62	63	64	65	66	67	68	69	70	71	72	73																			
	Time delays	-5	-4	-3	-2	-1	-1	0	0	0	0	0	0	-1	-1	-2	-3	-4	-5																			
7	RF idx	58	59	60	61	62	63	64	65	66	67	68	69	70	71																							
	Time delays	-3	-2	-1	-1	0	0	0	0	0	0	-1	-1	-2	-3																							

Simulated Beam Profile

The IVUS beam profile was simulated in MUST based on the IVUS transducer characteristics and is depicted in Figure 3.6 clipped at -3, -6, and -20 dB. The natural focus was calculated to be located at 1.6 mm. This lies in the highest intensity area of the beam profile. However, the area with the highest sensitivity is not a single point but an elongated area. Lastly, the beam profiles show a weak focus.

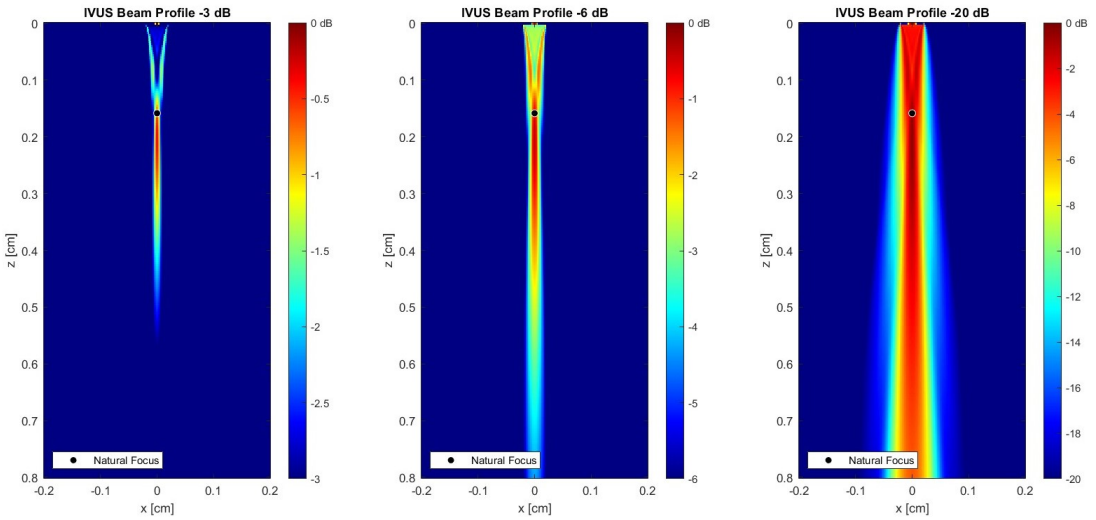

Figure 3.6: Three beam profiles for -3, -6, and -20 dB. The black dot is the natural focus which was calculated to be at 1.6 mm depth.

3.3.2. Image Reconstruction

Simulated Data

The algorithm results for the simulated IVUS data of the seven point scatterers are shown in Figure 3.7. A decrease in LR is seen in the VSSA result, except for the third point scatterer, which is located at the VS. Generally, the further away the scatterer is from the VS, the worse the lateral resolution is. Remarkably, the curvature of the point scatterers in the near field (scatterer 1 and 2) is oriented opposite to the curvature of the far field scatterers. The CFW seems to increase the amplitude at the center of the scatterer.

The quantified image results for LR and SNR are summarized in Table 3.4. The method to quantify the LR and SNR is explained in Section 3.2.3. The VSSA strongly deteriorates the LR, which is partly recovered after adding CFW. However, the LR of the VSSA+CFW is only better than the original reconstruction for some scatterers in the far field. The SNR is decreased due to the VSSA. Adding the CFW continues this trend, even resulting in SNR values below 1.

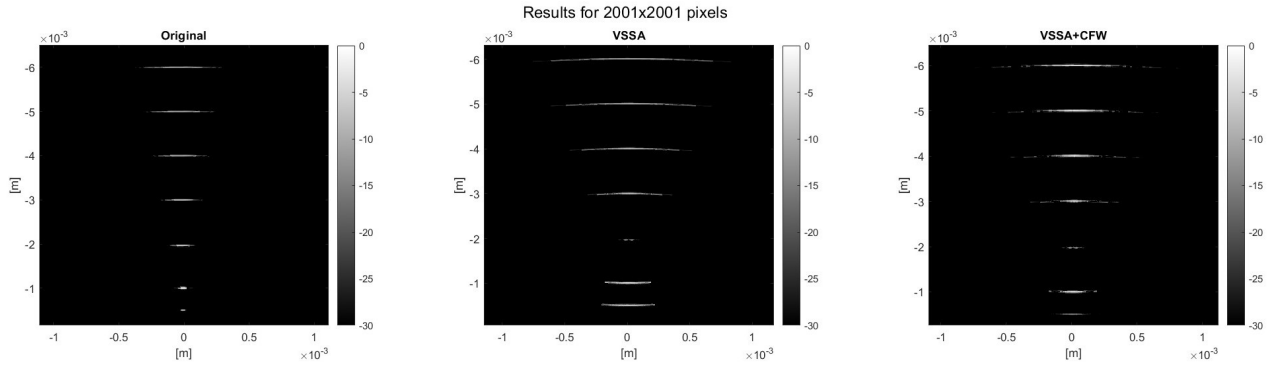

Figure 3.7: Results of the simulated data. From left to right: The reconstructed images by the original reconstruction, the VSSA, and the VSSA+CFW .

Table 3.4: Lateral resolution (LR) and Signal-to-Noise Ratio (SNR) values for the original image reconstruction, the VSSA result, and the VSSA+CFW result of the simulated IVUS data. The SNR is quantified for the simulated data after noise addition with a comparable noise level to the experimental data.

Scatterer	1	2	3	4	5	6	7
Lateral Resolution Original [μm]	29.0	43.6	94.4	159.7	246.8	290.3	362.9
Lateral Resolution VSSA [μm]	290.0	210.5	79.8	217.8	362.9	544.4	725.9
Lateral Resolution VSSA+CFW [μm]	384.7	130.7	79.8	123.4	145.2	261.3	413.7
SNR [dB] Original	7.3	11.9	6.8	4.5	4.5	3.1	3.2
SNR [dB] VSSA	6.7	5.1	1.5	1.8	1.4	0.6	1.7
SNR [dB] VSSA+CFW	5.4	1.5	0.9	0.9	1.3	0.5	2.8

Experimental Data

The algorithm results for the stent data is shown in Figure 3.8 and the results for the artery data are shown in Figure 3.9. All images are visualized with a 30 dB dynamic range below the local maximum of the image to allow for a fair comparison. Both figures show the original reconstruction, the reconstruction by only applying VSSA beamforming, and lastly by VSSA combined with CFW. The original reconstruction is the image that is reconstructed by stacking the band-pass filtered RF data and converting it to a polar image. Figure 3.8 with the stent shows that the VSSA decreases the lateral resolution but does increase the intensity of the stent struts. After adding the CFW, the lateral resolution is visually improved. However, the image remains rather noisy behind the stent struts. The VSSA result for the artery data in Figure 3.9 shows image quality deterioration in resolution and contrast rather than improvements. The VSSA+CFW image has an inferior image quality.

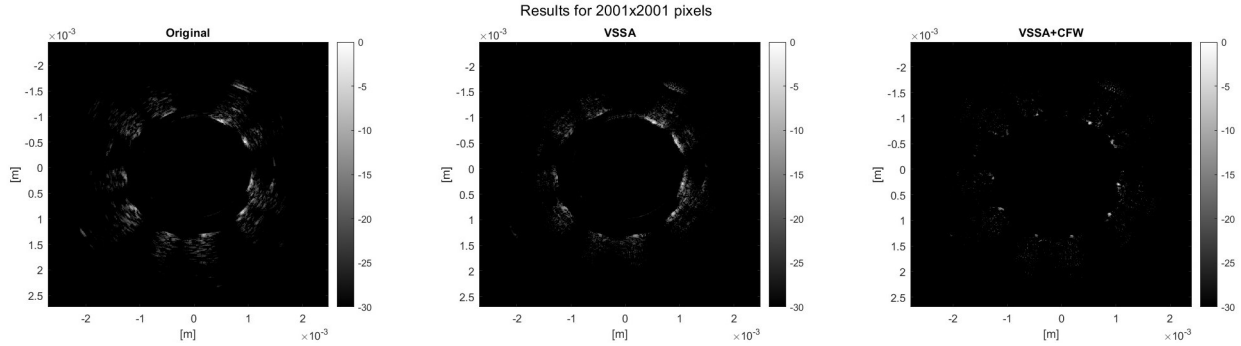

Figure 3.8: Results of the stent data. From left to right: The reconstructed images by the original reconstruction, the VSSA, and the VSSA+CFW. All images are displayed with a 30 dB dynamic range below the local maximum of the image.

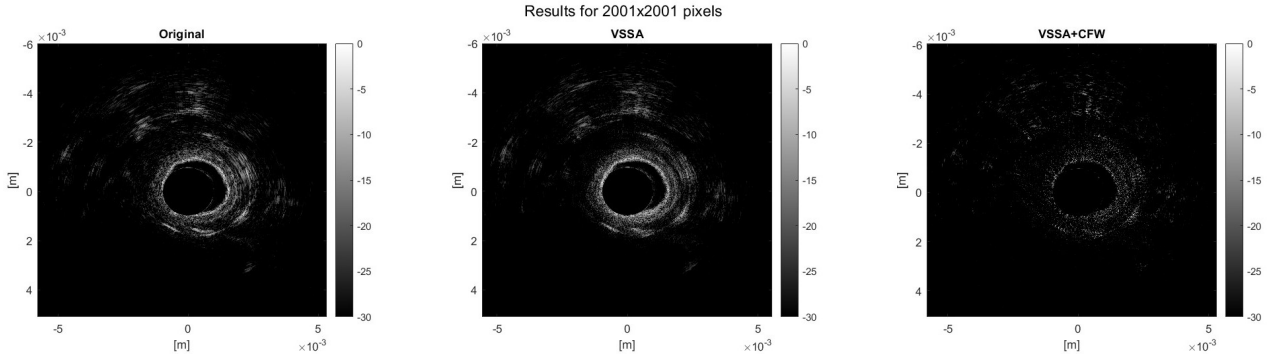

Figure 3.9: Results of the artery data. From left to right: The reconstructed images by the original reconstruction, the VSSA, and the VSSA+CFW. All images are displayed with a 30 dB dynamic range below the local maximum of the image.

3.4. Discussion

3.4.1. Performance

Overall, the results of the VSSA and CFW algorithm visually do not show the expected image quality improvement. The VSSA-only images visually have a lower image quality in lateral resolution and contrast for the artery and stent data compared to the original image. The VSSA-CFW results do show lateral resolution improvements for the stent data. However, the stent image does remain rather noisy. The VSSA-CFW shows no improvement for the artery data at all.

It was expected that similar results as in the original paper could be achieved since similar transducer characteristics and the same algorithm specifics were used. The algorithm was applied to data from a 40 MHz flat US transducer with a natural focus at 1.7 mm in [29], whereas a 50 MHz flat US transducer with its natural focus at 1.6 mm was used in this work. However, the results do not show similar image quality improvements in lateral resolution and signal-to-noise ratio (SNR). Several observations indicate that the assumption that the VS should be placed at the natural focus could be incorrect. First, there is a substantial size difference between the time delays calculated by the algorithm and determined by cross-correlation from the simulated data. Since the time delays are calculated with respect to the VS, an incorrectly placed VS could cause a wrong calculation of the time delays. Second, the time delays for the data simulation decrease with depth instead of finding the largest time delays near the VS. This indicates that the actual VS lies close to, or even behind, the transducer because that is where the largest time delays are found. Lastly, the sign difference, as observed in the algorithm results, is not visible in the simulated data results. The simulation time delays have the same sign as the scatterers in the far field for the algorithm results. This indicates that all scatterers should actually lie in the far field, meaning a VS that should lie behind or close to the transducer.

Moreover, the simulated beam profiles, as shown in Figure 3.6, show that the beam is not as focused as the beam shape assumed in the algorithm. The beam shape used in the algorithm is more focused than the simulated beam profile. This suggests that the used beam shape does not accurately represent the actual IVUS beam shape. Yu et al. [29] base their assumption that the VS should lie at the natural focus of the beam on studies by Passman and Ermert [53, 54]. The assumption is based

on simulations where a Rayleigh-Sommerfeld integral in the time domain is used to simulate the field distribution of a focused transducer [54]. However, Yu et al. performed their experiment with a flat transducer. In this work, the IVUS data is also transmitted and received by a flat transducer. This is validated by the simulated IVUS beam profile, which shows only a weakly focused beam.

To conclude, the algorithm as currently implemented with the VS at the natural focus does not provide the desired image quality improvement. This is most likely due to incorrect beam shape visualization and the invalid assumption that the VS should lie at the natural focus of the beam. Next, Chapter 4 aims to optimize the algorithm to achieve the desired image quality improvement.

3.4.2. Implementation

It was decided to develop a pixel-based implementation where the image pixel values are reconstructed directly by delaying and summing the RF lines that overlap the pixel. This allows for a computational benefit because four out of five algorithm steps can be precomputed for fixed transducer characteristics. Once these steps are precomputed, only the Delay and Sum step has to be executed for each image. The part that can be precomputed has a computational time of 148 seconds for 2001x2001 pixels which only has to be executed once for the same dataset. The computational time of the last step to obtain the final VSSA and CFW values takes 27 seconds for one image of 2001x2001 pixels.
However, this implementation also has some limitations. First, the implementation assumes that the catheter center is equal to the image center, which would be true in an ideal scenario. However, due to the obliquity of the catheter and vessel curvature or movements, it is more likely that the catheter is only sometimes exactly in the middle. This can cause a small offset in the distance calculations when the actual catheter position is not in the image center. Therefore, the time delays will be larger or smaller than they should be, resulting in incorrect alignment of the RF.
Second, the implementation is pixel-based, meaning several unit conversions are needed to enable discretization. An example is the conversion of the time delays in seconds to samples because the time delays need to be applied to an RF line which is a function of time given in samples instead of seconds. This conversion is executed by multiplying the time delays in seconds with the sampling rate. Conversions like these often need a rounding factor because the number of samples needs to be an integer. In this case, the *round* function in MATLAB was used, which rounds the value to the nearest integer. Other options could be to round towards positive or negative infinity, which rounds to the nearest integer smaller or greater than the value that needs rounding. The effect of these three rounding methods was evaluated and showed almost similar performance in LR and maximum image intensity, but rounding to the nearest integer showed slightly better results. Besides, the distance calculations from pixels to VS are calculated from the pixel center, which will be more accurate to the true values when more pixels are used. However, there is a trade-off between this accuracy and the computational time because this will increase when more pixels are reconstructed. Moreover, the pixel-based implementation deals with discretization effects which will be discussed in Chapter 5.
Another potential limitation is the TGC method which pre-processes the data to compensate the IVUS data for energy loss due to tissue attenuation. A more accurate method would be to compensate for the exact tissue attenuation based on the attenuation coefficients of the medium. Since the medium exists of artery tissue and water, air, or blood in the lumen, depending on the acquisition method, it is quite complicated to compensate for this due to the different attenuation coefficients. Moreover, it is complicated to establish the exact attenuation coefficient for the artery tissue because it depends on various factors like water content or collagen content [55].

4 Optimization

4.1. Introduction

Chapter 3 describes a pixel-based implementation of the VSSA with CFW based on [29]. However, the reconstructed images do not show the image quality improvements in LR and SNR as expected based on [29]. This chapter aims to optimize the algorithm for maximum image quality improvement for the Kaminari Medical IVUS and IVPA catheter. This chapter will therefore describe the answer to the third research question.

Research Question 3

What are the optimal algorithm parameters to reconstruct high-quality images from data acquired with the Kaminari Medical IVUS and IVPA catheter?

First, a theoretical validation of the principle behind VSSA will be performed to find what effect should be expected from the algorithm on the image quality. These findings can be used to guide the optimization to find the parameters that yield the highest obtainable image quality. Once the optimization method and the optimized version of the algorithm are established, the image quality will be evaluated to provide an answer to the fourth research question.

Research Question 4

What is the image quality improvement after optimization compared to the original reconstruction?

This will be evaluated visually and quantitatively by calculating the LR and SNR. The optimization will be applied to IVUS and IVPA data. The method to obtain the theoretical validation of the VSSA efficacy and the optimization approach is described in Section 4.2. Section 4.3 provides the theoretical validation results. Besides, the visual and quantitative results of the optimized algorithm for IVUS and IVPA data are reported. Lastly, conclusions will be drawn in Section 4.4.

4.2. Materials and Methods

4.2.1. Theoretical Validation VSSA

The effect of the VSSA is analyzed by the principle of Delay and Sum (DAS), which essentially is the core of the VSSA algorithm. As explained in Section 3.1.1, SAFT generally improves the LR by coherently summing delayed signal values. RF lines contain positive and negative values and can be seen as waves. When a scatterer fully covers a pixel, the correct delays will result in a high amplitude for that pixel due to the summation of signal peak values that are correctly aligned by delaying. This is also referred to as constructive interference [56]. For the pixels that do not contain strong scatterers, this summation should result in pixel values that are (almost) zero due to the summation of positive and negative values. The latter is also referred to as destructive interference, which occurs when the

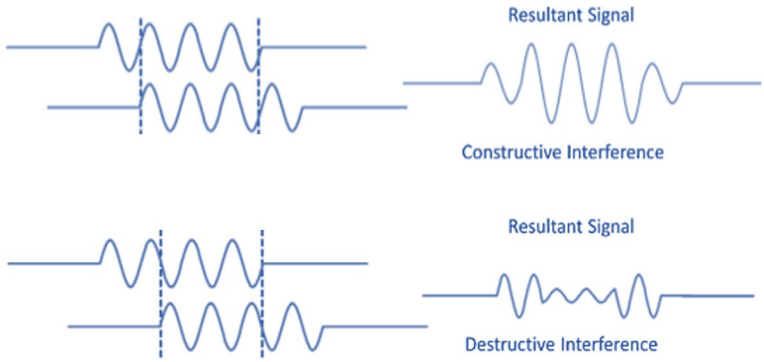

Figure 4.1: Constructive and destructive interference. Constructive interference occurs when delaying leads to alignment of the signal peaks, and summation leads to a strong resultant signal shows. In destructive interference, the signals have opposite phases, and summation will lead to a lower resultant signal than the original signals. Adapted from [56].

sum of multiple waves is lower than one of the waves by itself [57]. The principle of constructive and destructive interference is illustrated in Figure 4.1.

Due to the significant difference in signal intensity between pixels undergoing destructive or constructive interference, the SNR and the LR improve. Nevertheless, very small time delays will most likely result in a summation of in-phase signals. This means that there is barely any destructive interference because the summed values are close to each other in either positive or negative amplitude. The guideline is that the time delays of DAS methods should be larger than half a wavelength to obtain the benefits of constructive and destructive interference [56]. This time delay threshold can be calculated by Equation 4.1.

$$\Delta t < \frac{1}{2 \cdot f_c} \tag{4.1}$$

For the IVUS transducer with a center frequency of 50 MHz, DAS methods will probably not perform well when the time delays are smaller than 10 ns, which equals four samples because a sampling frequency of 400 MHz is used.

The simulated data is used to validate whether the time delays meet this guideline. The RF lines that contain signals of the same scatterer have their peak value at a different sample index because the data originates from a different transducer position causing a delay in the signal. Therefore, the locations of the signal values belonging to the same image point will show as an arc when plotting the sample index of the RF peak value over the RF index. The curvature of the arc determines how many samples the furthest RF line needs to be delayed for alignment with the reference beam. Applying the time delays will correctly align all RF, resulting in a straight line instead of an arc. The sharper the arc is, the larger the time delays that should be applied. Again, when the arc is almost flat, the time delays are so small that delaying the RF lines before summation will barely affect the image quality positively.

The second step is to evaluate the effect of DAS compared to only taking the sum of the contributing RF lines. The DAS signal is obtained by cross-correlation using the ground truth time delays determined from the simulated data. Applying these time delays will approximate a perfect alignment of the RF lines, leading to the theoretically best image quality. Once all RF lines for each scatterer are delayed, the resulting signal can be computed by taking the sum of all delayed RF lines. The DAS and only sum result are compared to the original signal, which is the reference RF line that travels straight through the scatterers.

The difference in amplitude increase is visualized by taking the envelope of the signals, which is obtained by taking the absolute of the Hilbert Transform of the original, DAS, and only sum signals. Next, the point spread function (PSF) of the three signals is visualized to evaluate their effect on the LR. The more narrow the PSF, the better the LR. The PSF is acquired by normalizing the envelope signal to its maximum value.

4.2.2. Optimization

The optimization aims to find the optimal combination of two input parameters of the VSSA algorithm that yield the best image quality in LR and maximum signal intensity (MI). The first parameter is the VS depth (z_{vs}) which strongly determines the calculated time delays. The second parameter is the half opening angle (α) of the beam, which determines the beam shape used to generate the N mask, i.e., determines how many RF signals contribute to the reconstructed pixel value. The performance is judged by quantifying the LR and MI after all steps of the VSSA algorithm are computed. The CFW is left out at this point. The reconstructed scatterer will show as a curve covering multiple pixel rows in the image, and the LR is quantified as the number of pixels that have pixel values within the 0 to -6 dB range. Instead of using the LR calculation method of 3.2.3, this 2D LR metric is used because taking the line profile through this is too cumbersome for each optimization iteration. Second, the MI is calculated instead of SNR because the MI calculation is straightforward, whereas SNR can only be calculated after manually adding noise to the data. The MI of the signal will be highest when the correct time delays are applied before the summation of the final pixel values. The LR and MI values of the original reconstruction are used as a lower limit to the optimization. Several optimization runs will be executed from coarse to fine step sizes of the input parameters to reduce the computational time. Each subsequent run will be performed over a range of VS depths and opening angles close to the input values that showed the best performance in the previous run.

The optimization will be executed for two pathways, with the VS placed in front of and behind the transducer, where the former is similar to the initial VSSA implementation described in Chapter 3. The VS depth behind the transducer needs to be larger than the physical offset of the catheter of 383 μm to allow for correct time delay calculations. This is defined because the results in Section 3.3.1 show that the time delays should become smaller when closer to the transducer, which is only the case for a concave ring. If the VS depth is smaller than the catheter offset, the distances needed to determine the time delays are calculated with respect to a convex ring of VS. In that case, the relative difference between the direct distance (r) and depth distance (r') is larger when further away from the transducer, leading to larger time delays instead. Thus, the VS depth range given as input when the VS is placed behind the transducer needs to be larger than 383 μm.

Beam Shape

When the VS is placed behind the transducer, some adjustments are needed to generate the new beam shape since this will be a diverging beam instead of an hourglass-shaped beam. However, the calculation of the beam width in the near field and far field is similar in both cases. The beam shapes are visualized in Figure 4.2. When a range of z_{vs} and α is given as input, the beam widths can be calculated by the following equation

$$w = tan(\alpha) \cdot z \tag{4.2}$$

where z equals the z_{vs} for calculating the beam width at the transducer surface. For calculating the beamwidth in the far field, z equals the imaging depth minus or plus the z_{vs} for the VS placed in front of or behind the transducer, respectively. The imaging depth is the depth seen from the transducer surface. The half opening angle (α) is calculated as follows:

$$\alpha = arctan(\frac{0.5 \cdot D}{z_{vs}}) \tag{4.3}$$

The beam width at the VS of the hourglass beam Figure 4.2a is not an infinitely small point but will be defined as half the beam width at the transducer surface.

IVPA

The theoretical validation and optimization methodology was initially developed for IVUS but reproduced for IVPA. New data was simulated similarly to the IVUS simulation. Only the frequency is adjusted to 5 MHz. The goal is to optimize the number of overlapping beams per pixel in depth to obtain the best achievable SNR and LR. Whether the data is pulse-echo or receive-only does not affect this because the beam that determines the overlap is the same in both cases. Therefore, it is assumed that the simulated pulse-echo data can be used to evaluate the VSSA performance for IVPA. A similar theoretical validation is performed as explained before, where the IVPA frequency of 5 MHz leads to a time delay guideline of 100 ns, i.e., 40 samples (See Equation 4.1). In other words, when the time delays are smaller than 40 samples, the delay and sum will likely not positively affect the image quality.

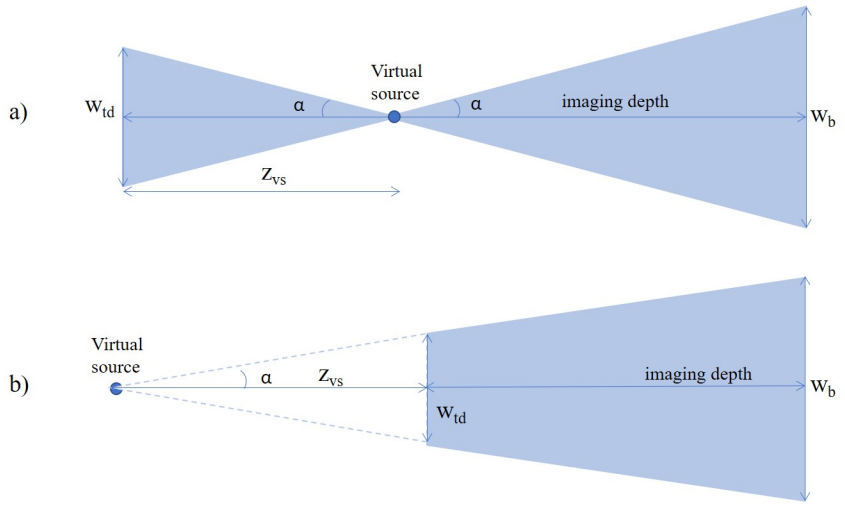

Figure 4.2: Overview of the beam shape when the VS is placed a) in front of the transducer and b) behind the transducer. α is the half opening angle, z_{vs} is the virtual source depth seen from transducer surface, w_{td} is the beam shape width at the transducer surface, and w_b the beam shape width at the imaging depth.

Next, the same optimization method is used for a range of VS depths in front of and behind the transducer and a range of half opening angles to determine the beam shape. The optimization will again be guided by quantifying the MI and LR. IVPA has a lower resolution due to the lower frequency. Therefore, the number of pixels is decreased to 501x501 instead of 2001x2001 to speed up the optimization process. Once the optimal VS depth and angle are known, the simulated data will be reconstructed to a 2001x2001 image, and LR and SNR will be quantified.

4.2.3. Image Reconstruction and Quality

The images of the simulated data, the stent data, and the artery data will be reconstructed using the optimized VSSA algorithm with the optimal combination of z_{vs} and α. Each figure is displayed with a dynamic range of 30 dB below the local maximum of the image to allow for a fair comparison between the images. The image quality will be quantified similarly as in Section 3.2.3, namely by quantifying the LR and SNR for the simulated data.

4.3. Results

The results of the theoretical validation and optimization are most extensively described for IVUS. These results are only shortly summarized for IVPA to avoid repetitiveness. More detailed results and figures can be found in Appendix B. Lastly, the reconstructed images and image quality metrics are similarly reported for IVUS and IVPA.

4.3.1. Theoretical Validation VSSA for IVUS

A plot of the sample index of the peak amplitude of each RF line was generated for each point scatterer to visualize the delay over all RF lines (See Figure 4.3). This plot shows the time delays, in number of samples, between the reference RF line and the adjacent RF lines.

The arc selected arc to evaluate for each scatterer is highlighted with the light blue box. The RF lines that do not contain any signal from that scatterer are excluded. The selected arc has a maximum time delay of five samples for scatterers 1 and 2 and six samples for scatterers 3 to 7. This is just above the threshold of four samples.

The RF lines, envelope signals, and the PSF are shown in 4.4 for the original signal, the DAS results, and the only sum result. These results are visualized for scatterers 1, 3 and 7. Scatterer 1 is located in the near field, scatterer 3 is at the natural focus, and scatterer 7 is in the far field. A strong increase in main lobe amplitude is observed when comparing the envelope of the DAS signal and only sum signal to the envelope of the reference beam. The DAS main lobe intensity is only slightly higher than the

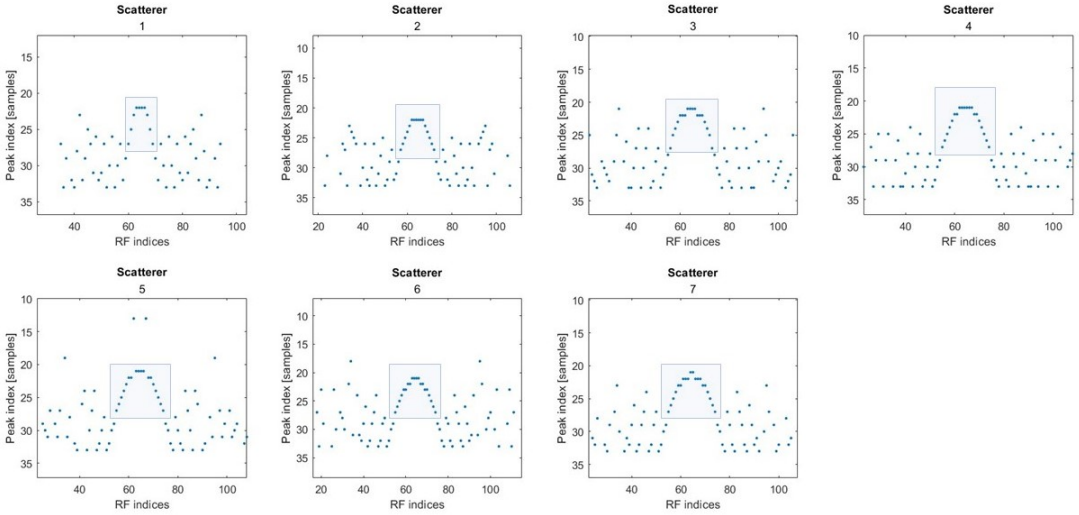

Figure 4.3: Overview of the delay range per scatterer. Generated by plotting the sample index of the peak value of the RF line. The highlighted area is the selected arc to evaluate whether the time delays are large enough for DAS methods to have a beneficial effect.

only sum result. Unfortunately, the side lobe intensity is also increased. Overall, neither DAS nor only summation improves the LR, because the width of the PSF remains the same compared to the original signal.

This means that the main gain of the VSSA method lies in improving the SNR by increasing the intensity of the image signal. This can be used to guide the optimization. In conclusion, the desired outcome after optimization is an increased MI and LR that is equal to or better than the LR of the original signal.

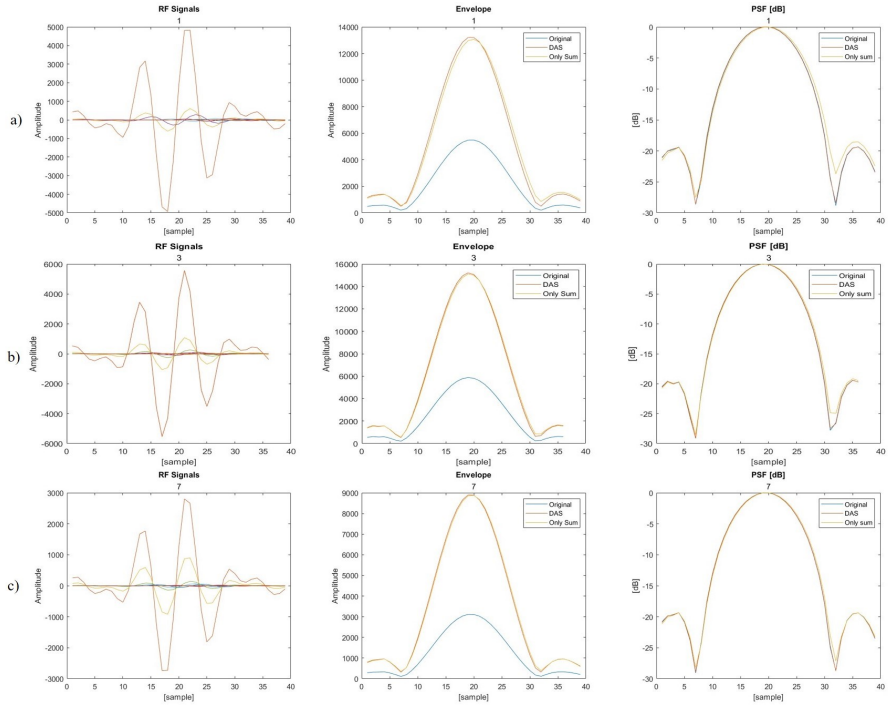

Figure 4.4: From left to right for each image: The RF lines of the scatterer, the envelopes of the original, DAS and only sum results, and the PSF of the original, DAS and only sum signals. a) shows the results for scatterer 1 at 0.5 mm depth in the near field, b) for scatterer 3 at the natural focus at 1.6 mm depth, and c) for scatterer 7 at 5 mm in the far field. The DAS and only sum results show similar behavior for the envelope signal and the PSF. The PSF is very similar for all three signals. However, the maximum intensity is strongly increased by DAS and only sum, compared to the original signal.

4.3.2. IVUS Optimization

The MI and LR values of the original image are used as the lower limit to guide the optimization. These values can be found in Table 4.1 together with the LR and MI values for the VSSA method with the VS at the natural focus of Chapter 3, further referred to as the initial VSSA implementation.

Table 4.1: IVUS quantification of the image quality for the original reconstruction, the initial VSSA implementation from Chapter 3, and the optimization results of the VS behind the transducer. Per scatterer, the maximum intensity (MI) is reported in dB, and the lateral resolution (LR) in a number of pixels within the 0 to -6 dB range. The LR values are calculated from 2001x2001 images.

Non-Optimized								
	Scatterer	**1**	**2**	**3**	**4**	**5**	**6**	**7**
Original *RF stacking*	Lateral Resolution [#pixels]	10	22	40	60	85	125	157
	Maximum Intensity [dB]	74.6	80.3	75.2	72.7	71.4	70.4	69.6
VSSA $z_f = 1.6mm$	Lateral Resolution [#pixels]	120	92	20	81	134	177	210
	Maximum Intensity [dB]	77.9	78.4	79.3	79.4	75.5	86.5	81.3
Optimized								
	Scatterer	**1**	**2**	**3**	**4**	**5**	**6**	**7**
Behind $z_{vs} = 0.4mm$ α = 1.5 °	Lateral Resolution [#pixels]	17	20	37	75	112	104	127
	Maximum Intensity [dB]	80.5	86.7	82.1	79.8	78.3	77.8	77.2

VS in front of the Transducer

It was observed that the smallest angles and VS depths obtained the best LR that was comparable to the original, whereas the MI was lowest for the smallest angles. However, these small angles that yield LR values that are similar to or lower than the original LR have an insufficient overlap at the VS depth. Insufficient overlap leads to pixels without available data for reconstruction. Therefore, no angle and VS depth in front of the transducer shows improvement of the MI when the LR is equal to or better than the original image.

VS behind the Transducer

The optimization results are visualized in Figure 4.5 to show the observed trends that count for LR and MI in the near field, at the focus, and in the far field. Green indicates the best values, which is a low value for LR and a high value for MI. It was observed that the LR is best for the smallest VS depths and angles, whereas the MI is highest for small VS depths and larger angles. However, even the lowest MI values obtained from the optimization are higher than the MI of the original reconstruction for all scatterers. Therefore, it was chosen to aim for the largest possible gain of MI increase for a LR that is equal to or better than the original reconstruction. The LR resolution should be equal to or lower than 10, 40, and 157 pixels for the near field, focus, and far field, respectively. A VS depth of 0.4 mm and an angle of 1.5 degrees was the optimal combination yielding a similar or better LR and higher MI. The corresponding LR and MI values can be found in Table 4.1 together with the original reconstruction and the non-optimized initial VSSA LR and MI results. Not all LR values are lower than the original LR values of the individual scatterers, but the optimization shows an average reduction of 7 pixels. The MI is improved for all scatterers compared to the original reconstruction. The MI is, on average, increased by 6.9 dB, with 6.15 dB in the near field, 6.9 dB at the focus, and 7.25 dB in the far field.

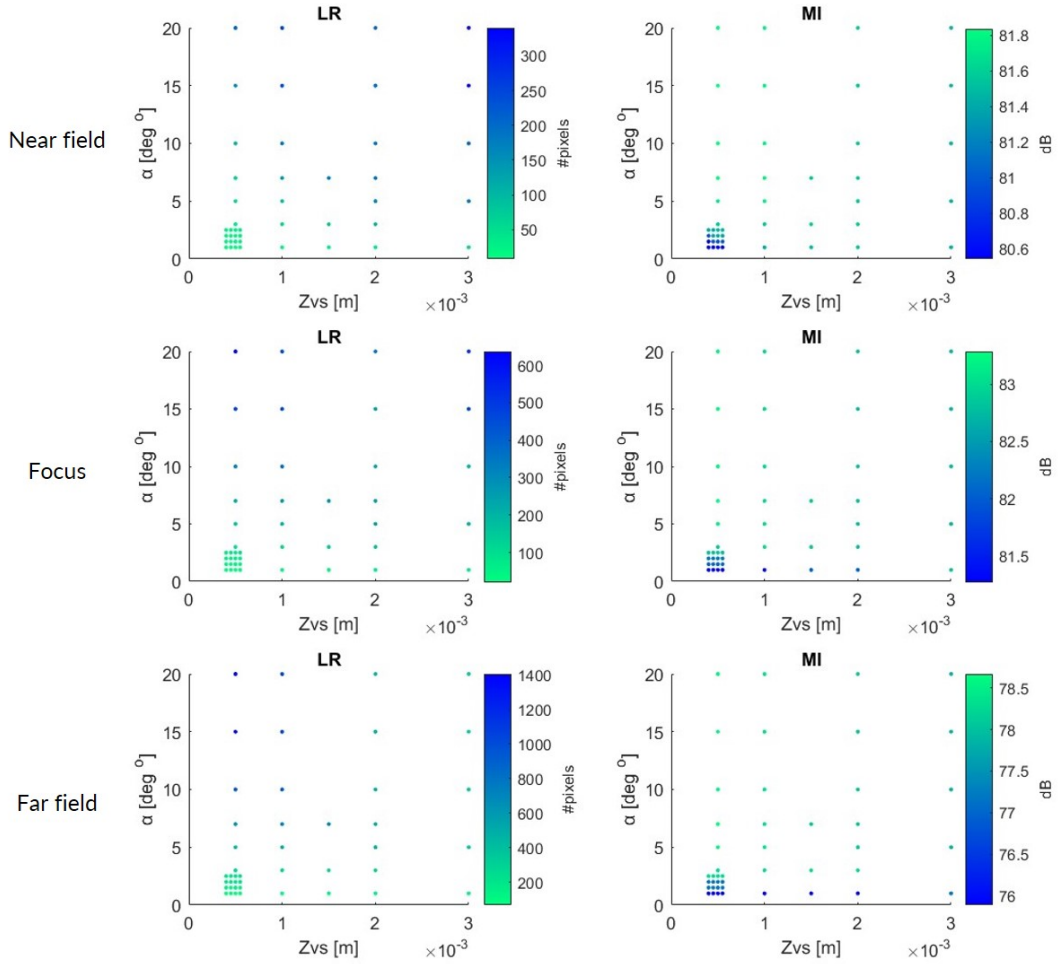

Figure 4.5: The optimization results for LR and MI plotted over the input ranges of half opening angle of the beam (α) and the VS depth behind the transducer (z_{vs}). The results are visualized for scatterer 1 in the near field, scatterer 3 at the natural focus, and scatterer 7 in the far field. The unit of the color bar for LR is the number of pixels that fall within the 0 to -6 dB range, and MI is given in dB.

4.3.3. IVPA

The theoretical validation of the IVPA data shows that DAS performs similarly to only sum and the original result regarding LR. The theoretical validation results for IVPA can be found in Appendix B.1. The guideline was set on time delays of 40 samples for the DAS to positively affect the IVPA image quality. When evaluating the curvature over the figures where the sample indices of the peak amplitudes per RF lines are plotted, it was found that the time delays are only slightly bigger than 40 samples. This could explain why DAS does not show improved MI and LR compared to the only sum result. Again, the MI is increased for DAS and only sum compared to the original signal. Hence, the optimization aims to find the VS depth and angle that have similar or improved LR to the original signal with the largest possible gain in MI.

When the VS is placed in front of the transducer, improved LR and MI values are obtained compared to the original reconstruction. However, the LR and MI are even more improved when the VS is placed behind the transducer. Hence, only the results for optimizing the VS behind the transducer will be discussed. The first run was executed with angles up to 50 degrees and VS depths up to 3 mm. It was observed that the LR was best for very small angles and VS depths, whereas the highest MI was overall found for large angles at similarly small VS depths. The LR quickly deteriorates when the angle is increased. The optimal angle and VS depth combination is where the LR is maintained or improved, with the largest possible gain in MI. This is achieved when the VS was placed at 0.7 mm behind the transducer with a half opening angle of 2 degrees. This results in a LR that is equal to the original reconstruction for scatterer 1, and much lower for the other scatterers. A visual representation of the optimization runs and the selected optimal values can be found in Appendix B.2. The further away the scatterer is from the transducer, the larger the LR improvement. The MI decreases with depth but is, on average, increased by 12.5 dB compared to the original reconstruction.

4.3.4. Image Reconstruction and Quality

IVUS

The best combination of LR and MI values was found for IVUS when the VS was placed at 0.4 mm behind the transducer, with a half opening angle of 1.5 degrees. These parameters are used to reconstruct the images with the optimized version of the VSSA algorithm for the simulated data (Fig 4.6, the stent data (Fig. 4.7), the artery data (Fig. 4.8), and the simulated data with added noise (Fig. 4.9). The optimized VSSA images are visualized with the original reconstruction and the initial VSSA implementation. Overall, the images reconstructed by the optimized VSSA show better image quality in LR and SNR than the initial VSSA implementation. Especially in the noisy simulated data results in Figure 4.9 is visible that the optimized VSSA performs much better regarding SNR compared to the initial VSSA algorithm. Besides the simulated data with noise, the image quality decrease by the initial VSSA implementation is most clearly visible in the artery data of Figure 4.8. The image appears more blurry with less contrast. This contrast is regained and even improved by the optimized VSSA algorithm, which stands out most clearly in the distinction of the different vessel layers. For instance, this is visible in the optimized VSSA image from 1 to 7 o'clock, where the space between two layers is darker than in the original reconstruction. The LR can be compared visually best in the stent and simulated data, which shows a LR that seems comparable to the original reconstruction.

The image quality of the simulated data is quantified for LR and SNR, which are summarized in Table 4.2. The optimized LR is worse than the original reconstruction for all scatterers. However, the SNR is improved by the optimized VSSA algorithm for all scatterers. The SNR is, on average, increased by 0.7 dB.

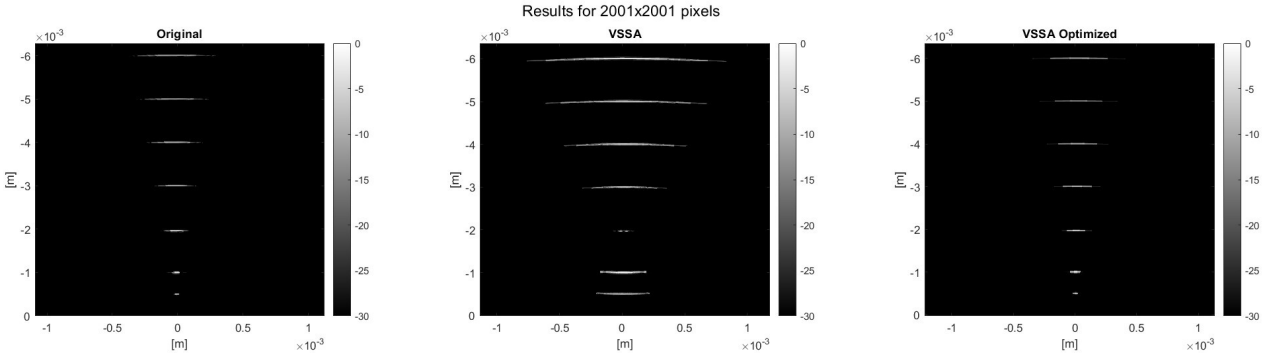

Figure 4.6: Simulated IVUS data results. From left to right: The reconstructed images by the original reconstruction, the initial VSSA algorithm with the VS at the natural focus, and the optimized VSSA algorithm for the simulated data. All images are displayed in dB with a 30 dB dynamic range below the local maximum of the image.

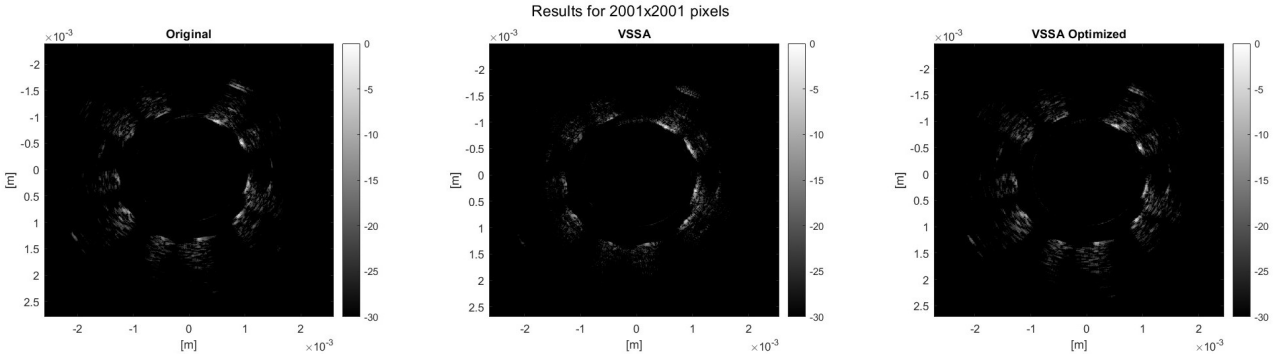

Figure 4.7: Stent data results. From left to right: The reconstructed images by the original reconstruction, the initial VSSA algorithm with the VS at the natural focus, and the optimized VSSA algorithm for the simulated data. All images are displayed in dB with a 30 dB dynamic range below the local maximum of the image.

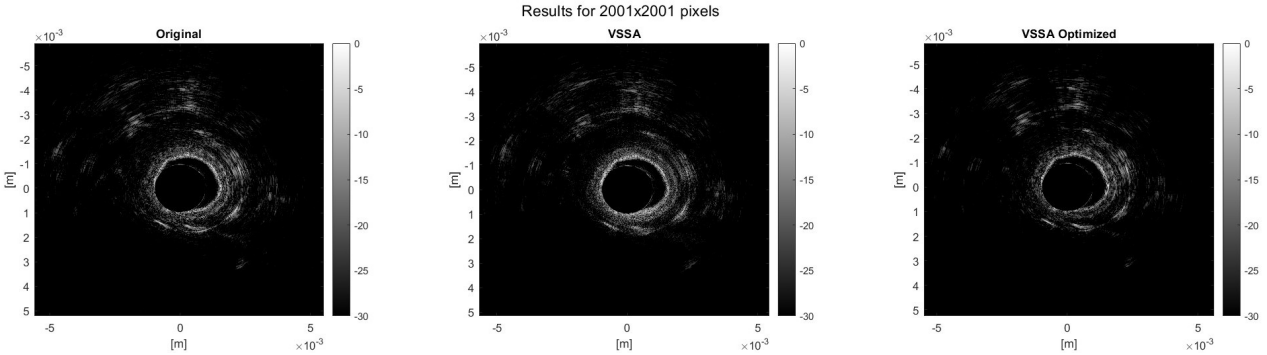

Figure 4.8: Artery data results. From left to right: The reconstructed images by the original reconstruction, the initial VSSA algorithm with the VS at the natural focus, and the optimized VSSA algorithm for the simulated data. All images are displayed in dB with a 30 dB dynamic range below the local maximum of the image.

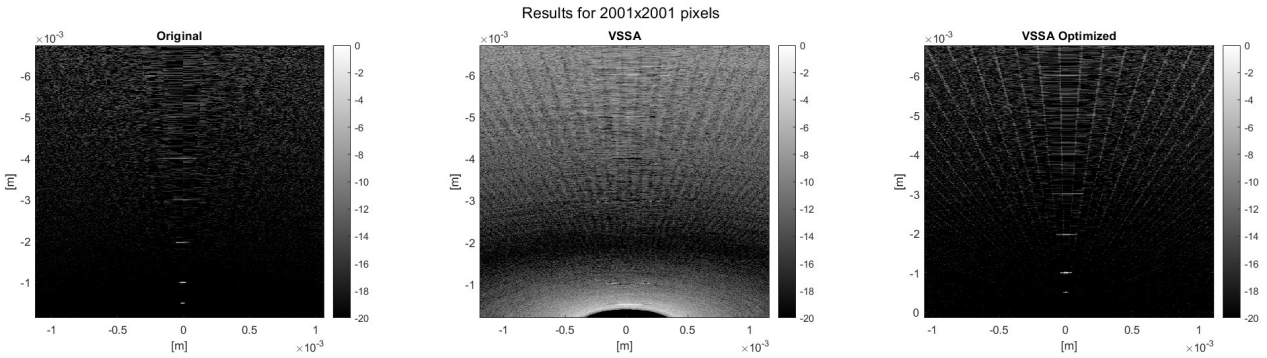

Figure 4.9: Simulated data with noise. From left to right: The reconstructed images by the original reconstruction, the initial VSSA algorithm with the VS at the natural focus, and the optimized VSSA algorithm for the simulated data. All images are displayed in dB with a 20 dB dynamic range below the local maximum of the image.

Table 4.2: IVUS image quality results. Lateral resolution (LR) and Signal-to-Noise Ratio (SNR) values for the original reconstruction and the optimized VSSA result of the simulated IVUS data. The SNR is quantified for the simulated data after noise addition with a comparable noise level to the experimental data.

Scatterer	1	2	3	4	5	6	7
Lateral Resolution Original [μm]	29.0	43.6	94.4	159.7	246.8	290.3	362.9
Lateral Resolution Optimized VSSA [μm]	36.3	50.8	145.2	225.0	297.6	370.2	442.8
SNR [dB] Original	7.3	11.9	6.8	4.5	4.5	3.1	3.2
SNR [dB] Optimized VSSA	7.4	12.2	7.8	5.8	5.3	4.0	4.8

IVPA

The VSSA algorithm reconstructed the image of the simulated IVPA data with the VS at 0.7 mm behind the transducer and a half opening angle of 2 degrees. The results of the original reconstruction, the VSSA, and the optimized VSSA are visualized in Figure 4.10. The LR seems improved by the optimized VSSA compared to the initial VSSA and original reconstruction. The scatterers in the far field are less visible in the optimized reconstruction, whereas their amplitude is higher than in the original reconstruction. This distorted view is caused by the high amplitude of the first scatterer that determines the dynamic range.

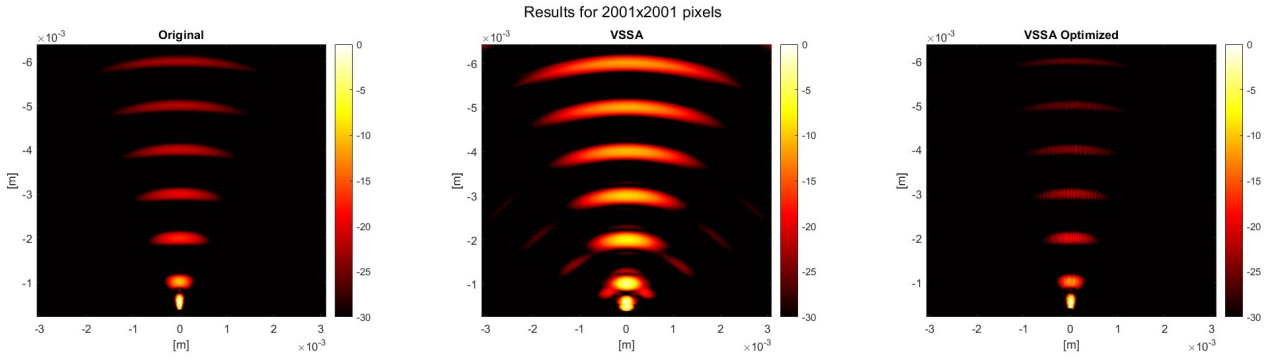

Figure 4.10: Simulated IVPA data results. From left to right: The reconstructed images by original reconstruction, the initial VSSA algorithm with the VS at the natural focus, and the optimized VSSA algorithm for the simulated data. All images are displayed in dB with a 30 dB dynamic range below the local maximum of the image.

The image quality of this optimized VSSA result is quantified and compared to the image quality values of the original reconstruction. The values can be found in Table 4.3. The optimized VSSA improves the LR for all scatterers except for the first and last. The SNR is improved in all cases except for scatterer 7. On average, the SNR is 1.1 dB higher for the VSSA result compared to the original reconstruction.

Table 4.3: IVPA image quality results. Lateral resolution (LR) and Signal-to-Noise Ratio (SNR) values for the original reconstruction and the optimized VSSA result of the simulated IVPA data. The SNR is quantified for the simulated data after noise addition with a comparable noise level to the experimental data.

Scatterer	1	2	3	4	5	6	7
Lateral Resolution Original [mm]	0.094	0.37	1.0	1.5	1.8	2.3	2.6
Lateral Resolution Optimized VSSA [mm]	0.10	0.36	0.84	1.3	1.6	2.0	2.6
SNR [dB] Original	19.2	9.3	1.5	2.5	0.5	2.3	2.4
SNR [dB] Optimized VSSA	21.0	10.7	2.8	3.1	2.3	3.4	1.4

4.4. Discussion

The optimization leads to improved image quality when the VS is placed behind the transducer instead of at the natural focus. The methodology to reach this is discussed below, together with a discussion of the results of the theoretical validation, the optimization, and the final image reconstruction and image quality.

4.4.1. Theoretical Validation VSSA

The simulated IVUS data shows that there is only a small delay of five or six samples over the entire arc between the reference beam and the beams that are furthest from the imaging point. Whenever the number of overlapping RF lines based on the N mask is not the maximal amount of RF lines that contains the signal, fewer RF lines and thus smaller delays are used to reconstruct a pixel. This delay will quickly be below the threshold of four samples for DAS to have an effect. Similar results were observed for the IVPA data. Therefore, the biggest gain in image quality will likely be an SNR improvement after the summation of the non-delayed signals for IVUS and IVPA data.

Furthermore, the IVUS data barely show a difference between the DAS and only sum results in envelope and PSF. This can be caused by the following: For each scatterer, we see in Figure 4.3 that multiple RF lines do not have to be delayed to align with the reference beam. These are also the RF lines closest to the point scatterer and therefore have the highest signal amplitude, which will be summed regardless of applying a delay since there is none. The first RF line subject to delay has a much lower amplitude that only accounts for a small percentage of the sum of the first non-delayed signals. Similar results are observed for the IVPA data because the first six to eight RF lines are not subject to delays, or the delay is so small that the added amplitude value will be very similar to the non-delayed value. In conclusion, the RF lines that should be delayed have a significantly smaller amplitude than the non-delayed signals, so their contribution to the sum, and thus the effect of delay and sum, will be negligible. Therefore, the DAS result was observed to perform equally to the only sum result.

4.4.2. Optimization

When the VS was placed behind the transducer, it was generally observed for IVUS and IVPA that the MI was largest for large angles. Large angles generate a beam shape with a larger surface area, causing a higher overlap. Thus, this leads to a summation of more values resulting in a higher MI. Meanwhile, the LR was best when small angles and small VS depths were used. This could be because the summation is most effective when only a limited amount of RF lines is used because the signal amplitude strongly drops when the RF line is only slightly further away. Nevertheless, for a small angle of 1.5 degrees and a VS depth 0.4 mm behind the transducer, there was still an increased MI found for IVUS, while the LR was similar to or slightly better than the LR of the original image. The IVPA optimization showed that an angle of 2 degrees and the VS at 0.7 mm behind the transducer gives an equal or better LR with a substantial MI increase. Both cases have a quite narrow beam shape due to the small opening angle, leading to few overlapping RF lines per pixel (N). The maximum overlap is an overlap of three

and six RF lines for IVUS and IVPA, respectively. Besides, the VS depth is very close to the axis of the catheter, such that the VS are located on a small circle. Together, this leads to such small time delays in seconds that all delays are rounded to 0 samples, i.e., no delays. Again, a non-delayed VSSA yielding optimal image quality can be validated by what has been observed in the theoretical validation where the only sum result shows nearly equal performance to the DAS result.

4.4.3. Image Reconstruction and Quality

The optimized VSSA visually shows a great improvement in image quality compared to the initial VSSA algorithm with the VS at the natural focus for IVUS and IVPA. The aim is to find an improvement in image quality compared to the original reconstruction. The image quality results show an increase in SNR and LR except for the LR of the IVUS. The SNR of the optimized VSSA for IVUS is, on average, increased by 0.8 dB compared to the original reconstruction. The average SNR increase is 1 dB for IVPA. The LR is only improved for IVPA, which is equal or slightly better for each scatterer reconstructed by the optimized VSSA.

Placing the VS behind the transducer leads to a diverging beam instead of the proposed hourglass beam shape of the initial implementation based on [29]. The optimized VS depth and half opening angle of the beam shape cause little overlap of the beams, resulting in an optimal image reconstruction without delaying the RF lines before summation.

5

General Discussion

5.1. Conclusion

This report will be concluded by evaluating whether the research objective is met based on the achieved results. The main research objective was as follows:

Main Research Objective

To develop an IVUS and IVPA image reconstruction method with improved image quality to advance lipid imaging in atherosclerotic coronary arteries.

This improved image quality is defined as the improvement of LR and SNR compared to the conventional image reconstruction method of stacking RF lines, referred to as the original reconstruction. The image reconstruction method that is developed for this purpose is a pixel-based VSSA method that computes image pixel values by delaying and summing the RF lines of beams that overlap that particular pixel. The VSSA algorithm was optimized to the IVUS and IVPA characteristics of the Kaminari Medical catheter by finding the optimal VS depth and half opening angle of the beam. A VS depth of 0.4 mm behind the transducer and a half opening angle of 1.5 degrees led to best image quality for IVUS data captured with a 50 MHz center frequency transducer. For IVPA, this was a VS depth of 0.7 mm behind the transducer and a slightly larger angle of 2 degrees. The IVPA center frequency is 5 MHz, meaning that the lower the frequency, the further the VS should be placed behind the transducer and the larger the opening angle of the beam. Thus, a broader beam shape is used for lower-frequency data. The LR and SNR are quantified for the IVUS and IVPA data to evaluate whether the optimized VSSA improves the image quality with respect to the original reconstruction.

The lateral resolution can be characterized by Equation 3.1, which describes the resolution in the focal zone for focused transducers or in the area beyond the transition to the far field for unfocused transducers [47]. The LR for the 50 MHz IVUS transducer is 108 μm. The calculated LR for the IVUS data is around 100 μm for the scatterers at and around the natural focus in Section 4.3. Even though the simulated beam profile showed a weakly focused beam, the measured LR in the focal zone seems to correspond with the theoretically calculated LR for this transducer. However, the optimized VSSA algorithm shows a LR that is slightly deteriorated for IVUS, whereas the expectation was that synthesizing a larger aperture would improve the LR. The optimized VSSA uses a maximum of three non-delayed RF lines to reconstruct the pixels for the IVUS data, which means that the synthetic aperture is only increased slightly for some pixels. The results show that the optimized VSSA LR is, on average, 48 μm higher than the LR of the original reconstruction, which accounts for a 29.5% decrease. On the other hand, the LR is improved for IVPA by 7% on average, which accounts for an average reduction of 126 μm compared to the original reconstruction. It would be expected that the VSSA effect on IVPA data is smaller because the time delays need to be much larger, due to the lower frequency than IVUS, to benefit the image quality. Nevertheless, the optimized VSSA for the IVPA data shows a maximum overlap of six instead of three RF lines for IVUS, which synthesized a larger aperture because the same

rotational radius is used. Since a larger synthetic aperture leads to an improved LR, the maximum overlap of three RF lines for IVUS could be insufficient to benefit from the LR increase by a larger aperture, whereas an overlap of six leads to an LR improvement for IVPA.

In contrast with the LR, the SNR is improved for IVUS and IVPA. The SNR shows an increase of 20.3% for IVUS and 77.7% for IVPA with respect to the original image reconstruction. For the IVUS data, the SNR increases even more with depth.

It can be concluded that optimized VSSA only improves the LR for the IVPA data, whereas the SNR is substantially improved for both IVUS and IVPA. This means that the research objective is partially met, and future work should be aimed at further improving the lateral resolution to show an improvement of LR and SNR for all transducer characteristics. The high quality images that are generated by the optimized VSSA will benefit atherosclerotic lipid images in multiple ways. First, a higher image quality enables more accurate image feature quantification like measurement of the lipid pool size, or it could even enable fibrous cap thickness measurements. Second, a higher SNR increases the image depth and allows for visualization of tissue structures or lipids at larger depths. This could provide a more complete image of the artery. For example, this enables detection of deeper located lipids or arterial side branches that could affect the strategy for stent implantation. Lastly, a good LR also benefits the visualization of stents during or after implantation, because the stent struts strongly reflect the ultrasound and easily create side lobes that could deteriorate the visibility of lumen and stent borders [36]. The increase of LR reduces the side lobes and improves assessment of the stent implantation due to the enhances stent visualization with respect to the arterial wall and the lipids.

A reason for lower LR for IVUS could be that the VS depth and half opening angle should be optimized better. The selection of the optimal parameter combination is done manually, due to the trade-off between LR and MI. The theoretical validation showed that this algorithm will benefit the SNR most, so a LR close to the lower limit with the largest gain in MI was chosen. However, a different angle and VS depth could still result in a LR and MI above the lower limits. For example, another parameter combination could result in an improved LR but a slightly lower MI. An analytical approach to the optimization would be a good way to avoid this parameter selection being affected by human decisions. An analytical formula should be derived to determine the VS depth and the beam angle when the frequency changes. For this, a dependency between the center frequency of the transducer and the beamwidth or VS can be defined. One example of an analytical formulation that shows a certain dependency between the frequency (f_c), transducer width (D), which equals the beam width at the transducer surface, and the VS depth (z_{vs}) is Equation 5.1, which is similar to equation 3.5

$$z_{vs} = \frac{D^2}{4 \cdot \frac{c}{f_c}} \tag{5.1}$$

An attempt to derive an analytical approach was made with Equation 5.1 as the basis. However, the D and z_{vs} are the two variables that needed to be optimized because the beam shape is not limited to transducer width, so D could also vary. Therefore, the dependency between z_{vs} and D should be merged into this formula to only have one of these two parameters as the unknown variable. Still, additional factors are needed to find a solution for the IVUS and IVPA cases. It is recommended to first run the manual optimization for multiple frequencies to find relations between the variables more accurately to use this in the derivation of an analytical approach.

Second, the lack of LR improvement for the IVUS data could be due to the catheter geometry. The distance between the transducer and the rotation axis is minimal (383 μm), leading to a short distance between transducer positions during rotation. The time delays will be smaller when the different rotational transducer positions are closer to each other because the distances between the pixel and various VS will be smaller. The short distances between the VS could limit the size of the time delays such that this will not be larger than half of the wavelength. As discussed previously, DAS methods will only benefit the image quality when the time delays are larger than half the wavelength.

Moreover, the IVUS data showed that the difference in SNR between the original and optimized reconstruction increases with depth, which indicates that the algorithm works better in the far field (> scatterer 3). The IVPA transducer has a ten times lower frequency than the IVUS transducer, leading to a natural focus much closer to the transducer. The IVPA natural focus lies at only 0.16 mm at which scatterer 1 is located. All other scatterers are therefore placed in the far field, which might cause larger

image quality improvements for the IVPA data compared to the IVUS data. When more scenarios with different transducer frequencies are tested, a threshold up to which depth it is best to stick to the original reconstruction and to apply the VSSA to depths larger than that threshold can be derived. From the results can be derived that the largest benefit of the VSSA method lies in reconstructing scatterers in the far field. Thus, this threshold should depend on the natural focus.

5.2. Weighting Method

Since it was theoretically proven that the efficacy of the VSSA is limited regarding LR improvement, other methods could be attempted to achieve this LR improvement to meet the research objective fully. A Coherence Factor Weighting (CFW) method was developed and implemented as discussed in Chapter 3 to further improve the LR by reducing the sidelobes. Compared to the original reconstruction, the CFW did improve the LR of some far field scatterers in the simulated IVUS data. This effect was also observed visually for the stent data. However, it showed inferior image quality for the artery data, and the CFW decreased the SNR for the simulated data. Similar behavior is observed when the CFW is applied to the optimized VSSA. It seems to work well on the simulated and stent data but degrades the artery data's image quality. However, image quality improvement is most important for the latter scenario to enable introduction to the clinic. The assumption is that once the time delays are calculated correctly, which is enabled by an accurate location of the VS, the CFW should provide improved LR to all data types. However, the CFW shows chaotic values with no clear signal pattern as expected. This could be due to the CFW calculation method, which is the ratio between the envelope of the sum of the delayed RF values and N times the sum of envelopes of the delayed RF values. A high CFW means high coherency between the RF values. Since the coherency is based on the envelope, a high coherency is relatively easily reached even for noise pixels. Besides, the CFW might not work well because it is developed for a focused transducer. In contrast, Chapter 3 shows that the IVUS beam is only weakly focused, and the best results are obtained by simulating a diverging beam generated from a VS behind the transducer.

Therefore, it was aimed to find weighting methods in the literature that are developed explicitly for diverging beam SAFT. A Sign Coherence Factor (SCF) was described, which shows good side lobe reduction performance and LR improvement for diverging beam SAFT [58]. The SCF is based on the I/Q RF data and calculates the weight based on the sign of the phase value as follows [58]:

$$SCF = \left[1 - \sqrt{1 - (\frac{1}{N}\sum_{n=1}^{N} b_m(k))^2}\right]^p \tag{5.2}$$

where $b_m(k)$ is -1 when the sign of the phase signal < 0 and 1 when the phase signal is > 0. This is determined by taking the signum of the imaginary part of the RF value. The SCF is calculated per pixel, so N is the number of RF lines that overlap each pixel. This means the more RF phase values have the same sign, the higher the SCF value with a maximum of 1. This could be an alternative weighting method to add to the algorithm, so it was implemented and tested on the simulated IVUS data to provide preliminary results on its image quality performance. These results show an improved LR for one scatterer, a similar LR for scatterer 4, and a slightly worse LR for the rest compared to the original. Overall, this is a reduction of LR by 12.6%. Adding the SCF does improve the LR slightly compared to the optimized VSSA only but does not meet the desired improvement of LR compared to the original result. However, the SNR is strongly improved. Instead of an average increase of 20.3% by the VSSA only, the SNR is increased by 75.8% after the addition of the SCF. In conclusion, adding the SCF could yield better image quality than the optimized VSSA only, yet it does not meet all desired image quality requirements. The optimized VSSA for IVUS does only sum two or three RF lines without applying any delays. Therefore, this is not a beamforming method as SAFT are. This could also preclude the effect of the SCF since the SCF is developed to be applied on delayed RF.

Another idea is to weigh the RF lines according to their beam profile intensity at the point where it overlaps the pixel. The center axis of the US beam profile has the highest intensity, which decreases laterally, as visible in Figure 3.6. The RF value used to reconstruct the pixel value can be weighted according to the intensity of the beam profile of the RF line that overlaps the pixel. When the pixel. The assumption is that the closer the RF line is to the pixel, the higher the beam profile intensity and

the higher the weight that should be applied. On the other hand, when the RF line is further away from the pixel, it should have a lower weight and, thus, a lower contribution to the reconstructed pixel. This was implemented with weight values between 0 and 1 that sum up to 1 to take normalization into account. The distance between the pixel and VS (r') is used to determine which RF line is closest.

Again, some preliminary results are reported based on arbitrary values of 0.8, 0.1, and 0.1 or 0.9 and 0.1 as weights for 3 or 2 overlapping RF, respectively. This method does successfully improve the original IVUS LR by 5.9%. Nevertheless, the SNR is decreased to values below the SNR of the original reconstruction for most scatterers. However, this technique is certainly promising due to the LR improvement, and future work is recommended to find the optimal weights. In this case, the arbitrarily selected weights could be the reason for the SNR decrease because the furthest RF line gets a low weight regardless of its actual distance to the pixel. It would be better to scale the weights to the distance the RF lines have from the pixel instead of giving a fixed weight based on the order of proximity. For instance, when the pixel is almost exactly in the middle of two RF lines, and one is only slightly further away than the other, they should both get a weight of around 0.5 instead of 0.9 and 0.1.

In conclusion, the optimal weighting method still needs to be established, which improves the LR without degrading the SNR achieved by VSSA. As explained above, the beam profile weighting method is a promising candidate. Otherwise, the optimization could be tailored to give a low LR and SNR, which can subsequently benefit from the SNR increase by the SCF. However, it needs to be taken into account that a good performance on simulated data does not necessarily mean a good performance on experimental artery data.

5.3. Algorithm Implementation

5.3.1. Beam Shape Overlap

The number of RF lines that need to be reconstructed is based on the overlap of the beam shapes. In the initial implementation, this beam shape was simplified to an hourglass shape with its smallest width equal to half of the transducer width. This simplified beam assumes that all energy is limited to be only present and equally distributed within the boundaries with a fixed energy level. The concept of the VSSA is likely based on this due to its simplicity. However, in the real scenario, we are dealing with wave physics where the beam is a beam profile with different energy levels laterally and per depth. This difference does not affect the time delay calculation method because this is calculated per pixel based on the distances to the VS, which remains the same. However, simplifying the beam shape could preclude the selection of the right RF lines for the reconstruction of the pixels. For example, a more accurate method is to use a beam shape based on the contour of the -6 dB contribution of the beam profile and additionally weigh the RF line before summation based on its beam amplitude at that particular pixel. This approach could be interesting for future work because selecting the RF lines more accurately and weighing them to their beam profile intensity ensures that all available information on the overlapping beams is considered.

Besides, there is a minimum line density, i.e., number of acquired RF lines, because the algorithm breaks down when there are pixels that are not overlapped by any RF line. The minimum number of RF lines strongly depends on the beam shape, its opening angle, and whether the VS is placed in front of or behind the transducer. The optimized VSSA performs best when placing the VS behind the transducer, leading to a diverging beam shape. The overlap of diverging beams decreases with the imaging depth due to the larger radius at larger imaging depths. Therefore, it can be stated that there are sufficient RF lines when the ratio between the circumference at the desired maximal imaging depth and the number of lines times the arc length of a beam at this imaging depth is larger than 1. When this ratio falls below 1, the total arc length of all beams is smaller than the circumference of the circle, meaning there are gaps with no overlap.

$$\frac{2 \cdot \pi \cdot r}{(r \cdot \alpha_{rad}) \cdot N_{RF}} > 1 \tag{5.3}$$

Where $r \cdot \alpha_{rad}$ is the arc length of the beam at imaging depth r for the full opening angle of the beam (α) in radians. Since the r is equal in the numerator and denominator, the minimum number of RF lines

N_{RF} can be calculated as follows

$$N_{RF} > \frac{2 \cdot \pi}{\alpha_{rad}} \tag{5.4}$$

For the IVUS data, the number of RF lines needs to be >120, whereas only >90 are needed for IVPA due to its larger full opening angle of 4 degrees. The data in this research was acquired with 256 RF lines per rotation, which is sufficient.

Lastly, the algorithm deals with a stripe artifact based on the N mask, which is most clearly visible in Figure 4.9. The overlap of the beam will always create a certain pattern due to pixels having more overlapping RF lines than others. This pattern is again visible in the final image because the pixels with a higher overlap will likely get a higher signal amplitude and show brighter pixels in the image. The stripe artifact is more strongly present when there is little overlap because the difference in pixel values is relatively larger. A way to reduce this stripe pattern is to normalize all pixel values for N by multiplying the final pixel values with 1/N. A disadvantage of this method is that it decreases the signal amplitude.

5.3.2. Pixel-based Discretization

The VSSA is originally a beamforming algorithm that synthesizes new RF lines by delaying the original RF data [29]. Subsequently, the image is reconstructed based on the original and synthesized RF lines. However, it was decided to develop a pixel-based implementation. The pixel-based implementation is based on the same principle. The difference is that the image pixel values are directly reconstructed versus the pixel values being reconstructed after stacking the original and newly synthesized RF lines. The pixel-based implementation was chosen because of its computational efficiency and because synthesizing new RF lines is more complicated for rotational scanning compared to the rather straightforward calculations in a linear scanning method. This is mainly due to the complexity of calculating the correct time delays to apply to the original RF lines to synthesize a new RF line. The delay that should be applied changes with the depth along the RF lines that will be synthesized because the adjacent RF lines are received under an angle. The larger the imaging depth, the further away the original RF line is from the synthesized RF line, thus the larger the time delay that should be applied. Moreover, also the number of RF lines used to synthesize a new RF line changes per depth. Determining the depths where the N changes is quite a complex trigonometry problem due to the rotational scanning method that occurs under an angle. However, this method does not suffer from discretization errors like the pixel-based implementation, so it could be worth the effort of implementation.

Discretization is the conversion of continuous data to a discrete form. This involves having a value per pixel rather than continuous values for infinite measurement points. The image resolution will be lower when fewer pixels are used for this discretization. Moreover, a sufficient number of pixels must be reconstructed to avoid undersampling the signal. The Nyquist-Shannon Sampling Theorem can be used as a guideline to find the minimum number of pixels that gives a sufficient sampling rate for the discretization to reproduce the signal accurately [59]. When fewer pixels are used, the signal is undersampled, which leads to a distorted image due to aliasing artifacts. Aliasing artifacts occur because the frequency spectrum cannot be replicated in its original spectrum, which causes overlap of frequency components [60]. Following Nyquist, the data should be sampled at least twice per wavelength [59], i.e., the number of samples per pixel should be half the number of samples per wavelength. The data was acquired with a sampling frequency of 400 MHz, i.e., 400e6 samples per second. The frequency of 50 MHz of the IVUS transducer yields a sampling density of eight samples per wavelength. This means that the minimum pixel density is four samples per pixel to sample with twice the amount of pixels per wavelength. The experimental artery data has 3784 samples for 7 mm imaging depth from the transducer surface. Thus, a pixel density of 1892x1892 is the minimum for the IVUS data when the RF lines start in the center of the image. Compensating for the catheter offset and considering that there are fewer pixels along the diagonals due to larger inter-pixel distance, a pixel density of 2001x2001 was used to compensate for this. The IVPA images need a much lower amount of pixels due to the lower resolution. Because the IVPA data is sampled with 80 samples per wavelength, and the data only contains the received US waves because the light excitation is instantaneous, it has half of the samples compared to IVUS. This leads to a minimum pixel density of only 93x93 for imaging up to 7 mm. Therefore, reconstructing the IVPA images with more than 200x200 should be sufficient to avoid undersampling artifacts in IVPA.

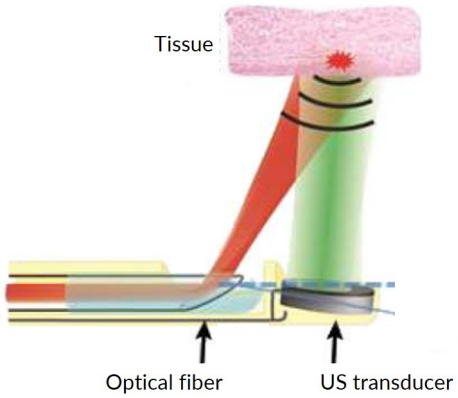

Figure 5.1: Concept of the overlap of the optical excitation beam (red) and the US reception beam (green) for IVPA. Due to catheter design choices, there is a certain offset before the beams overlap. Adapted from [61].

5.3.3. Implementation for IVPA

The algorithm is developed with IVUS data and characteristics as its focus and subsequently implemented for IVPA data. However, some differences in the fundamentals of the two image modalities affect the VSSA algorithm's applicability to IVPA data. IVUS contains a pulse-echo ultrasound beam, which beam shape is used to define the overlap of the RF lines. However, IVPA deals with a receive-only beam after instantaneous excitation of the tissue by an optical beam. The main assumption is that the optical beam uniformly excites all tissue, which generates sound waves captured by the receive-only US beam of the transducer. However, in a true scenario, the optical beam might be narrow and only selectively excite the tissue. Or, the optical beam starts as a focused beam and only diverges at larger depths due to scattering. Additionally, the US beam and optical beam have a certain overlap area due to their side-by-side placement in the catheter [61]. This is illustrated by Figure 5.1, which shows a limited overlap of the acoustic reflection field and optical beam depending on the optical fiber angle and transducer position. A method to deal with this is to develop a depth-dependent algorithm that considers the limitation of the optical excitation. In this version, the optical beam determines the beam shape used for the VSSA when reconstructing IVPA data.

Bibliography

[1] World Health Organization, "Leading Causes of Death and Disability 2000-2019: A Visual Summary," 2020. https://www.who.int/data/stories/leading-causes-of-death-and-disability-2000-2019-a-visual-summary.

[2] M. A. Khan, M. J. Hashim, H. Mustafa, M. Y. Baniyas, S. K. B. M. A. Suwaidi, R. AlKatheeri, F. M. K. Alblooshi, M. E. A. H. Almatrooshi, M. E. H. Alzaabi, R. S. A. Darmaki, and S. N. A. H. Lootah, "Global Epidemiology of Ischemic Heart Disease: Results from the Global Burden of Disease Study," *Cureus*, vol. 12, 7 2020.

[3] P. Libby, "The changing landscape of atherosclerosis," *Nature*, vol. 592, pp. 524–533, 4 2021.

[4] F. Sharif and R. T. Murphy, "Current Status of Vulnerable Plaque Detection," *Catheterization and Cardiovascular Interventions*, vol. 75, pp. 135–144, 1 2010.

[5] F. D. Kolodgie, R. Virmani, A. P. Burke, A. Farb, D. K. Weber, R. Kutys, and A. V. Finn, "Pathologic Assessment of the Vulnerable Human Coronary Plaque," *Heart*, vol. 90, pp. 1385–1391, 2004.

[6] M. J. Davies and A. C. Thomas, "Plaque Fissuring: The Cause of Acute Myocardial Infarction, Sudden Ischaemic death, and Crescendo Angina," *British Heart Journal*, vol. 53, pp. 363–73, 1985.

[7] J. A. Ambrose, M. A. Tannenbaum, D. Alexopoulos, C. E. Hjemdahl-Monsen, J. Leavy, M. Weiss, S. Borrico, R. Gorlin, and V. Fuster, "Angiographic Progression of Coronary Artery Disease and the Development of Myocardial Infarction," *Journal of the American College of Cardiology*, vol. 12, pp. 56–62, 7 1988.

[8] J. M. Stolker, D. J. Cohen, K. F. Kennedy, M. J. Pencina, J. B. Lindsey, L. Mauri, D. E. Cutlip, and N. S. Kleiman, "Repeat Revascularization after Contemporary Percutaneous Coronary Intervention: An Evaluation of Staged, Target Lesion, and Other Unplanned Revascularization Procedures during the First Year," *Circulation: Cardiovascular Interventions*, vol. 5, pp. 772–782, 12 2012.

[9] G. W. Stone, A. Maehara, A. J. Lansky, B. de Bruyne, E. Cristea, G. S. Mintz, R. Mehran, J. McPherson, N. Farhat, S. P. Marso, H. Parise, B. Templin, R. White, Z. Zhang, and P. W. Serruys, "A Prospective Natural-History Study of Coronary Atherosclerosis," *New England Journal of Medicine*, vol. 364, pp. 226–235, 1 2011.

[10] A. C. De Franco and S. E. Nissen, "Coronary Intravascular Ultrasound: Implications for Understanding the Development and Potential Regression of Atherosclerosis," *The American Journal of Cardiology*, vol. 88, pp. 7–20, 11 2001.

[11] H. M. Loree, R. D. Kamm, R. G. Stringfellow, and R. T. Lee, "Effects of Fibrous Cap Thickness on Peak Circumferential Stress in Model Atherosclerotic Vessels.," *Circulation Research*, vol. 71, no. 4, pp. 850–858, 1992.

[12] S. Sethuraman, S. R. Aglyamov, J. H. Amirian, R. W. Smalling, and S. Y. Emelianov, "Intravascular Photoacoustic Imaging Using an IVUS Imaging Catheter," *IEEE Transactions on Ultrasonics, Ferroelectrics, and Frequency Control*, vol. 54, no. 5, pp. 978–986, 2007.

[13] G. J. Tearney, E. Regar, T. Akasaka, T. Adriaenssens, P. Barlis, H. G. Bezerra, B. Bouma, N. Bruining, J. M. Cho, S. Chowdhary, M. A. Costa, R. De Silva, J. Dijkstra, C. Di Mario, D. Dudeck, E. Falk, M. D. Feldman, P. Fitzgerald, H. Garcia, N. Gonzalo, J. F. Granada, G. Guagliumi, N. R. Holm, Y. Honda, F. Ikeno, M. Kawasaki, J. Kochman, L. Koltowski, T. Kubo, T. Kume, H. Kyono, C. C. S. Lam, G. Lamouche, D. P. Lee, M. B. Leon, A. Maehara, O. Manfrini, G. S. Mintz, K. Mizuno, M. A. Morel, S. Nadkarni, H. Okura, H. Otake, A. Pietrasik, F. Prati, L. Rber, M. D. Radu, J. Rieber,

M. Riga, A. Rollins, M. Rosenberg, V. Sirbu, P. W. Serruys, K. Shimada, T. Shinke, J. Shite, E. Siegel, S. Sonada, M. Suter, S. Takarada, A. Tanaka, M. Terashima, T. Troels, S. Uemura, G. J. Ughi, H. M. Van Beusekom, A. F. Van Der Steen, G. A. Van Es, G. Van Soest, R. Virmani, S. Waxman, N. J. Weissman, and G. Weisz, "Consensus Standards for Acquisition, Measurement, and Reporting of Intravascular Optical Coherence Tomography Studies: A Report From the International Working Group for Intravascular Optical Coherence Tomography Standardization and Validation," *Journal of the American College of Cardiology*, vol. 59, pp. 1058–1072, 3 2012.

[14] T. J. Jun, S. J. Kang, J. G. Lee, J. Kweon, W. Na, D. Kang, D. Kim, D. Kim, and Y. H. Kim, "Automated Detection of Vulnerable Plaque in Intravascular Ultrasound Images," *Medical and Biological Engineering and Computing*, vol. 57, pp. 863–876, 4 2019.

[15] D. Vanderlaan, A. B. Karpiouk, D. Yeager, and S. Emelianov, "Real-Time Intravascular Ultrasound and Photoacoustic Imaging," *IEEE Transactions on Ultrasonics, Ferroelectrics, and Frequency Control*, vol. 64, p. 141, 1 2017.

[16] R. Waksman, C. Di Mario, R. Torguson, Z. A. Ali, V. Singh, W. H. Skinner, A. K. Artis, T. T. Cate, E. Powers, C. Kim, E. Regar, S. C. Wong, S. Lewis, J. Wykrzykowska, S. Dube, S. Kazziha, M. van der Ent, P. Shah, P. E. Craig, Q. Zou, P. Kolm, H. B. Brewer, H. M. Garcia-Garcia, H. Samady, J. Tobis, M. Zainea, W. Leimbach, D. Lee, T. Lalonde, W. Skinner, A. Villa, H. Liberman, G. Younis, R. de Silva, M. Diaz, L. Tami, J. Hodgson, G. Raveendran, N. Goswami, J. Arias, L. Lovitz, R. Carida, S. Potluri, F. Prati, A. Erglis, A. Pop, M. McEntegart, M. Hudec, U. Rangasetty, and D. Newby, "Identification of Patients and Plaques Vulnerable to Future Coronary Events with Near-infrared Spectroscopy Intravascular Ultrasound Imaging: A Prospective, Cohort Study," *The Lancet*, vol. 394, pp. 1629–1637, 11 2019.

[17] M. Jaguszewski, R. Klingenberg, and U. Landmesser, "Intracoronary Near-Infrared Spectroscopy (NIRS) Imaging for Detection of Lipid Content of Coronary Plaques: Current Experience and Future Perspectives," *Current Cardiovascular Imaging Reports*, vol. 6, p. 426, 10 2013.

[18] B. Wang, A. Karpiouk, D. Yeager, J. Amirian, S. Litovsky, R. Smalling, and S. Emelianov, "In Vivo Intravascular Ultrasound-guided Photoacoustic Imaging of Lipid in Plaques using an Animal Model of Atherosclerosis," *Ultrasound in Medicine & Biology*, vol. 38, p. 2098, 12 2012.

[19] S. Brugaletta, H. M. Garcia-Garcia, P. W. Serruys, S. De Boer, J. Ligthart, J. Gomez-Lara, K. Witberg, R. Diletti, J. Wykrzykowska, R. J. Van Geuns, C. Schultz, E. Regar, H. J. Duckers, N. Van Mieghem, P. De Jaegere, S. P. Madden, J. E. Muller, A. F. Van Der Steen, W. J. Van Der Giessen, and E. Boersma, "NIRS and IVUS for Characterization of Atherosclerosis in Patients Undergoing Coronary Angiography," *Journal of the American College of Cardiology: Cardiovascular Imaging*, vol. 4, pp. 647–655, 6 2011.

[20] S. Iskander-Rizk, M. Wu, G. Springeling, H. M. van Beusekom, F. Mastik, M. te Lintel Hekkert, R. H. Beurskens, A. Hoogendoorn, E. M. Hartman, A. F. van der Steen, J. J. Wentzel, and G. van Soest, "In Vivo Intravascular Photoacoustic Imaging of Plaque Lipid in Coronary Atherosclerosis," *EuroIntervention*, vol. 15, pp. 452–456, 8 2019.

[21] K. Jansen, A. F. W. van der Steen, H. M. M. van Beusekom, J. W. Oosterhuis, and G. van Soest, "Intravascular Photoacoustic Imaging of Human Coronary Atherosclerosis," *Optics Letters*, vol. 36, p. 597, 3 2011.

[22] M. Wu, K. Jansen, G. v. Soest, and A. F. W. v. d. Steen, "Specific Imaging of Atherosclerotic Plaque Lipids with Two-wavelength Intravascular Photoacoustics," *Biomedical Optics Express, Vol. 6, Issue 9, pp. 3276-3286*, vol. 6, pp. 3276–3286, 9 2015.

[23] X. F. Gao, Z. Ge, X. Q. Kong, J. Kan, L. Han, S. Lu, N. L. Tian, S. Lin, Q. H. Lu, X. Y. Wang, Q. H. Li, Z. Z. Liu, Y. Chen, X. S. Qian, J. Wang, D. Y. Chai, C. H. Chen, T. Pan, F. Ye, J. J. Zhang, and S. L. Chen, "3-Year Outcomes of the ULTIMATE Trial Comparing Intravascular Ultrasound Versus Angiography-Guided Drug-Eluting Stent Implantation," *Journal of the American College of Cardiology: Cardiovascular Interventions*, vol. 14, pp. 247–257, 2 2021.

[24] S. J. Hong, G. S. Mintz, C. M. Ahn, J. S. Kim, B. K. Kim, Y. G. Ko, T. S. Kang, W. C. Kang, Y. H. Kim, S. H. Hur, B. K. Hong, D. Choi, H. Kwon, Y. Jang, and M. K. Hong, "Effect of Intravascular Ultrasound–Guided Drug-Eluting Stent Implantation: 5-Year Follow-Up of the IVUS-XPL Randomized Trial," *Journal of the American College of Cardiology: Cardiovascular Interventions*, vol. 13, pp. 62–71, 1 2020.

[25] C. di Mario, K. C. Koskinas, and L. Räber, "Clinical Benefit of IVUS Guidance for Coronary Stenting: The ULTIMATE Step Toward Definitive Evidence?," *Journal of the American College of Cardiology*, vol. 72, pp. 3138–3141, 12 2018.

[26] J. Dijkstra, G. Koning, and J. H. C. Reiber, "Quantitative Measurements in IVUS Images," *International Journal of Cardiac Imaging*, no. 15, pp. 513–522, 1999.

[27] C. Peng, H. Wu, S. Kim, X. Dai, and X. Jiang, "Recent Advances in Transducers for Intravascular Ultrasound (IVUS) Imaging," *Sensors*, vol. 21, p. 3540, 5 2021.

[28] S. Kang, J. Lee, and J. H. Chang, "Effectiveness of Synthetic Aperture Focusing and Coherence Factor Weighting for Intravascular Ultrasound Imaging," *Ultrasonics*, vol. 113, 5 2021.

[29] M. Yu, Y. Li, T. Ma, K. K. Shung, and Q. Zhou, "Intravascular Ultrasound Imaging with Virtual Source Synthetic Aperture Focusing and Coherence Factor Weighting," *IEEE Transactions on Medical Imaging*, vol. 36, pp. 2171–2178, 10 2017.

[30] K. Moore, "Essential Clinical Anatomy," pp. 1022–1033, 2014.

[31] M. J. Davies, "Stability and Instability: Two Faces of Coronary Atherosclerosis. The Paul Dudley White Lecture 1995," *Circulation*, vol. 94, no. 8, pp. 2013–2020, 1996.

[32] "Percutaneous Coronary Intervention (PCI)," 2021. `https://my.clevelandclinic.org/health/treatments/22066-percutaneous-coronary-intervention`.

[33] N. Bom, A. van der Steen, and C. Lancée, *History and Principles*. PhD thesis, 2003.

[34] A. E. Powles, D. J. Martin, I. T. Wells, and C. R. Goodwin, "Physics of Ultrasound," *Anaesthesia & Intensive Care Medicine*, vol. 19, pp. 202–205, 4 2018.

[35] A. Manbachi and R. S. Cobbold, "Development and application of piezoelectric materials for ultrasound generation and detection," *Ultrasound*, vol. 19, pp. 187–196, 11 2011.

[36] G. S. Mintz, S. E. Nissen, W. D. Anderson, S. R. Bailey, R. Erbel, P. J. Fitzgerald, F. J. Pinto, K. Rosenfield, R. J. Siegel, E. Murat Tuzcu, P. G. Yock, R. A. O'Rourke, J. Abrams, E. R. Bates, B. R. Brodie, P. S. Douglas, G. Gregoratos, M. A. Hlatky, J. S. Hochman, S. Kaul, C. M. Tracy, D. D. Waters, and W. L. Winters, "American College of Cardiology Clinical Expert Consensus Document on Standards for Acquisition, Measurement and Reporting of Intravascular Ultrasound Studies (IVUS)," *Journal of the American College of Cardiology*, vol. 37, pp. 1478–1492, 4 2001.

[37] H. ten Hoff, *Scanning Mechanisms for Intravascular Ultrasound Imaging : A Flexible Approach*. PhD thesis, 1993.

[38] R. Cobbold, *Foundations of Biomedical Ultrasound*. Oxford University Press, 2007.

[39] M. Baad, Z. F. Lu, I. Reiser, and D. Paushter, "Clinical Significance of US Artifacts," *Radiographics*, vol. 37, no. 5, pp. 1408–1423, 2017.

[40] K. Jansen, G. Van Soest, and A. F. van der Steen, "Intravascular Photoacoustic Imaging: A New Tool for Vulnerable Plaque Identification," *Ultrasound in Medicine & Biology*, vol. 40, pp. 1037–1048, 6 2014.

[41] L. V. Wang, "Photoacoustic Imaging and Spectroscopy," p. 518.

[42] V. Daeichin, M. Wu, N. De Jong, A. F. van der Steen, and G. van Soest, "Frequency Analysis of the Photoacoustic Signal Generated by Coronary Atherosclerotic Plaque," *Ultrasound in Medicine and Biology*, vol. 42, pp. 2017–2025, 8 2016.

[43] T. Zhao, A. E. Desjardins, S. Ourselin, T. Vercauteren, and W. Xia, “Minimally Invasive Photoacoustic Imaging: Current Status and Future Perspectives,” *Photoacoustics*, vol. 16, p. 100146, 12 2019.

[44] K. Jansen, A. F. van der Steen, M. Wu, H. M. van Beusekom, G. Springeling, X. Li, Q. Zhou, K. Kirk Shung, D. P. de Kleijn, and G. van Soest, “Spectroscopic Intravascular Photoacoustic Imaging of Lipids in Atherosclerosis,” *Journal of Biomedical Optics*, vol. 19, p. 026006, 2 2014.

[45] J. Kortbek, J. A. Jensen, and K. L. Gammelmark, “Synthetic Aperture Focusing Applied to Imaging Using a Rotating Single Element Transducer,” *Proceedings - IEEE Ultrasonics Symposium*, pp. 1504–1507, 2007.

[46] C. H. Frazier and W. D. O’Brien, “Synthetic Aperture Techniques with a Virtual Source Element,” *IEEE Transactions on Ultrasonics, Ferroelectrics, and Frequency Control*, vol. 45, no. 1, pp. 196–207, 1998.

[47] F. S. Foster, C. J. Pavlin, K. A. Harasiewicz, D. A. Christopher, and D. H. Turnbull, “Advances in Ultrasound Biomicroscopy,” *Ultrasound in Medicine and Biology*, vol. 26, no. 1, pp. 1–27, 2000.

[48] S. Nikolov and J. A. Jensen, “Virtual Ultrasound Sources in High-Resolution Ultrasound Imaging,” *SPIE Medical Imaging*, vol. 4687, pp. 395–405, 4 2002.

[49] B. Goossens, I. Despotoví, E. Vansteenkiste, A. Pižurica, and W. Philips, “Using Phase Information in Ultrasound RF-signals for Tissue Characterization,” *Image Processing and Interpretation, Ghent University*, 2008.

[50] D. Garcia, “Make the Most of MUST, An Open-Source Matlab UltraSound Toolbox,” *IEEE International Ultrasonics Symposium, IUS*, 2021.

[51] D. Garcia, “SIMUS: An Open-Source Simulator for Medical Ultrasound iImaging. Part I: Theory & Examples,” *Computer Methods and Programs in Biomedicine*, vol. 218, 5 2022.

[52] K. F. Üstüner and G. L. Holley, “Ultrasound Imaging System Performance Assessment,” tech. rep., 2003.

[53] C. Passmann and H. Ermert, “In Vivo Imaging of the Skin in the 100 MHz Region Using the Synthetic Aperture Concept,” *Proceedings of the IEEE Ultrasonics Symposium*, vol. 2, pp. 1287–1290, 1995.

[54] C. Passmann and H. Ermert, “A 100-MHz Ultrasound Imaging System for Dermatologic and Ophthalmologic Diagnostics,” *IEEE Transactions on Ultrasonics, Ferroelectrics, and Frequency Control*, vol. 43, no. 4, pp. 545–552, 1996.

[55] V. R. Amin, *Ultrasonic attenuation estimation for tissue characterization*. PhD thesis, Iowa State University, Digital Repository, Ames, 1989.

[56] S. M. Al-Qahtani and C. M. Langton, “Ultrasound Temporal-spatial Phase-interference in Complex Composite Media; A Comparison of Experimental Measurement and Simulation Prediction,” *Ultrasonics*, vol. 71, pp. 115–126, 9 2016.

[57] University of Conneticut, “Constructive and Destructive Interference.” `https://www.phys.uconn.edu/~gibson/Notes/Section5_2/Sec5_2.htm`.

[58] B. Lokesh and A. K. Thittai, “Design of a Low Cost Ultrasound System using Diverging Beams and Synthetic Aperture Approach: Preliminary Study,” *Proceedings - International Symposium on Biomedical Imaging*, pp. 1108–1111, 6 2017.

[59] C. E. Shannon, “Communication in the Presence of Noise,” *Proceedings of the IRE*, vol. 37, no. 1, pp. 10–21, 1949.

[60] P. E. Wellstead, “Signal Aliasing in System Identification,” *International Journal of Control*, vol. 22, no. 3, pp. 363–375, 1975.

[61] M. Wu, K. Jansen, G. Springeling, A. F. W. v. d. Steen, and G. v. Soest, “Impact of Device Geometry on the Imaging Characteristics of an Intravascular Photoacoustic Catheter,” *Applied Optics, Vol. 53, Issue 34, pp. 8131-8139*, vol. 53, pp. 8131–8139, 12 2014.

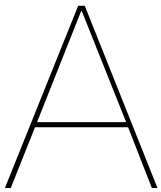

Appendix A - Literature Review

Image Reconstruction for Intravascular Ultrasound and Photoacoustics to Detect Lipid-Rich Atherosclerotic Plaques in Human Coronary Arteries: A Scoping Review

Amerens Bekkers
Biomedical Engineering, Technical University of Delft, the Netherlands

Abstract

Intravascular Ultrasound (IVUS) combined with Intravascular Photoacoustics (IVPA) is a novel imaging modality that can potentially improve the diagnosis of vulnerable atherosclerotic plaques by accurate imaging of lipids in the coronary arteries. Rupture of these lipid-rich plaques is the most common cause of acute events in patients with Coronary Artery Disease (CAD). IVUS is based on the reception of echoes of the transmitted ultrasound waves that originate from acoustical impedance differences at tissue boundaries, which enables visualization of the vessel morphology. IVPA detects sound waves that are generated from a local pressure rise in the tissue after absorption of the emitted pulsed laser light. This can be used for visualization of the lipid content by using laser light of specific wavelengths that is maximally absorbed by lipids. Combining these imaging methods can provide clinically relevant information to diagnose lipid-rich atherosclerotic plaques. So far, IVUS and IVPA imaging is not clinically available yet. A step toward introducing this modality to the clinic is to develop an image reconstruction method to obtain high-quality images. Therefore, this review aims to find the state-of-the-art image reconstruction for IVUS and IVPA imaging with a rotating single-element side-viewing catheter. This scoping review provides a categorized overview of the image reconstruction algorithms that are included after a systematic literature search of 507 studies in PubMed and IEEExplore. After evaluating these algorithms on performance regarding image quality, computational time, reproducibility, and the study methods, six algorithms are considered the most interesting for IVUS and IVPA image reconstruction. These algorithms aim to improve spatial resolution, reduce noise, or correct catheter motion.

Keywords: Intravascular Ultrasound; Intravascular Photoacoustics; Vulnerable plaque; Image reconstruction;

I. Introduction

Coronary Artery Disease (CAD) is the leading cause of death worldwide [1]. CAD is primarily caused by atherosclerosis [2], which leads to lipid accumulation and calcification in the coronary arteries [2], [3]. This atherosclerotic mechanism can form large lipid-rich plaques with a necrotic core that is contained by a thin fibrous cap [4], [5]. This type of plaque is also referred to as thin-cap fibroatheroma (TCFA) or vulnerable plaque. Rupture of a vulnerable plaque can lead to thrombus formation and subsequent obstruction of the blood flow, which is the most common cause of acute coronary events like myocardial infarction [6], [7]. Many patients suffering from obstructive CAD are treated by percutaneous coronary intervention (PCI) [8], [9]. Still, 12% of the patients that underwent PCI need another intervention within the first year due to cardiac events caused by the culprit or non-culprit plaques [8], [9]. This indicates the importance of more accurate detection of all lipid-rich plaques at risk. Currently, Intravascular Ultrasound (IVUS) is the gold standard for in vivo intravascular imaging of the coronary arteries [10] and performs well in detecting calcification and stenosis [11]. However, since IVUS lacks adequate soft-tissue contrast, it can neither be used for measurement of the fibrous cap thickness nor the detection of the lipid-core, which are two key features of vulnerable plaques [12], [13]. To overcome these limitations of IVUS, other imaging modalities aim to provide more accurate intravascular imaging and quantification of vulnerable plaque features. Intravascular Optical Coherence tomography (IV-OCT) detects the reflection of the emitted near-infrared light to visualize the arterial wall [14]. Therefore, it is referred to as the optical analog of IVUS because IVUS detects the echo of the transmitted ultrasound wave generated from tissue boundaries [14]. IV-OCT provides a high spatial resolution which enables identifying the fibrous cap thickness [4], [5], [14], [15], but does have a limited penetration depth of 1-2 mm [4], [14]. Another modality is Near-Infrared Spectroscopy (NIRS), which can detect lipids by identifying the chemical components of the tissue. The amount of near-infrared light that is absorbed or reflected can be used for this tissue characterization because each tissue component has a unique absorption pattern over a certain wavelength range [16]. However, the NIRS signal and thus the lipid distribution is not depth-resolved [4], [15], [17]. Moreover, NIRS cannot measure the fibrous cap thickness [14].

A novel imaging modality is IVUS combined with intravascular photoacoustics (IVPA). Photoacoustic (PA) imaging (PAI) is based on the optical absorption of pulsed laser light. This causes transient thermoelastic expansion and local tissue heating, which generates a pressure sound

wave. Detecting this sound wave allows for accurate reconstruction of the absorption site [17], [18]. When using specific wavelengths, IVPA can detect lipid content which is fundamental in the diagnosis of vulnerable plaque [19] and provides clinically relevant information that could improve diagnosis and enhance intervention strategy [13], [20]. Due to the combination with IVUS, the lipids can be imaged alongside good morphological imaging of the arterial wall [14]. IVPA has been applied to human plaque specimens and large-animal coronary atherosclerosis models but is not clinically available yet. A step in the development of this imaging modality is an image reconstruction method to obtain high-quality images. Therefore, this scoping review aims to provide an overview of the state-of-the-art image reconstruction and processing techniques for IVUS and IVPA to verify their ability to detect lipid-rich atherosclerotic plaques.

A literature search for IVUS and IVPA image reconstruction will be performed. The imaging of both modalities is based on the reception of acoustic waves, hence image reconstruction algorithms could therefore be mutually applicable. However, a difference in the literature search is required because IVPA is not performed much yet whereas IVUS has been investigated extensively. Therefore, the US part can be focused on the intravascular application specifically, whereas the PA part aims to find image reconstruction methods from related PA imaging approaches, which can be adapted to the IVPA configuration. Thus, it needs to be defined which PA image reconstruction techniques could apply to IVPA imaging. PAI can be subdivided into two main categories: photoacoustic tomography (PAT) and photoacoustic microscopy (PAM). PAT relies on a multi-sensor approach to detect the sound waves at several angular positions around the imaging object using transducer arrays [21]. In PAM, a single-element transducer scans around or across the imaging object [21]. PAM has an optical-resolution (OR-PAM) and an acoustical-resolution (AR-PAM) imaging mode, where the resolution is determined by the optical laser beam or by the acoustic wave, respectively [21]. This scoping review considers a rotating side-viewing single-element transducer as the foreseen clinical application of IVUS and IVPA, hence PAM image reconstruction methods are most relatable to this IVPA configuration. The PAI approaches that are excluded for IVPA will be further described in Section II.
Finally, this review aim to answer the following research questions: (1) What is the state-of-the-art image reconstruction for single-element transducer IVUS? (2) What is the state-of-the-art image reconstruction for single-element transducer photoacoustic imaging that is likely also applicable to IVPA?

These research questions determine the literature search, which is further described in Section II. Section II also describes the eligibility and exclusion criteria and the approach to synthesizing the results. The results of the literature search and the characteristics of the included studies are described in Section III. Lastly, Section IV assesses which algorithms of the included studies belong to the state-of-the-art IVUS and IVPA image reconstruction by selecting the most optimal combination of algorithms.

II. Methods

A. Search Strategy

This literature review was conducted by following the guidelines of the Preferred Reporting Items for Systematic reviews and Meta-Analyses extension for Scoping Reviews (PRISMA-ScR) statement [22]. A systematic literature search was conducted in PubMed and IEEEXplore to find the optimal combination of clinical (PubMed) and technical (IEEEXplore) studies focusing on image reconstruction. The search queries of the IVUS and PA parts can be found in Appendix A. All studies published prior to the 1st of March 2022 are included in both literature searches. Besides the database search, studies can be additionally included upon recommendation of an expert in the IVUS or IVPA field or by reference searching. The latter means that a study from the reference list of a readily included study is found eligible.

B. Study Selection and Eligibility Criteria

The eligibility and exclusion criteria are described here. For both the IVUS and PA literature search, a study is found eligible when the following criteria are met: (1) English full text available, (2) the image reconstruction algorithm is described, (3) the reconstruction is based on single-element transducer data. This means that studies were excluded where a clinical application, the hardware system design, automatic quantification, or segmentation of the vessel components was the main topic instead of image reconstruction. Also, studies on other imaging modalities than IVUS and PA and studies that focus on reconstruction from sparse subsampled data were excluded. In addition, the IVUS and PA parts separately require some specific exclusion criteria. For IVUS, studies that perform motion correction based on ECG-gating were excluded because the foreseen clinical IVUS-IVPA imaging modality is a stand-alone device without ECG availability. In the case of PAI, studies on OR-PAM and PAT geometries with multiple transducers or transducer elements were excluded because these approaches are not similar enough to the IVPA configuration.

C. Results Synthesis

For each study, the algorithm, the method regarding the used data for experiments and the transducer characteristics, the main results, computational time, and some advantages and disadvantages are extracted and summarized. Then, the studies are categorized based on the problem that the proposed algorithm aims to solve, to provide a structured overview. The advantages and disadvantages of the algorithms are found by extracting strengths and limitations by critically assessing the studies. This critical assessment is performed by evaluating the relevance of the performed experiments and the quantitative metrics used to report the image quality, like spatial resolution, Signal-to-Noise (SNR),

or Contrast-to-Noise Ratio (CNR). Also, the reproducibility of the methods is evaluated and the limitations reported by the authors were extracted. Subsequently, the results will be discussed in Section IV to determine which algorithms have the most interesting features for intravascular atherosclerotic plaque detection. This specific clinical application requires prioritizing certain characteristics that weigh in determining which algorithms belong to the state-of-the-art image reconstruction. These characteristics are performance regarding image quality and computational efficiency to evaluate real-time applicability. Lastly, reproducibility of the algorithm is desired to enable implementation and subsequent testing on IVUS and IVPA data for translation into the clinical setting. This requires an extensive algorithm description or available code.

III. Results

A. Study Selection

From the electronic database search and hand searching, 507 studies were identified and screened, consisting of 267 and 240 studies for IVUS and PA, respectively. For IVUS, 23 duplicates and 217 studies were removed due to unrelated topics. 21 duplicates and 165 studies with an unrelated topic were removed for PA. Unrelated topics were automated quantification and segmentation of lumen components for the IVUS part. For the PA part, unrelated topics were array-based or tomographic imaging set-up or OR-PAM. For both parts, clinical applications, system designs, systems with unrelated characteristics, or when no image reconstruction, IVUS or PAI was involved were considered unrelated topics. Finally, 26 and 59 full texts are screened for eligibility. After exclusion by the criteria as shown in Figures 1 and 2, a total of 10 studies for IVUS and 15 for PA was included.

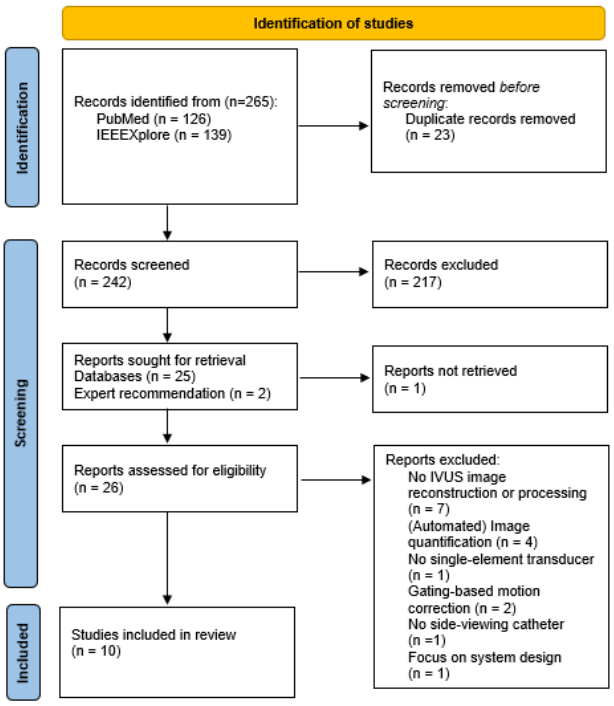

Fig. 1. Flow diagram of the IVUS literature search

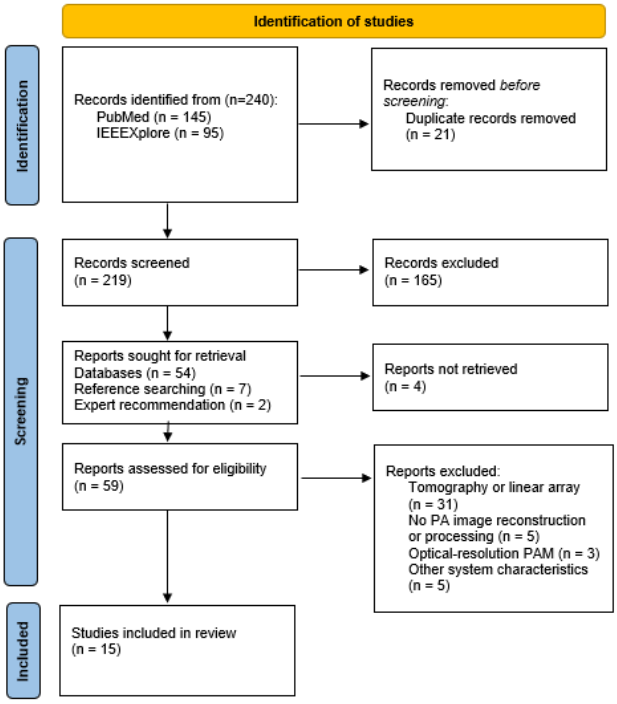

Fig. 2. Flow diagram of the PA literature search

B. Intravascular Ultrasound

The IVUS reconstruction algorithms could be subdivided into four categories as shown in Table 1 in Appendix B. These categories are spatial resolution improvement by Synthetic Aperture Focusing (SAF) Techniques (SAFT), noise reduction, motion correction, and 3D reconstruction. Most studies aim to improve the lateral resolution, which is the capability to distinguish imaging objects that are side-by-side and located at the same depth [23]. The other component of spatial resolution is axial resolution which is the capability to distinguish imaging objects at different depths along the beam axis [23]. The noise reduction algorithms treat blood noise, multiplicative noise, and an undefined noise type. The categories motion correction and 3D reconstruction only consist of one study. Furthermore, it should be noted that the computational time is only described for three out of 10 studies throughout all categories. Below, the algorithms will be described in more detail per category.

1) Spatial resolution improvement by Synthetic Aperture Focusing: SAFT are applied in IVUS to improve the spatial resolution by combining the signal of appropriately delayed adjacent A-lines [24]. A variety of

SAFT is proposed to achieve this resolution improvement [24]–[28]. A Display Pixel-Based Synthetic Aperture Focusing (DPBSAF) technique is proposed in [25] as an efficient method to remove the need for a Digital Scan Converter (DSC) that converts the data from Polar to Cartesian coordinates. The DSC potentially causes blurring and reduces the angular resolution of IVUS images. By avoiding the need for a DSC, the DPBSAF has a slightly improved Contrast-to-Noise Ratio (CNR) up to 2 dB and provides a better angular resolution compared to conventional SAF. In conventional SAF, the A-lines are delayed and summed to reconstruct the images. This is further referred to as Delay-and-Sum (DAS) beamforming. Furthermore, there are multiple algorithms included that operate in the frequency domain (FD). A time-domain algorithm is compared with an FD algorithm in [26] to evaluate their effectiveness in reducing elevated sidelobes and thus improving the lateral resolution. The lateral resolution was considered as high when a narrow main lobe and low sidelobes were obtained. The FD algorithm outperformed the time-domain algorithm because of a relatively narrow main lobe, small sidelobes, and a short computational time, yet it was only tested on phantom data [26]. Another FD algorithm is described in [27] that performs SAFT by taking the point spread function (PSF) characteristics into account. The results of [27] are not convincing because of a scarce quantification of the results and a lack of reproducible methods. Lastly, SAFT with coherence factor weighting (CFW) was evaluated by [24] and [28]. CFW suppresses the signal when there is a low coherence between the delayed A-lines [24]. Despite [28] describing theoretical evidence that SAF and CFW will deteriorate lateral resolution in single-element-based IVUS, both [24] and [28] report an increase in lateral resolution and CNR. A lateral resolution increase of 42% was reported for the virtual source SAFT with CFW (VSSA-CFW) of [24], compared with the original image which was reconstructed by stacking A-lines. Also [28] shows improvement of the lateral resolution and CNR, determined by the addition of CFW. Results are reported for conventional SAF, SAF, CFW, and SAF-CFW. Applying only CFW improves the lateral resolution compared to the other methods, but degrades the CNR by around 0.35 dB at 3 mm depth. On the other hand, applying only SAF increases the CNR by almost 1 dB but shows the worst lateral resolution [28]. The combination of SAF-CFW slightly improves the CNR too, which offers the optimal combination of a high SNR, CNR, and lateral resolution, which is required for measuring plaque burden [28]. This applicability for measuring plaque burden was also supported by [24], who also claim that VSSA-CFW could be applicable to IVPA imaging because it offers a high lateral resolution and low noise levels [24].

2) Noise Reduction: There are multiple ongoing efforts to reduce noise in IVUS images, as IVUS images are susceptible to various types of noise from hardware, blood backscatter, and other sources [29]–[31]. The efficacy of a blood noise reduction (BNR) algorithm is evaluated in [29]. The intra- and interobserver variability decreased when the BNR was applied to images of the cross-sectional area of the lumen and the so-called plaque plus media area. The latter is the area delineated by the adventitial border, minus the lumen area. This indicates that it does have a positive effect on the morphometric image analysis in areas that are important for lipid detection. The BNR takes 7 seconds to reconstruct one image, and real-time computations could become feasible with hardware improvements [29]. Besides only focusing on blood noise as in [29], the algorithm in [31] aims to remove all present image noise by digital subtraction. A background image to subtract from the final image is acquired by imaging blood only [31], which might not be possible in a real-time imaging setting. Lastly, a Nonlocal Total Variation (NLTV) method is described in [30] which aims to reduce speckle artifacts and multiplicative noise while maintaining the edges and image texture. This method reconstructs pixel values by minimizing a total variation model based on the similarities between image patches within a search window that is centered around the pixel that will be reconstructed. Besides SNR and a similarity metric, a no-reference metric that can evaluate image quality without needing a noiseless image as a reference is used for image quality evaluation. This is called the Natural Image Quality Estimator (NIQE). The NIQE and visual results show that the NLTV outperforms two other validated nonlocal denoising algorithms. The computational time dramatically increases with the search window size, whereas the SNR does not follow this trend. Therefore, it was found that a 40x40 search window is sufficient [30].

3) Motion Correction: Multiple sources of motion can distort the image quality. The motion between the transducer and the tissue is one of the most relevant motion types for IVUS because the acquired signal translates to the distance from the transducer to tissue components. By estimating the rigid rototranslation between subsequent IVUS images, the algorithm as described in [32] can reduce motion artifacts affecting the lateral view. The algorithm outperforms the fastest available method to reduce all short-axis motion artifacts, which was considered a state-of-the-art method. This was validated quantitatively by an adjusted version of the Cardiac Alignment Rate, which was introduced by Gil et al. (2007) [33]. This motion correction algorithm has a throughput of 3.16 frames per second [32].

4) 3D reconstruction: 3D reconstruction is performed to visualize a blood vessel in its entirety, instead of just 2D cross-sectional areas. A 3D reconstruction method where a natural cubic spline generates intermediary slices to form the 3D image is described in [34]. Since the intermediary slices are generated after acquiring the original slices, this method is likely not applicable to real-time imaging situations. This 3D reconstruction method visually performs better than a conventional pixel-based interpolation method. However, only wall thickness difference is described as a quantitative metric which provides only a narrow validation of the results. The main limitation of this algorithm is the assumption of no axial and rotational movement of the catheter in the artery,

whereas this is a well-known problem in in vivo arterial pullbacks [34].

C. Photoacoustic Imaging

The PA image reconstruction algorithms can be subdivided into four categories. The majority of studies describe an image reconstruction algorithm for AR-PAM. AR-PAM typically uses a focused transducer, which has a poor out-of-focus resolution as a consequence [35], [36]. Hence, the largest category consists of the various 1D- and 2D-SAFT and Fourier domain (FD) algorithms that aim to improve the out-of-focus resolution. Other categories are IVPA image reconstruction, algorithms that incorporate the heterogeneity of the imaging medium into the reconstruction, and Artificial Intelligence (AI). The studies are summarized in Table 2 in Appendix B and discussed in more detail below. Due to the exclusion of studies with multiple transducers or transducer elements, all included studies either use a single element transducer, or the transducer configuration was not specified.

1) IVPA image reconstruction: Despite its limited implementation, there are two studies included about IVPA image reconstruction [37], [38]. First, the efficacy of three conventional PA reconstruction methods applied to single-element IVPA was explored [37]. The estimation maximization (EM) method performs best compared to the filtered back projection and a lambda-tomography reconstruction [37]. Still, the EM visually does not show strong results and conducts ten iterations, which is likely to be computationally heavy. The need for high-speed imaging to enable real-time IVPA imaging is emphasized in [38]. Fast imaging is often achieved with a high repetition rate, which limits the SNR. However, [38] shows that Delay-and-Sum (DAS) and Modulation Transfer Function filtering improve the SNR while imaging at the rate of 12 frames per second. The best performance was found when the two methods were combined [38]. However, no other quantitative measures besides SNR were used to assess the performance.

2) Out-of-focus resolution improvement: AR-PAM can achieve a high lateral resolution when a transducer with a large numerical aperture (NA) is used because the lateral resolution in AR-PAM is defined as follows [39]:

$$R_{lateral} = \frac{0.71 \cdot c}{NA \cdot f} \tag{1}$$

where c is the speed of sound, f the central frequency and NA the numerical aperture of the transducer [39]. Therefore, the larger the NA, the better the lateral resolution in the focal region [35], [39]–[43]. Nevertheless, increasing the NA results in a more narrow focal region and thus deteriorates the lateral resolution in the out-of-focus region [35], [39]–[43]. Multiple studies aim to improve the out-of-focus resolution, indicating its importance for image quality [35], [36], [39]–[45]. An improved concept of conventional SAF were proposed by [35], [39], and [40]. First, the Virtual Detector (VD) based SAF with CFW by [40] increases the SNR up to 29 dB and improves the lateral resolution compared to the original image, which reconstruction method was not reported. Additional improvements in SNR and lateral resolution are achieved by taking a step further from conventional DAS beamforming in SAFT, which resulted in Delay-Multiply-And-Sum (DMAS) by [35] and a double-stage DMAS by [39]. Although [35] and [39] outperform DAS-SAFT in both resolution and contrast, it is computationally heavier than DAS. Where DMAS takes 15 seconds per image, it only takes 0.02 seconds per image for DAS [35]. The double-stage DMAS provides an even better lateral resolution and lowers the noise level by 14.3 dB in comparison with DMAS, but again at the cost of computational time. It needs 2 hours to compute 1024x2400x4000 sized data [39]. Computational acceleration by using a Graphics Processing Unit (GPU) is recommended, which can potentially enable real-time imaging [35], [39]. Generally, image reconstruction methods that operate in the Fourier domain (FD) are faster [44], [36] shows that an FD algorithm is up to 28 times faster than DAS for a similar performance in CNR and lateral resolution. Also, a SAFT in the FD was described in [41] which consists of two steps, namely Fourier Accumulation SAFT followed by directional model-based deconvolution. It improves the lateral resolution, but with approximately 80 seconds for reconstructing data with size 121x121x30, it is not as fast as expected for an FD algorithm [41]. Furthermore, [42] and [43] aim to improve the out-of-focus resolution by using a 2D-SAFT method. The directional 2D-SAFT from [42] has a high computational cost, while it does not show a significant performance improvement in lateral resolution compared to a 1D SAFT equivalent, which has a substantially shorter computational time. Secondly, 2D-SAFT as described in [43] had an improved overall resolution in two directions, whereas the 1D-SAFT has a better resolution in the B-scan direction along the x or y-axis. No computation time was reported, but a comparable computational burden as [42] is assumed, which took around 600 seconds to reconstruct one 2D image. Lastly, the potential real-time application of a 3D reconstruction method by an adjusted VD implementation combined with a Non-Uniform Fast Fourier Transform (NUFFT) is described in [44] to improve the out-of-focus resolution. The proposed algorithm was the most time-efficient with 11.1 seconds and had the best full field-of-view resolution by comparing the results to DAS, Stolt migration, a time-reversal, and a conventional model-based image reconstruction algorithm. In more detail, the proposed algorithm achieved the smallest FWHM of 88.39 μm, 176 μm, and 1.11 or 1.77 mm for a resolution test phantom, a hair phantom, and two in vivo blood vessels respectively [44].

3) Heterogeneous media: Most traditional VD-SAFT image reconstruction methods like in [35], [44] assume homogeneous media [46]. This is an inaccurate assumption because the speed of sound varies in the different tissue components of the arterial wall [47]. To take this heterogeneity into account, a method to automatically select the mean speeds of sound for optimal PA signals was developed [48]. This algorithm needs input based on

prior knowledge, namely a region of interest [48]. However, this prior knowledge about the regions of interest, such as the location of the vulnerable plaques, is not available. Another method to include various speeds of sound in the reconstruction is proposed in [46]. This is an FD-based VD that incorporates tissue heterogeneity by wavefield extrapolation. It shows good performance by obtaining a smaller FWHM and relative error than conventional VD-SAFT for out-of-focus imaging in an all-fluid and a fluid-solid-fluid layer phantom. Due to a similar NUFFT as in [44], this FD-based VD concept is very efficient and needs only around 0.7 seconds to reconstruct a 3D image without GPU acceleration [46].

4) Artificial Intelligence in PAI reconstruction: Despite the emerging application of AI in PAI, only two studies were included that use AI for image reconstruction specifically that is potentially translatable to the IVPA imaging configuration. First, in [49] a dictionary learning approach is used in PAM to remove reverberation artifacts. This method visualizes microvasculature, which was previously obscured due to reverberation artifacts caused by material with stronger absorption like bone [49]. Second, [50] describes a pattern-learning-based method that shows a good performance in the removal of interference noise with a stable pattern. This algorithm could be applied to a broad spectrum of interference noise because there are many sources of interference noise, but it cannot remove all noise types. The findings of only two studies are not sufficient to evaluate the potential of AI applications in PAI. Therefore, a more broad review by Gröhl et al. (2021) [51] of 83 papers on the use of Deep Learning (DL) in all biomedical PAI modalities was consulted to evaluate its prospect. Since not all PAI configurations can be applied to IVPA, the results can only give a general insight into whether the use of AI could be beneficial for IVPA. It was found that the first results of DL in PAI are undoubtedly promising. However, a lack of clinical validation studies and experimental data hinders DL for PAI from regular use in the clinic. When these bottlenecks can be overcome, direct image reconstruction with DL can significantly impact real-time imaging because it can drastically reduce reconstruction time. However, when the objective is to standardize and generalize image reconstruction methods, it is recommended to apply DL methods that use additional information or require handcrafted features [51].

IV. Discussion

This review aims to find the state-of-the-art image reconstruction for IVUS and IVPA to detect lipid-rich atherosclerotic plaques in human coronary arteries. An overview of 25 image reconstruction algorithms and their characteristics, advantages, and disadvantages was created. To the author's best knowledge, this is the first review that provides an overview of image reconstruction algorithms that can be applied to IVUS combined with IVPA. The proposed algorithms are active in different categories. They aim to improve spatial resolution, reduce noise, correct motion, reconstruct 3D images, or account for heterogeneous media with varying sound speeds. Besides two studies that apply AI in PAI, a recent review on DL in PAI was included to define the prospect of AI in PAI. An optimal combination of the algorithms will be determined and proposed in this section as the state-of-the-art image reconstruction for IVUS and IVPA imaging of atherosclerotic plaque.

A. Intravascular Ultrasound

For the IVUS part, two algorithms are considered the best solutions within the spatial resolution improvement category. These are the Display Pixel-based SAF (DPBSAF) as described in [25] and the VSSA focusing with CFW of [24]. The DPBSAF is a relatively simple method that can also increase contrast and spatial resolution besides reducing blurring [25], which is a positive synergistic effect. The VSSA focusing technique with CFW was most clearly described in [24] and was claimed to also be applicable in IVPA. Besides poor spatial resolution, speckle is another main contributor to a degraded IVUS signal [30], [52]. Speckle is caused by the interference of ultrasound pulses and random scatterers [30]. These speckle artifacts and multiplicative noise types are successfully removed by the Nonlocal Total Variation (NLTV) algorithm as described in [30], which is therefore seen as the most relevant algorithm from its category. Lastly, the motion correction method [32] that successfully reduces the motion caused by heart movement and by vessel tortuosity is considered relevant too. The study on the 3D reconstruction category is discarded due to the required prior tissue segmentation as an algorithm input.

B. Photoacoustic Imaging

Even though two studies reported IVPA image reconstruction, there are still possibilities for improvement as described in Section III-C1. Multiple PA studies aim to improve the out-of-focus resolution. This could also benefit the image quality of the foreseen IVUS and IVPA imaging modality because the unfocused ultrasound beams have a natural focus where the lateral resolution is the highest. The majority of the included studies achieve this improvement by applying either a 1D-SAFT or 2D-SAFT. It was found that the 2D-SAFT methods only partially or slightly outperform more conventional 1D-SAFT regarding spatial resolution. This slight two-directional spatial resolution increase is not worth the drastic increase in computational complexity. Therefore, a 1D SAFT is preferred over a 2D-SAFT. Multiple studies on 1D-SAFT are included, that are discarded because of their long computational times (see Table 2 in Appendix B), except for the FD algorithm as described in [36]. Despite its efficiency, it performs equally to conventional DAS regarding the obtained image quality, which is not considered a state-of-the-art technology and is therefore discarded. The algorithm within this category that is considered the strongest candidate for out-of-focus resolution improvement is the fast model-based approach with NUFFT in [44]. The reconstruction of a 200x200x150 data set takes only 8.15 seconds, which is relatively fast. Furthermore, it improves the spatial resolution by 64.8% compared to DAS for hair phantom data by taking the analytical transducer

beam pattern into account [44]. Lastly, the category that accounts for heterogeneous media is deemed relevant because the homogeneity of the imaging medium is often wrongfully assumed in SAFT [46]. The algorithm in [46] corrects for this and is considered the most suitable algorithm within the category because of its high reconstruction speed of 0.7 seconds for data of size 40x40x2000.

C. *Limitations*

This review has some limitations and other aspects to consider. First, it is good to note that most studies assume a focused transducer in the theoretical concept of the algorithm or use a focused transducer in their experiments. Focused transducers inherently provide a better spatial resolution because of a more narrow beamwidth [28]. Kang et al. (2021) [28] even claimed that conventional imaging with a focused transducer outperforms the results of flat transducer imaging with SAFT and CFW in spatial resolution and contrast. Thus, not all studies can be compared one to one, due to variations in the used transducer type. Also, other aspects like the difference in transducer frequency and the variations in reported quantitative metrics complicate a direct comparison between studies. Therefore, it is recommended for further research to present a more quantitative comparison between studies. This can perhaps be approached by determining a theoretical best image quality that can be achieved per imaging setup. How far the algorithm results are from this theoretical best, provides a comparable quantitative metric. The theoretical best image quality can be defined for example by calculating the lateral and axial resolution based on the transducer characteristics. Moreover, a theoretically best lateral resolution can be found by defining the effective aperture of the transducer geometry. This can be used to subsequently calculate the natural focal depth, as that can be used to determine the lateral resolution for unfocused transducers [23]. Second, an unexpected finding was that the noise reduction category is absent in the PA part. Since all signals, including PA signals, have a noise component, it is remarkable that besides the DL studies, there are no PA noise removal algorithms found in this review. However, multiple PA algorithms that are described in this review do perform noise reduction steps. Lastly, this review focuses on reconstructing high-quality images with good contrast and high spatial resolution because this is an important foundation to enable the diagnosis of vulnerable atherosclerotic plaques. Moreover, this diagnosis can be further improved by quantifying certain features like fibrous cap thickness and the size of the lipid core, as described before. Quantification algorithms are beyond the scope of this review. However, it is recommended for future work. Reviewing the image processing algorithms for quantification of the IVPA signal can further benefit the diagnostic accuracy of vulnerable atherosclerotic plaques that can cause acute events in CAD patients.

V. Conclusion

A combination of six algorithms was seen as optimal image reconstruction for IVUS and IVPA for imaging atherosclerotic vulnerable plaques. The algorithms can be seen as a chain or complementary solution to increase image quality. The first step is to improve the spatial resolution with a SAF-based technique. This can be the VSSA focusing and CFW of [24], the FD-based VD concept from [44] where the analytical beam pattern is taken into account or the Display Pixel-based SAF in [25] where the beams are directly focused on the display pixels to avoid errors in conversion from Polar to Cartesian coordinates. Subsequently, the image quality can be further improved by reducing the speckle artifacts by the Nonlocal Total Variation algorithm [30] and incorporating the medium heterogeneity by the FD-based VD concept as described in [46]. Lastly, the motion reduction of [32] can be applied when stacking the 2D images to obtain a smooth longitudinal image of the vessel. Some algorithms are either claimed to work on the other imaging modality data as well, which will be clear after testing the algorithm on data of both IVUS and IVPA. Also, after implementing and testing these algorithms, a first image reconstruction method can be for the novel IVUS and IVPA imaging modality. Moreover, when sufficient clinical validation studies and experimental data are available, AI could greatly impact PA image reconstruction in reconstruction speed and standardization.

References

[1] World Health Organization, "Leading causes of death and disability 2000-2019: A visual summary," 2020.

[2] M. A. Khan, M. J. Hashim, H. Mustafa, M. Y. Baniyas, S. K. B. M. A. Suwaidi, R. AlKatheeri, F. M. K. Alblooshi, M. E. A. H. Almatrooshi, M. E. H. Alzaabi, R. S. A. Darmaki, and S. N. A. H. Lootah, "Global Epidemiology of Ischemic Heart Disease: Results from the Global Burden of Disease Study," *Cureus*, vol. 12, 7 2020.

[3] M. Mehu, C. A. Narasimhulu, and D. K. Singla, "Inflammatory Cells in Atherosclerosis," *Antioxidants (Basel, Switzerland)*, vol. 11, p. 233, 1 2022.

[4] F. Sharif and R. T. Murphy, "Current status of vulnerable plaque detection," *Catheterization and cardiovascular interventions : official journal of the Society for Cardiac Angiography & Interventions*, vol. 75, pp. 135–144, 1 2010.

[5] T. J. Jun, S. J. Kang, J. G. Lee, J. Kweon, W. Na, D. Kang, D. Kim, D. Kim, and Y. H. Kim, "Automated detection of vulnerable plaque in intravascular ultrasound images," *Medical and Biological Engineering and Computing*, vol. 57, pp. 863–876, 4 2019.

[6] M. J. Davies, A. C. Thomas, J. Davies, and S. George', "Plaque fissuring-the cause of acute myocardial infarction, sudden ischaemic death, and crescendo angina A number of clinical angiographic appearances-including persistent retention of con-Requests for reprints to Professor M," *Br HeartJ*, vol. 53, pp. 363–73, 1985.

[7] J. A. Ambrose, M. A. Tannenbaum, D. Alexopoulos, C. E. Hjemdahl-Monsen, J. Leavy, M. Weiss, S. Borrico, R. Gorlin, and V. Fuster, "Angiographic progression of coronary artery disease and the development of myocardial infarction," *Journal of the American College of Cardiology*, vol. 12, pp. 56–62, 7 1988.

[8] J. M. Stolker, D. J. Cohen, K. F. Kennedy, M. J. Pencina, J. B. Lindsey, L. Mauri, D. E. Cutlip, and N. S. Kleiman, "Repeat revascularization after contemporary percutaneous coronary intervention: An evaluation of staged, target lesion, and other unplanned revascularization procedures during the first year," *Circulation: Cardiovascular Interventions*, vol. 5, pp. 772–782, 12 2012.

[9] G. W. Stone, A. Maehara, A. J. Lansky, B. de Bruyne, E. Cristea, G. S. Mintz, R. Mehran, J. McPherson, N. Farhat, S. P. Marso, H. Parise, B. Templin, R. White, Z. Zhang, and P. W. Serruys, "A Prospective Natural-History Study of Coronary Atherosclerosis," *New England Journal of Medicine*, vol. 364, pp. 226–235, 1 2011.

[10] M. K. Hong and S. Y. Lee, "Intravascular Ultrasound for Percutaneous Coronary Intervention: Benefits and Limitations," *JACC: Cardiovascular Interventions*, vol. 14, pp. 258–260, 2 2021.

[11] A. C. De Franco and S. E. Nissen, "Coronary intravascular ultrasound: implications for understanding the development and potential regression of atherosclerosis," *The American Journal of Cardiology*, vol. 88, pp. 7–20, 11 2001.

[12] H. M. Loree, R. D. Kamm, R. G. Stringfellow, and R. T. Lee, "Effects of fibrous cap thickness on peak circumferential stress in model atherosclerotic vessels.," *Circulation Research*, vol. 71, no. 4, pp. 850–858, 1992.

[13] S. Sethuraman, S. R. Aglyamov, J. H. Amirian, R. W. Smalling, and S. Y. Emelianov, "Intravascular photoacoustic imaging using an IVUS imaging catheter," *IEEE Transactions on Ultrasonics, Ferroelectrics, and Frequency Control*, vol. 54, no. 5, pp. 978–986, 2007.

[14] A. v. Veelen, N. M. R. v. d. Sangen, R. Delewi, M. A. M. Beijk, J. P. S. Henriques, and B. E. P. M. Claessen, "Detection of Vulnerable Coronary Plaques Using Invasive and Non-Invasive Imaging Modalities," *Journal of Clinical Medicine*, vol. 11, p. 1361, 3 2022.

[15] D. Vanderlaan, A. B. Karpiouk, D. Yeager, and S. Emelianov, "Real-Time Intravascular Ultrasound and Photoacoustic Imaging," *IEEE transactions on ultrasonics, ferroelectrics, and frequency control*, vol. 64, p. 141, 1 2017.

[16] S. Waxman, "Near-infrared spectroscopy for plaque characterization," *Journal of Interventional Cardiology*, vol. 21, pp. 452–458, 12 2008.

[17] B. Wang, A. Karpiouk, D. Yeager, J. Amirian, S. Litovsky, R. Smalling, and S. Emelianov, "In vivo intravascular ultrasound-guided photoacoustic imaging of lipid in plaques using an animal model of atherosclerosis," *Ultrasound in medicine & biology*, vol. 38, p. 2098, 12 2012.

[18] S. Iskander-Rizk, M. Wu, G. Springeling, H. M. van Beusekom, F. Mastik, M. te Lintel Hekkert, R. H. Beurskens, A. Hoogendoorn, E. M. Hartman, A. F. van der Steen, J. J. Wentzel, and G. van Soest, "In vivo intravascular photoacoustic imaging of plaque lipid in coronary atherosclerosis," *EuroIntervention*, vol. 15, pp. 452–456, 8 2019.

[19] K. Jansen, A. F. W. van der Steen, H. M. M. van Beusekom, J. W. Oosterhuis, and G. van Soest, "Intravascular photoacoustic imaging of human coronary atherosclerosis," *Optics letters*, vol. 36, p. 597, 3 2011.

[20] M. Wu, K. Jansen, G. v. Soest, and A. F. W. v. d. Steen, "Specific imaging of atherosclerotic plaque lipids with two-wavelength intravascular photoacoustics," *Biomedical Optics Express, Vol. 6, Issue 9, pp. 3276-3286*, vol. 6, pp. 3276–3286, 9 2015.

[21] X. L. Deán-Ben and D. Razansky, "Optoacoustic image formation approaches-a clinical perspective," 2019.

[22] A. C. Tricco, E. Lillie, W. Zarin, K. K. O'Brien, H. Colquhoun, D. Levac, D. Moher, M. D. Peters, T. Horsley, L. Weeks, S. Hempel, E. A. Akl, C. Chang, J. McGowan, L. Stewart, L. Hartling, A. Aldcroft, M. G. Wilson, C. Garritty, S. Lewin, C. M. Godfrey, M. T. MacDonald, E. V. Langlois, K. Soares-Weiser, J. Moriarty, T. Clifford, Tunçalp, and S. E. Straus, "PRISMA extension for scoping reviews (PRISMA-ScR): Checklist and explanation," *Annals of Internal Medicine*, vol. 169, pp. 467–473, 10 2018.

[23] C. Peng, H. Wu, S. Kim, X. Dai, and X. Jiang, "Recent Advances in Transducers for Intravascular Ultrasound (IVUS) Imaging," *Sensors 2021, Vol. 21, Page 3540*, vol. 21, p. 3540, 5 2021.

[24] M. Yu, Y. Li, T. Ma, K. K. Shung, and Q. Zhou, "Intravascular Ultrasound Imaging with Virtual Source Synthetic Aperture Focusing and Coherence Factor Weighting," *IEEE Transactions on Medical Imaging*, vol. 36, pp. 2171–2178, 10 2017.

[25] S. Kim, S. R. Aglyamov, and S. Y. Emelianov, "Display pixel-based synthetic aperture focusing method for intravascular ultrasound imaging," *Proceedings of the 31st Annual International Conference of the IEEE Engineering in Medicine and Biology Society: Engineering the Future of Biomedicine, EMBC 2009*, pp. 475–478, 2009.

[26] K. Schroeder, C. Haas, M. Krueger, H. Ermert, T. Rastello, D. Vray, and G. Gimenez, "Synthetic aperture-based reconstruction of intravascular ultrasound images in the time domain and frequency domain," *IEEE International Symposium on Industrial Electronics*, vol. 3, pp. 1502–1507, 1999.

[27] D. Vray, T. Rastello, F. Schoofs, and P. Delachartre, "Improving the spatial resolution of intravascular ultrasound imaging with synthetic aperture Fourier-based methods," *Proceedings of the IEEE Ultrasonics Symposium*, vol. 2, pp. 1531–1534, 1997.

[28] S. Kang, J. Lee, and J. H. Chang, "Effectiveness of synthetic aperture focusing and coherence factor weighting for intravascular ultrasound imaging," *Ultrasonics*, vol. 113, 5 2021.

[29] K. Hibi, A. Takagi, X. Zhang, T. J. Teo, H. N. Bonneau, P. G. Yock, and P. J. Fitzgerald, "Feasibility of a novel blood noise reduction algorithm to enhance reproducibility of ultra-high-frequency intravascular ultrasound images," *Circulation*, vol. 102, pp. 1657–1663, 10 2000.

[30] S. Liang, F. Yang, T. Wen, Z. Yao, Q. Huang, and C. Ye, "Nonlocal total variation based on symmetric Kullback-Leibler divergence for the ultrasound image despeckling," *BMC medical imaging*, vol. 17, 11 2017.

[31] M. J. Vonesh, C. Kequing, and M. Radvany, "Digital subtraction for noise reduction in intravascular ultrasound data," *Computers in Cardiology*, pp. 329–332, 5 1991.

[32] C. Gatta, O. Pujol, O. R. Leor, J. M. Ferre, and P. Radeva, "Fast rigid registration of vascular structures in IVUS sequences," *IEEE Transactions on Information Technology in Biomedicine*, vol. 13, pp. 1006–1011, 11 2009.

[33] D. Gil, O. Rodriguez-Leor, P. Radeva, and A. Hernàndez, "Assessing Artery Motion Compensation in IVUS," *Lecture Notes in Computer Science (including subseries Lecture Notes in Artificial Intelligence and Lecture Notes in Bioinformatics)*, vol. 4673 LNCS, pp. 213–220, 2007.

[34] Y. Rim, D. D. McPherson, and H. Kim, "Volumetric three-dimensional intravascular ultrasound visualization using shape-based nonlinear interpolation," *Biomedical engineering online*, vol. 12, 5 2013.

[35] J. Park, S. Jeon, J. Meng, L. Song, J. S. Lee, and C. Kim, "Delay-multiply-and-sum-based synthetic aperture focusing in photoa-

coustic microscopy," *https://doi.org/10.1117/1.JBO.21.3.036010*, vol. 21, p. 036010, 3 2016.
[36] F. Spadin, M. Jaeger, R. Nuster, P. Subochev, and M. Frenz, "Quantitative comparison of frequency-domain and delay-and-sum optoacoustic image reconstruction including the effect of coherence factor weighting," *Photoacoustics*, vol. 17, p. 100149, 3 2020.
[37] Y. L. Sheu, C. Y. Chou, B. Y. Hsieh, and P. C. Li, "Image reconstruction in intravascular photoacoustic imaging," *IEEE Transactions on Ultrasonics, Ferroelectrics, and Frequency Control*, vol. 58, pp. 2067–2077, 10 2011.
[38] S. Cho, C. Choi, J. Ahn, T. Kim, S. Park, H. Park, J. Kim, S. Lee, Y. Kang, K. Chang, Y. Kim, and C. Kim, "SNR enhancement for catheter based intravascular photoacoustic/ultrasound imaging," *Photons Plus Ultrasound: Imaging and Sensing 2017*, vol. 10064, p. 100643P, 3 2017.
[39] M. Mozaffarzadeh, M. H. Varnosfaderani, A. Sharma, M. Pramanik, N. de Jong, and M. D. Verweij, "Enhanced contrast acoustic-resolution photoacoustic microscopy using double-stage delay-multiply-and-sum beamformer for vasculature imaging," *Journal of Biophotonics*, vol. 12, p. 201900133, 11 2019.
[40] M.-L. Li, H. F. Zhang, K. Maslov, G. Stoica, and L. V. Wang, "Improved in vivo photoacoustic microscopy based on a virtual-detector concept," *Optics Letters, Vol. 31, Issue 4, pp. 474-476*, vol. 31, pp. 474–476, 2 2006.
[41] F. Feng, S. Liang, and S.-L. Chen, "Image enhancement in acoustic-resolution photoacoustic microscopy enabled by a novel directional algorithm," *Biomedical Optics Express*, vol. 13, 11 2021.
[42] S. Jeon, J. Park, R. Managuli, and C. Kim, "A Novel 2-D synthetic aperture focusing technique for acoustic-resolution photoacoustic microscopy," *IEEE Transactions on Medical Imaging*, vol. 38, pp. 250–260, 1 2019.
[43] Z. Deng, X. Yang, H. Gong, and Q. Luo, "Two-dimensional synthetic-aperture focusing technique in photoacoustic microscopy," *Journal of Applied Physics*, vol. 109, 5 2011.
[44] H. Jin, R. Zhang, S. Liu, and Y. Zheng, "Fast and High-Resolution Three-Dimensional Hybrid-Domain Photoacoustic Imaging Incorporating Analytical-Focused Transducer Beam Amplitude," *IEEE Transactions on Medical Imaging*, vol. 38, pp. 2926–2936, 12 2019.
[45] J. Meng, C. Liu, J. Zheng, R. Lin, and L. Song, "Compressed sensing based virtual-detector photoacoustic microscopy in vivo," *https://doi.org/10.1117/1.JBO.19.3.036003*, vol. 19, p. 036003, 3 2014.
[46] H. Jin, S. Liu, R. Zhang, S. Liu, and Y. Zheng, "Frequency Domain Based Virtual Detector for Heterogeneous Media in Photoacoustic Imaging," *IEEE Transactions on Computational Imaging*, vol. 6, pp. 569–578, 1 2020.
[47] R. S. Thompson and L. S. Wilson, "The effect of variations in transducer position and sound speed in intravascular ultrasound: a theoretical study," *Ultrasound in medicine & biology*, vol. 22, no. 6, pp. 719–734, 1996.
[48] B. Cong, K. Kondo, M. Yamakawa, and T. Shiina, "Photoacoustic image reconstruction quality enhancement based on optimum focusing by calculating mean acoustic sound-speed," *IEEE International Ultrasonics Symposium, IUS*, pp. 1368–1371, 10 2014.
[49] S. Govinahallisathyanarayana, B. Ning, R. Cao, S. Hu, and J. A. Hossack, "Dictionary learning-based reverberation removal enables depth-resolved photoacoustic microscopy of cortical microvasculature in the mouse brain," *Scientific reports*, vol. 8, 12 2018.
[50] Z. Tu, B. Wang, T. Duan, and F. Gao, "Pattern-learning-based Noise Elimination Algorithm in Photoacoustic Sensing and Imaging," *Proceedings of the Annual International Conference of the IEEE Engineering in Medicine and Biology Society, EMBS*, vol. 2018-July, pp. 4808–4811, 10 2018.
[51] J. Gröhl, M. Schellenberg, K. Dreher, and L. Maier-Hein, "Deep learning for biomedical photoacoustic imaging: A review," *Photoacoustics*, vol. 22, p. 100241, 6 2021.
[52] M. Xu and L. V. Wang, "Photoacoustic imaging in biomedicine," *Review of Scientific Instruments*, vol. 77, no. 4, 2006.

Appendix

A. Search Queries

The search queries for IVUS and PA parts for both databases are given below.

IVUS - PubMed: ("Intravascular ultrasonography"[All Fields] OR "Intravascular Ultrasound"[All Fields] OR "IVUS"[All Fields]) AND ("Image Reconstruction"[All Fields] OR "Image Processing"[All Fields]) AND ("Algorithms"[MeSH Terms] OR "algorithm*"[All Fields])

IVUS - IEEExplore: ("All Metadata":Intravascular Ultrasound OR "All Metadata":IVUS OR "All Metadata":Intravascular Ultrasonography) AND ("All Metadata":image reconstruction OR "All Metadata":image processing) AND "All Metadata":Algorithm*

PA - PubMed: ("Photoacoustic Techniques"[MeSH Terms] OR "optoacoustic*"[All Fields] OR "photoacoustic*"[All Fields]) NOT ("Tomography"[MeSH Terms] OR "computed tomography"[All Fields]) AND ("Image Processing"[All Fields] OR "Image Reconstruction"[All Fields]) AND ("Algorithms"[MeSH Terms] OR "algorithm*"[All Fields]) NOT ("Linear Array*"[All Fields] OR "Phased Array"[All Fields])

PA - IEEExplore: ("All Metadata":Photoacoustic Techniques OR "All Metadata":optoacoustic* OR "All Metadata":photoacoustic*) NOT ("All Metadata":tomograph* OR "All Metadata":computed tomography) AND ("All Metadata":Image Processing OR "All Metadata":Image Reconstruction) AND ("All Metadata":Algorithm*) NOT ("All Metadata":linear-array* OR "All Metadata":phased array)

B. Results tables

See the following two pages for Table 1 with the IVUS results and Table 2 with the PA results.

Table 1. Results IVUS image reconstruction algorithms.
Abbreviations: CNR = Contrast-to-Noise Ratio; SAF = Synthetic Aperture Focusing Techniques; SAFT = SAF Technique(s); PSF = Point Spread Function; CFW = Coherence Factor Weighting; CAD = Coronary Artery Disease; MSSIM = Mean Structural Similarity Index; NIQE = Natural Image Quality Evaluator; hCAR = harmonic Cardiac Alignment Rate; N/A = Not Available;

Author (Year)	*#Citations*	*Aim*	*Algorithm*	*Method*	*Main results*	*Computational time*	*Advantages*	*Disadvantages*
				Improve spatial resolution by SAFT				
Kim et al. (2009)	1	Improve spatial resolution and CNR Remove blurring caused by Digital Scan Converter (DSC)	Display Pixel-based SAF technique (DPBSAF)	***Data*** Nylon strings phantom Polyvinyl alcohol phantom Ex vivo rabbit artery ***Transducer*** f = 20 MHz	CNR: 100.3 dB Peak in angular profile of PSF becomes narrower at higher depths, compared to conventional SAF	Similar as conventional SAF with 256 beams up to 300x300 pixels	Also removes DSC blurring, besides improving resolution and contrast	
Schroeder et al. (1999)	0	Improve lateral resolution	Time-domain algorithm: DAS SAFT + weighting Frequency domain (FD) algorithm:	***Data*** Wire phantom ***Transducer*** f = 20 MHz	FD algorithm performed best: lower grating lobes and narrower main lobe Grating lobe level: -25 dB Main lobe width: 1.7 imaging lines	N/A	Transducer has multiple elements, but algorithm also evaluated for monostatic approach where single element acts as both transducer and receiver.	Only relative values for computational time for the multistatic approach: FD 4x faster Time domain: weighting further reduced grating lobes, but at expense of lateral resolution.
Vray et al. (1997)	4	Improve lateral resolution	SAFT by taking PSF characteristics into account	***Data*** Wire phantom ***Transducer*** f = 30 MHz sampling f = 100 MHz	Factor 3 improvement of resolution, compared to raw data	N/A		No clear quantitative results. Main results derived from a graph, with 'resolution cells' as unit Only tested on one dataset
Yu et al. (2017)	18	Improve lateral resolution and CNR, especially at higher imaging depth	Virtual Source Synthetic Aperture (VSSA) focusing and CFW	***Data*** Tungsten wire phantom Agar-based phantom Anechoic cyst phantom Ex vivo human artery ***Transducer*** - flat f = 40 MHz Sampling f = 500 MHz	VSSA+CFW - from 1 to 6 mm imaging depth: CNR: 3 - 3.6 Lateral resolution: 120 – 160 µm Imaging depth improved from 4.7 to 6.5 mm Overall: Lateral resolution increased 42% after applying CFW to VSSA	N/A	Applicable in IVPA. Rotational scan shows good results Algorithm has a noise-suppressing nature	VSSA alone does not improve resolution, neither visually nor quantitatively
Kang et al. (2021)	3	Improve spatial and contrast resolution	SAFT+CFW	***Data*** Simulation Wire phantoms Tissue-mimicking phantom Experiments are performed with a focused and flat transducer ***Transducer*** - flat f = 50 MHz ***Transducer*** – focused f = 50 MHz Focal depth = 3 mm	***Flat transducer*** CNR – from 5 to 3 mm imaging depth: Conventional: 0.2 – 2.0 SAF: 0.8 – 2.9 CFW: 0.5 – 1.6 SAF-CFW: 0.6 – 1.8 ***Focused transducer*** CNR – from 5 to 3 mm imaging depth: Conventional: 0.6 – 2.7 SAF: 1.2 – 3.5 CFW: 0.8 – 2.5 SAF-CFW: 1.0 – 3.0 ***Overall*** CFW is responsible for best lateral resolution, SAF for best CNR SAF+CFW provides optimal CNR and resolution combination	N/A	Authors claim that SAF+CFW is a good candidate for intravascular atherosclerotic plaque burden because it provides a high CNR, SNR, and spatial resolution.	Theoretically proves that SAF+CFW will not perform well in single-element intravascular imaging, but results show otherwise.
				Noise reduction				
Hibi et al. (2000)	18	Noise reduction Blood noise	Blood Noise Reduction (BNR) algorithm	***Data*** 35 CAD patients ***Transducer*** f = 40 MHz Focal zone: 1.5 – 2.5 mm	Inter- and intra-observer variability decreased after BNR was applied, especially in lumen and plaque + media areas	7 s/img		Reconstruction of 500 frames takes ~60 min BNR is affected by motion artifacts from the transducer during a cardiac cycle
Vonesh et al. (1991)	4	Noise reduction Noise type not specified	Digital subtraction	***Data*** Vascular phantom ***Transducer*** f = 20 MHz	Noise is lower than in original images: 0.67 vs ~0.7	N/A	Simple and straightforward method	Needs subtraction of a background image. This is likely not always available in clinical settings and it complicates real-time application
Liang et al. (2017)	11	Noise reduction Multiplicative noise	Nonlocal total variation (NTLV)	***Data*** Synthetic noisy images Kidney phantom Liver US, IVUS, 3DUS ***Transducer*** N/A	*2D phantom – proposed vs two other methods* SNR: 36.8 vs. 19.88 and 31.541 MSSIM: 0.9987 vs. 0.9550 and 0.9939 *IVUS – proposed vs 2 other methods* NIQE: 6.42 vs. 6.06 and 5.49	N/A	Performance evaluated on multiple different data sets Outperforms current state-of-the-art filters for US denoising	
				Motion correction				
Gatta et al. (2009)	37	Motion correction	Algorithm to estimate rigid roto-translation between IVUS images	***Data*** Nine vessel sequences from seven patients ***Transducer*** N/A	hCAR larger for each sequence compared to one other method	3.16 frames/s Frame = 480x480	Results validated by comparison to fastest available algorithm with similar aim Fast: ~2.6 min	Three parameters to finetune
				3D Reconstruction				
Rim et al. (2013)	13	3D reconstruction	Shape-based nonlinear interpolation	***Data*** 25 2D IVUS frames of artery ***Transducer*** f = 20 MHz	Similar grey values and 0.013 ± 0.019 mm wall thickness difference between reconstructed intermediary slices and original slices.	N/A	The depicted results show a smooth 3D shape	Segmentation required prior to algorithm application.

Table 2. Results PA image reconstruction algorithms.
Abbreviations: VD = Virtual Detector; SAFT = Synthetic Aperture Focusing Techniques; CFW = Coherence Factor Weighting; SNR = Signal-to-Noise Ratio; DAS = Delay-and-Sum; DMAS = Delay-Multiply-And-Sum; DS-DMAS = Double Stage DMAS; FWHM = Full Width at Half Maximum; FD = Fourier Domain; N/A = Not Available;

Author (Year)	*#Citations*	*Aim*	*Algorithm*	*Method*	*Main results*	*Computational time*	*Advantages*	*Disadvantages*
				IVPA imaging				
Sheu et al. (2011)	22	IVPA image reconstruction	Three conventional methods: Filtered Back Projection (FBP), Lambda-tomography, and Estimation Minimization (EM) method	***Data*** Numerical phantom Phantoms (point object, cuboid structure) ***Transducer*** f = 40 MHz ***Laser*** λ = 532 nm PRR = 10 Hz Pulse width = 5 ns	No quantitative results EM with 10 iterations outperforms FBP and lambda-tomography.	N/A		Computational time not mentioned, but assumed to be long due to 10 required iterations No quantitative metric provided. Visual results are not convincing
Cho et al. (2017)	1	SNR improvement in IVPA	DAS and Modulation Transfer Function (MTF) filtering	***Data*** Carbon fiber phantom In vivo rabbit ***Transducer*** f = 40 MHz ***Laser*** λ =1064 nm PRR = 24 kHz Pulse energy = 5 µJ	***Carbon fiber*** SNR for 2 – 5 in axial position MTF: 16-28 dB DAS, DAS+MTF: 18-29 dB MTF, DAS, DAS+MTF improve SNR, but last two show largest increase. Same results visually from in vivo data.	12 frames per second	Simple and easily reproducible algorithms	Quantitative evaluation based on one metric only Only a ~1-fold improvement in SNR
				Out-of-focus resolution improvement				
Li et al. (2006)	194	Improve out-of-focus resolution	VD-SAFT with CFW	***Data*** Carbon fiber phantom In vivo mouse ***Transducer*** - focused f = 50 MHz Focal depth = 6.7 mm NA = 0.44 ***Laser*** λ = 584 nm PRR = 10 Hz Pulse width = 10 ns Pulse energy > 1mJ/cm^2	***Carbon fibre phantom*** at -6 dB Lateral resolution: 46-53 µm Improved SNR up to 29 dB	N/A	CFW can also suppress background noise	No result of SAFT without CFW is given
Park et al. (2016)	115	Improve out-of-focus resolution	SAFT+DMAS	***Data*** Carbon fiber phantom In vivo mouse abdomen ***Transducer*** - focused f = 50 MHz NA = 0.5 ***Laser*** λ = 570 nm PRR = 2.5 kHz Pulse width = 9 ns	FWHM (lateral): 75-87.3 µm SNR: 63-69.1 dB	Data size: 1024x2400x4000 2h	Also reduces reverberation artifacts	Reconstruction of 500 images takes ~15 min
Mozaffarzadeh et al. (2019)	18	Improve out-of-focus resolution	SAFT+DS-DMAS	***Data*** Hair phantom In vivo rat vasculature surrounding sentinel lymph node ***Transducer*** - focused f = 50 MHz Acoustic focal spot: ~46 µm ***Laser*** λ = 570 nm PRR = 5 kHz	Noise level ranges from -53.4 to -68 dB for depths between 0.91 to 4.85 mm Noise level reduction up to 134% compared to original image Better contrast (only visually)	14.45 sec/image		Reconstruction of 500 images takes >120 min The noise around the focal zone is not removed
Spadin et al. (2020)	27	Improve out-of-focus resolution	DAS and FD algorithm, both combined with CFW	***Data*** Gold wire phantom In vivo mouse with human breast carcinoma ***Transducer*** – wire phantom f = 50 MHz ***Laser*** – wire phantom λ = 532 nm Pulse width = 8 ns Pulse energy = 85 µJ ***Transducer*** – in vivo Bandwidth = 5-35 MHz Focal depth = 6.8 mm NA = 0.6 ***Laser*** – in vivo λ = 532 nm Pulse width = 1.4 ns Pulse energy = 1 mJ Focused transducers	***Wire phantom*** - CNR FD, DAS: 34-36 dB with CFW: 60-81 dB ***Wire phantom*** – Lateral resolution DAS, FD: 62-63 µm with CFW: 65-66 µm ***In vivo*** - CNR FD, DAS: increase of 3-4 dB with CFW: extra increase 2-3 dB CFW does not improve the lateral resolution	DAS: 7.10 s/img FD: 0.25 s/img DAS + CFW: 12 s/img FD + CFW: 0.5 s/img	Equal performance, but FD is significantly faster Reconstruction of 500 images by the FD algorithm takes ~2 min	
Feng et al. (2021)	0	Improve out-of-focus resolution	Fourier Accumulation SAFT (FA-SAFT) and directional model-based deconvolution (D-MB)	***Data*** Tungsten wire phantoms Leaf skeleton phantom In vivo mouse dorsal blood vessels ***Transducer*** - focused f = 50 MHz Focal depth = 6.7 mm NA = 0.44 ***Laser*** N/A	Lateral FWHM: 26-31 µm Lateral resolution: 460-490 µm	Data size 121x121x30 FA-SAFT: ~72 sec D-MB: ~8 sec	Image improvement in focal and out-of-focus region	Reconstruction of 500 images takes ~22 min (for 16 SAFT directions)
Jeon et al. (2019)	56	Improve out-of-focus resolution in 3D reconstruction	2D-directional-SAFT	***Data*** Carbon fiber phantom Leaf skeleton phantom In vivo mouse limb ***Transducer*** - focused f = 50 MHz NA = 0.5 ***Laser*** λ = 532 nm Pulse energy = 6 µJ	***Carbon fiber*** (N=16) FWHM: 45-53 µm SNR: 41-46.6 dB Over all imaging depths ***Leaf skeleton*** FWHM: 79 µm ***In vivo*** FWHM: 97-93 µm SNR: 11.3-13.2 dB	GPU accelerated: 596.37 s Unclear: likely per image	Outperforms other 2D-SAFT in vivo. Extensive algorithm explanation	In vivo it could not outperform conventional 1D-SAFT Very long computational time
Deng et al. (2011)	44	Improve out-of-focus resolution in 3D reconstruction	2D-SAFT + CFW	***Data*** Carbon fiber phantom In vivo mouse dorsal dermis ***Transducer*** - focused f = 50 MHz Focal depth = 6.7 mm NA = 0.44 ***Laser*** N/A	***Carbon fiber*** Lateral resolution z-x: 65-90 µm z-y: 70-88 µm Still worse than at focus Overall better resolution than 1D-SAFT, which has better resolution in B-scan direction	N/A		Focused on the resolution in certain direction. Carbon fibers are also arranged in the two directions, whereas actual data would not follow these specific orientations
Jin et al. (2019)	11	Improve out-of-focus resolution	3D reconstruction with Non-Uniform Fast Fourier Transform (NUFFT)	***Data*** Numerical simulations USAF1951s phantom Hair phantom In vivo mouse leg *Phantoms* ***Transducer*** – focused f = 20 MHz Focal depth = 12.7 mm NA = 0.393 ***Laser*** λ = 532 nm PRR = 80 Hz Pulse width = 6 ns Pulse energy = 1 mJ/cm^2 *In vivo* **Transducer** – focused f = 5 MHz NA = 0.25 ***Laser*** λ = 1064 nm PRR = 10 Hz Pulse energy = 5 mJ/cm^2	Resolution (FWHM) USAF1951s phantom: 88.39 µm Hair phantom: 176 µm In vivo: 1.11 – 1.77 mm Overall conclusion: Outperforms conventional DAS and Stolt migration in resolution and is more efficient than conventional model-based and timer reversal algorithms.	8.15 sec for 200x200x150 dataset	Performance evaluated with six different datasets. NUFFT interpolation error reduces to 4% when oversampling factor is 2 Fast algorithm	
				Account for heterogeneous media				
Jin et al. (2020)	11	Account for heterogeneous media	FD-based VD	***Data*** 2D numerical simulations Carbon fiber phantom Ex vivo porcine tissue ***Transducer*** - focused f = 5 MHz Focal depth = 20 mm ***Laser*** λ = 532 nm PRR = 80 Hz Pulse width = 6 ns Pulse fluence = 1 mJ/cm^2	***Numerical solution*** VD-SAFT vs proposed: Resolution heterogeneous media: 1.4 vs 0.5 mm Relative error: 7.92 vs 4.20 and 10.41 vs 4.37 (for full fluid and fluid-solid-fluid phantoms) ***Carbon fiber*** of 3 rods VD-SAFT vs. proposed (fluid layered wave extrapolation) vs. proposed (elastic layered wave extrapolation) FWHM: 1.42, 1.86, >2 vs. 1.35, 1.42, 1.45 vs. 1.33, 1.38, 1.41	0.6-0.7 s for 40x40x2000 data	Extensive algorithm explanation Very low computational time Also improved image quality in homogeneous media	
Cong et al. (2014)	1	Account for heterogeneous media	Automatically select mean speed of sound	***Data*** Numerical simulation ***Transducer & Laser*** N/A	The estimated speed of sound provides higher image quality	N/A		Needs prior information: selected region of interest or segmented image
				Artificial Intelligence				
Govinahallisathyanarayana et al. (2018)	21	*Deep Learning* Reverberation artifact removal	Dictionary learning	***Data*** Polystyrene beads phantom In vivo mouse brain ***Transducer*** f = 35 MHz ***Laser*** λ = 559 nm PRR = 10 kHz	21.0 ± 5.4 dB reverberant artifact suppression, allowing for depth-resolved PAM up to 500 µm	20 s/img for A-line interval of 0.83 µm and sparsity of 5	Possible to reduce computation time with online and minibatch methods	The dictionary itself may contain irrelevant information and can be very noisy Relatively long computational time Difficult to tune on large datasets
Tu et al. (2018)	0	*Deep Learning* Reduce periodically interference noise	Pattern learning noise detection method	***Data*** Water tank sample ***Transducer & Laser*** N/A	More stable than other filtering methods to reduce the noise	Lower computational time than filtering		Effectiveness shown for only one type of noise No in or ex vivo data used

B

Appendix B - IVPA Optimization Results

B.1. Theoretical Validation

B.1.1. Delay and Sum Effect

The maximum delays over the arc in the center of the plots ranges between 49 and 54 samples, with largest delays for the scatterers 4 and 5. The guideline for the DAS to have a beneficial effect on the image quality was set to 40 samples. Thus, the found delays are only slightly larger.

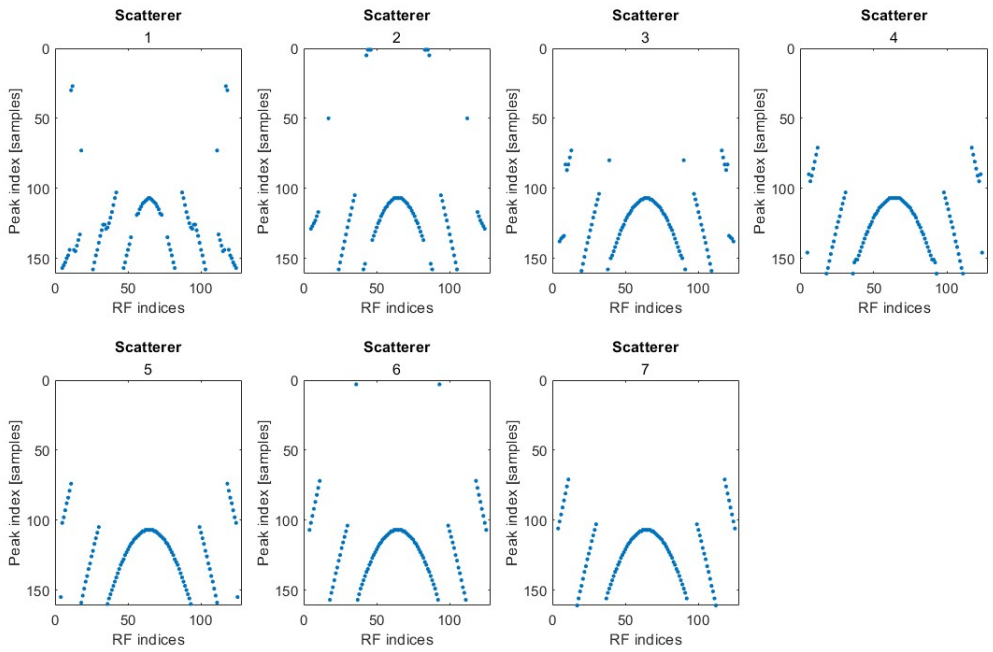

Figure B.1: Overview of the delay range per scatterer. Generated by plotting the sample index where the peak of the RF signal occurs.

B.1.2. Theoretical Maximum Image Quality

The RF signals, envelope signals, and the PSF of the original signal, the DAS results, and the only sum result is shown for scatterers 1, 3 and 7. Scatterer 1 is placed at the natural focus and scatterer 3 and 7 are placed in the far field. Similar to the IVUS results, the DAS and only sum results are almost similar. The DAS and only sum have show an increased maximum amplitude compared to the original result, but the LR of all three signals is similar.

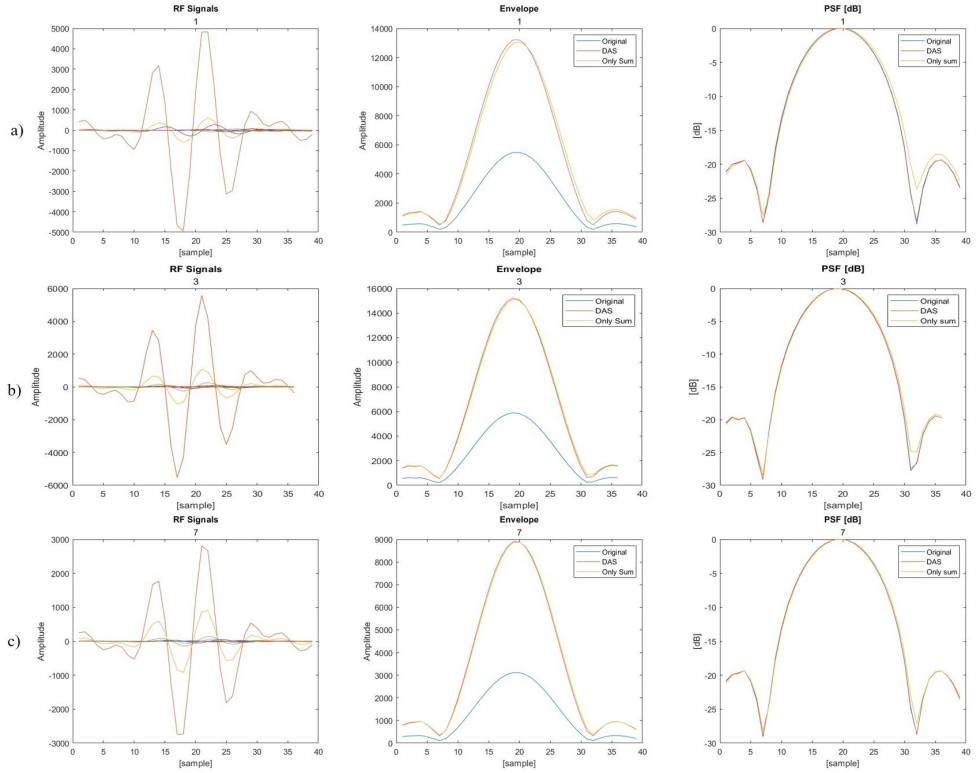

Figure B.2: From left to right for each image: The RF signals of the scatterer, the envelopes of the original, DAS and only sum results, and the PSF of the original, DAS and only sum signals. a) shows the results for scatterer 1 at the natural focus at 0.16 mm beyond the transducer, and scatterer 3 at 2 mm and 7 at 6 mm in the far field in b) and c) respectively. The DAS and only sum result show very similar behaviour for the envelope signal and the PSF. The further away the scatterer, the more similar these signals are. The PSF is very similar for all three signals, so neither DAS nor only sum does not improve the lateral resolution. The maximum intensity is however strongly increased by DAS and only sum, compared to the original signal

B.2. Optimization

The optimization results with the VS behind the transducer are depicted below. Green indicates the best values for LR and MI. The optimal combination of LR and MI was found for a VS depth of 0.7 mm and a half opening angle of 2 degrees. There are no scatterers placed in the near field, because the natural focus is only 0.16 mm from the transducer. Due to the proximity of the natural focus, all scatterers lie in the far field except for scatterer 1 that was placed at the natural focus.

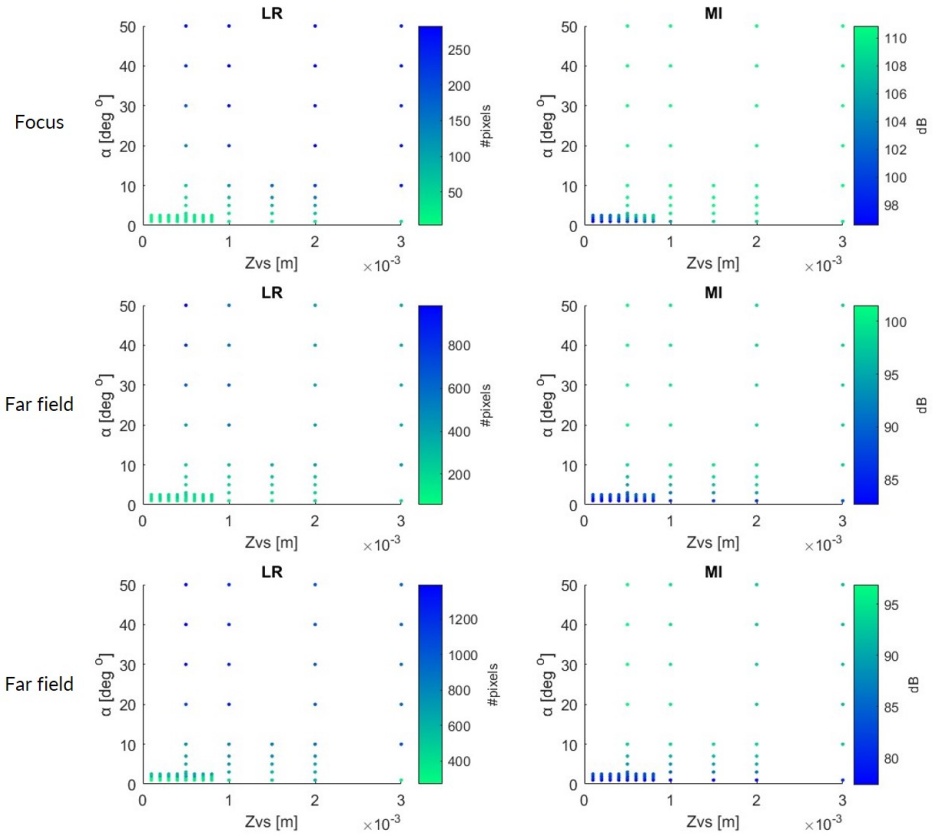

Figure B.3: The optimization results for LR and MI plotted over the input ranges of half opening angle of the beam (α) and the VS depth behind the transducer (z_{vs}). The results are visualized for scatterer 1 at the focus, and scatterer 3 and scatterer 7 in the far field. Green stands for the best values, and blue for the worst values for LR and MI.

Table B.1: IVPA quantification of the image quality for the original image the optimization results of the VS behind the transducer. Per scatterer, the maximum intensity (MI) is reported in dB and the lateral resolution (LR) in number of pixels that fall within the 0 to -6 dB range. The LR in number of pixels is based on the IVPA images with 501x501 pixels, instead of the 2001x2001 IVUS images.

Non-Optimized								
	Scatterer	**1**	**2**	**3**	**4**	**5**	**6**	**7**
Original *RF stacking*	Lateral Resolution [#pixels]	22	78	219	370	503	636	763
	Maximum Intensity [dB]	93.3	83.4	76.6	74.0	72.5	71.7	71.3
Optimized								
	Scatterer	**1**	**2**	**3**	**4**	**5**	**6**	**7**
Behind z_{vs} = 0.7 mm α = 2 °	Lateral Resolution [#pixels]	22	46	172	241	317	385	443
	Maximum Intensity [dB]	106.6	97.2	88.5	85.9	84.5	83.6	82.9